ERDC/CHL TR-22-20

Coastal and Hydraulics Laboratory

US Army Corps
of Engineers®
Engineer Research and
Development Center

ERDC
ENGINEER RESEARCH & DEVELOPMENT CENTER

Operational Modeling of Large Container-Type Vessel-Generated Waves with Related Erosion and Scour Effects

Michael-Angelo Y.-H. Lam, Matt Malej, and Fengyan Shi

September 2022

ERDC/CHL TR-22-20
September 2022

Operational Modeling of Large Container-Type Vessel-Generated Waves with Related Erosion and Scour Effects

Michael-Angelo Y.-H. Lam and Matt Malej

Coastal and Hydraulics Laboratory
US Army Engineer Research and Development Center
3909 Halls Ferry Road
Vicksburg, MS 39180-6199

Fengyan Shi

Center for Applied Coastal Research
University of Delaware
259 Academy Street
Newark, DE 19716

Final report

Prepared for Navigation Systems Research Program
US Army Engineer Research and Development Center
3909 Halls Ferry Road
Vicksburg, MS 39180-6199

Under Funding Account Code U4381107; AMSCO Code 031391

Abstract

In this report, the US Army Engineer Research and Development Center, Coastal and Hydraulics Laboratory, presents a numerical modeling study using FUNWAVE-TVD to investigate ship-induced waves of large container-type vessels with related erosion and scour effects. The new vessel wake generating models implemented in the FUNWAVE-TVD Vessel Module are presented and validated against field data in the Sabine-Neches Waterway, Texas. Utilizing the Sediment Transport and Morphology Change Modules, ship wake-induced erosion is analyzed to assess potential impacts to Sabine-to-Galveston Hurricane Flood Protection Systems.

Contents

Report Documentation Page

Figures and Tables

Figures

Tables

Preface

This study was conducted for the Navigation Systems Research Program under Funding Account Code U4381107; AMSCO Code 031391. The study was performed by the US Army Engineer Research and Development Center (ERDC), Coastal and Hydraulics Laboratory (CHL), and the Center for Applied Coastal Research.

At the time the study was completed, Ms. Morgan Johnston was the program manager for the Navigation Systems Research Program, and Mr. Charles E. Wiggins was the technical director, Navigation. The general administrative supervision was provided by Mr. Victor M. Gonzalez, chief, Coastal Processes Branch, and Dr. Cary A. Talbot, chief, Flood and Storm Protection Division.

At the time of publication of this report, Mr. Keith Flowers was the deputy director of CHL, and Dr. Ty V. Wamsley was the director.

COL Christian Patterson was commander of ERDC, and the director was Dr. David W. Pittman.

1 Introduction

1.1 Motivation

Modeling of ship-induced waves can be a challenging hydrodynamic problem, requiring accurate and efficient high-fidelity computation of multiple coastal processes and strongly nonlinear evolution equations for the free-surface waves. Quite often, because of the numerical tool constraints, models rely on ad hoc equations to capture physical phenomena, such as nonlinear wave-wave interactions, energy dissipation due to wave breaking, or interplay between waves and currents. The challenge is further complicated by the inclusion of sediment transport that can deliver a result that can be factors off from the full and correct solution. Accurate prediction of ship-induced waves and the associated erosional effects is a pressing need for the US Army Corps of Engineers (USACE) to maintain, expand, and construct navigation channels across the country cost effectively. The United States possesses longer navigation and intracoastal waterways than any other country, and even more than the next three in line, combined. This inevitably puts more urgency on research and development activities that can deliver an accurate and meaningful description of the vessel-wake field in an operational and computationally efficient setting.

1.2 Background

1.2.1 FUNWAVE-TVD

FUNWAVE-TVD is a phase-resolving wave model based on fully nonlinear Boussinesq-type equation coupled with a Godunov-type Riemann solver (Shi et al. 2012). It is a revision of the FUNWAVE model previously developed (Chen et al. 2000; Kennedy et al. 2000) with more complete fully nonlinear Boussinesq equations and more faithful model nonlinearities by several improvements, such as the following:

- Implementation of a time-varying reference elevation (Kennedy et al. 2001)
- Inclusion of vertical vorticity, correction (Chen 2006)
- Reformulation of the governing equations to a conservative form allowing the following:

  - Shock capturing through the higher-order Monotonic Upstream-centered Scheme for Conservation Laws-Total Variation Diminishing (MUSCL-TVD) scheme (Erduran et al. 2005)
  - Increased numerical accuracy using a third- and fourth-order Runge-Kutta time-stepping scheme. (Gottlieb et al. 2001).

Currently, FUNWAVE-TVD takes advantage of parallel computing by implementing Message Passing Interface with distributed domain decomposition, allowing for quick turnaround of numerical simulations through utilization of the Department of Defense (DoD) high-performance computing (HPC) systems such as Onyx (ERDC) or Koehr and Ganey (Navy).

The US Army Engineer Research and Development Center (ERDC), Coastal and Hydraulics Laboratory, has engaged in several collaborative efforts with the University of Delaware to extend the capabilities of FUNWAVE. Recently, these efforts have added

- Ship Wake Module (Shi et al. 2018)
- Sediment Transport and Morphology Modules (Tehranirad et al. 2016; Malej et al. 2019)
- Meteo-tsunami Module (Woodruff et al. 2018)
- Parallel input/output with HPC profiling and optimization (Lam et al. 2018).

1.2.2 Additions to the FUNWAVE-TVD vessel module

The validation work was preceded by the development of a new series of vessel-wave generation mechanisms in the numerical wave model FUNWAVE-TVD (Shi et al. 2018) that would be capable of modeling larger container-type vessels. The new mechanisms contain two pressure-source type and two slender-body type methodologies for vessel-induced wave generation and are uniformly valid for most types of vessels. The larger container-type vessel waves are normally characterized with a draw-down-type wave being present in a primary wave and are nonlinear in nature. The vessel-wave source functions were originally derived based on two general categories of vessels: small vessels (tugs, tows, pleasure crafts) and large vessels (tankers and largo cargo ships). Each source function contains a combination of two or more analytical functions, which can closely represent the vessel shape (body/hull) and accurately generate associated waves. For each category, basic vessel parameters were defined in model inputs such as vessel length, beam, and draft.

1.2.3 Sabine-Neches Waterway (SNWW)

The Sabine-Neches Waterway (SNWW) is the nation's third largest commercial waterway (Figure 1). According to the USACE Galveston District (SWG) investigations (USACE 2018), over 96 million tons of cargo were transported along the SNWW in 2015, which required 53,000 vessel transits whereas in 2017, that number increased to 300 million tons of cargo. The SNWW is a 64 mi[1,2] long, federally constructed, deep-draft navigation project serving Jefferson and Orange Counties in Texas and Cameron as well as Calcasieu Parish in Louisiana. The SNWW is home to 2 of the nation's 17 DoD strategic seaports. One of those is Port Arthur, located closer to the downstream end of the channel (see right image in Figure 1). The other port is Port Arthur of Beaumont, which leads the military's heavy tonnage deployment efforts. As such, the SNWW serves by helping move over 70% of all the military's heavy tonnage west of the Mississippi River that is not bound for the Pacific Area of Responsibility (AoR) (USACE 2018).

---

[1] For a full list of the spelled-out forms of the units of measure used in this document, please refer to *US Government Publishing Office Style Manual*, 31st ed. (Washington, DC: US Government Publishing Office 2016), 248-52, https://www.govinfo.gov/content/pkg/GPO-STYLEMANUAL-2016/pdf/GPO-STYLEMANUAL-2016.pdf.

[2] For a full list of the unit conversions used in this document, please refer to *US Government Publishing Office Style Manual*, 31st ed. (Washington, DC: US Government Publishing Office 2016), 345-7, https://www.govinfo.gov/content/pkg/GPO-STYLEMANUAL-2016/pdf/GPO-STYLEMANUAL-2016.pdf.

Figure 1. (left) Location of SNWW in the Texas area marked with a pin; (right) satellite image of the SNWW.

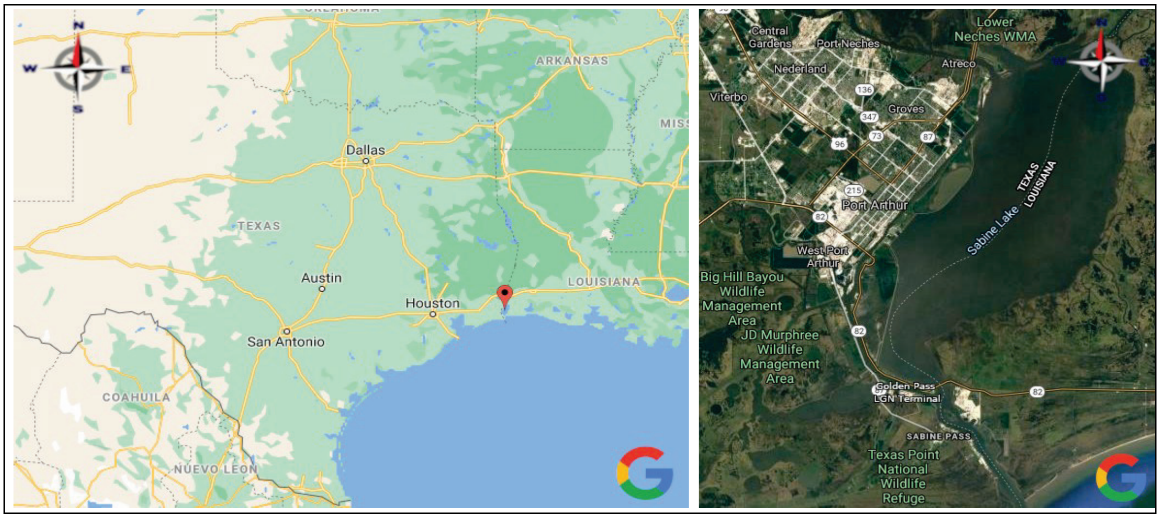

1.3 Objective

The SWG is currently engaged in the Sabine Pass to Galveston Bay (S2G) Preconstruction, Engineering, and Design study. The study was partially supported by the USACE SWG with the objective of providing validation of FUNWAVE-TVD vessel model using the field data observed in SNWW and an assessment of scour/erosion effects along the western bank of the SNWW that can potentially impact the S2G Freeport Hurricane Flood Protection Systems (HFPS). The background description of this effort follows the description in *Sabine Pass to Galveston Bay, Texas Coastal Storm Risk Management and Ecosystem Restoration Draft Integrated Feasibility Report – Environmental Impact Statement* (USACE 2017).

1.4 Approach

Field observations of vessel-induced waves in SNWW have been conducted by Lamar University and University of Houston (Zaloom et al. 2017). Wave measurements were taken at two locations, the Port Arthur dock and Golden Pass dock, which were determined according to the observed erosion hot spots. Vessel voyage information was obtained using the Automatic Identification System (AIS), which reflects the real-time speed and course over ground, rate of turn, and location at each time stamp for every commercial vessel. Type, name, length, beam, and draft of each vessel that passed the measuring locations were documented. Two types of waves were observed. One type is classified as short-period waves such as those generated by tugs, tows, and small crafts. The other type is long period waves induced by large cargo ships or tankers, often referred to as a transverse stern wave (TSW), comprised of the typical drawdown followed by a surge within the primary wave. The project report of Zaloom et al. (2017) provides wave statistics for short waves and eight sets of time series of surface elevation from the long wave measurements. In addition, the study provides estimates of the sediment erosion rate based on the channel hydraulic conditions, bank soil characteristics, and measured wave data.

As far as validations are concerned, the above-mentioned field data were not able to be obtained, and there was need to validate the model against only two separate results from digitized images in Zaloom et al. (2017). Based on data availability, two surge wave processes at Port Arthur, which have an average maximum wave height of 0.36 m, and two surge wave processes at Golden Pass with an average maximum wave height of 0.32 m, were used. Additional validation runs were also performed against a select vessel (*Pacific Sapphire*) from the report of Maynord (2003).

1.5 Report contents

- Section 2: an outline of how the global grid of the SNWW was constructed and how individual channel sub-grids were created. In addition, basic convergence and sediment module tests are shown, along with details on the AIS data and path interpolation/correction. Finally, different types of pressure-source generations are listed with sample schematics of the hull/body shapes.
- Section 3: presentation of ship-wake validation work against two vessels contained in Zaloom et al. (2017) and one vessel in Maynord (2003), as well as parametric study of the solution space.
- Section 4: results of the multi-vessel simulations with identification of erosion/scour hot spots.
- Section 5: discussion and conclusions.

2 Model Setup and Description

2.1 Bathymetry/topography data construction

The bathymetric and topographical data were needed to be merged and interpolated onto a rectilinear FUNWAVE grid, which subsequently was divided into five subgrids. The subgrids were carved out to minimize the redundant (dry) areas of the domain to limit the computational burden in the numerical simulations. The data reconstructions and prioritization consisted of two steps:

1. Convert longitude/latitude to Universal Transverse Mercator (UTM).

   The bathymetric/topographical data sets were provided by the SWG from previous projects and recent surveys. Sources are the following:

   a. ctx_adcirc_grid extact_20181110_meters_NAVD88.xyz.zip
   b. KeithLake_Interpolated_StatePlaneTXSouthCentraUSft_NAVD88.csv
   c. KeithLake_Merged_StatePlaneTXSouthCentralUSft_NAVD88.csv
   d. KL-Sabine_Model_NAD83UTM15_MSL.csv
   e. Datum adjustment was based on NOAA SABINE PASS NORTH station (8770570), MSL = 0.293 m NAVD88.
2. Extract subdomains. An automated program was developed to generate channel grids from the raw data (UTM format). The computational domains include five grids: (a) Mouth, (b) Gauge2, (c) Gauge2up, (d) Turner, and (e) Gauge1, as shown in Figure 2. The bathymetry/topography of the five grids were obtained by linear interpolation using the raw data; the results of which are shown in Figures 3 through 7.

2.2 Test runs with different grid resolutions

Test runs with different grid resolutions were conducted to find an appropriate grid resolution to be used for this application. Here is shown only the difference between the models with 5.0 m grid resolution and 1.0 m grid resolution in Figures 8 and 9. As shown in Figure 10, a greater detail in resolving the entire wake structure (both divergent and transverse) is achieved at the higher resolution compared to the result from the 5 m resolution model. The tests showed that further reducing the grid size did not gain more information about the wake structure but caused significant computational burden (e.g., a resolution of 0.5 m would increase the burden by over tenfold). Therefore, it was decided to use the resolution of 1.0 m in the subsequent simulation runs.

Figure 2. Definition of five subdomains. Traversing south to north, (a) Mouth, (b) Gauge2, (c) Gauge2up, (d) Turner, and (e) Gauge1. The colorbar of bathymetry and topography elevation is in meters.

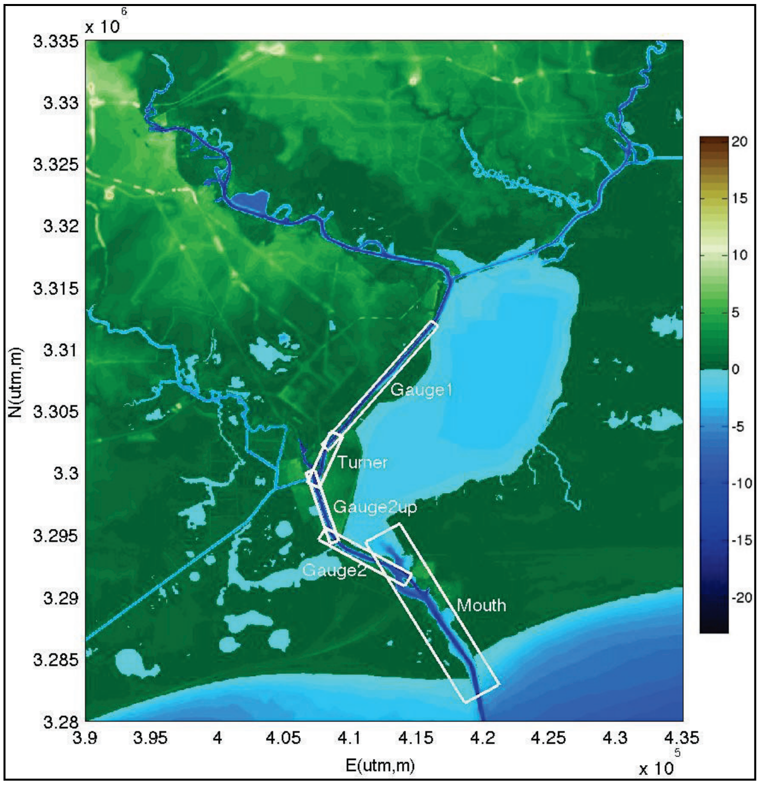

Figure 3. Grid: Mouth. Colorbar of bathymetry and topography elevation is in meters.

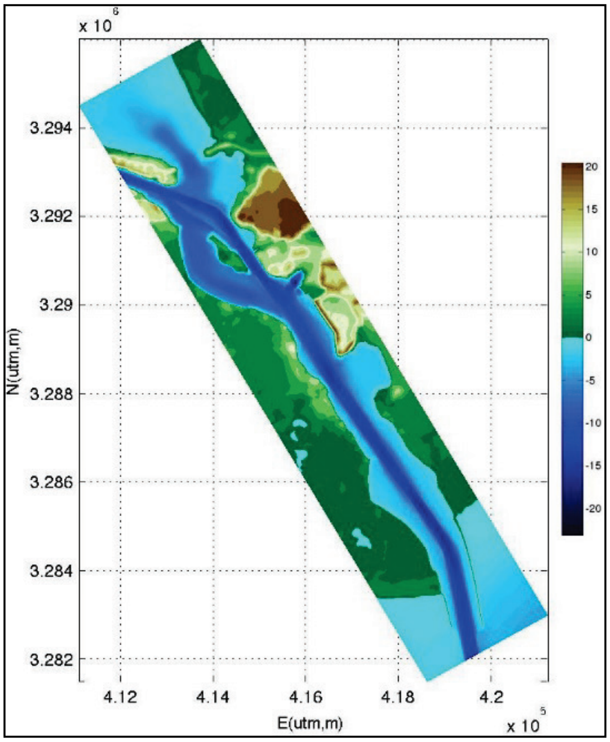

Figure 4. Grid: Gauge2. The red pin drop represents a relative location of Gauge 2 in the Golden Pass area contained in the report of Zaloom et al. (2017). The colorbar of bathymetry and topography elevation is in meters.

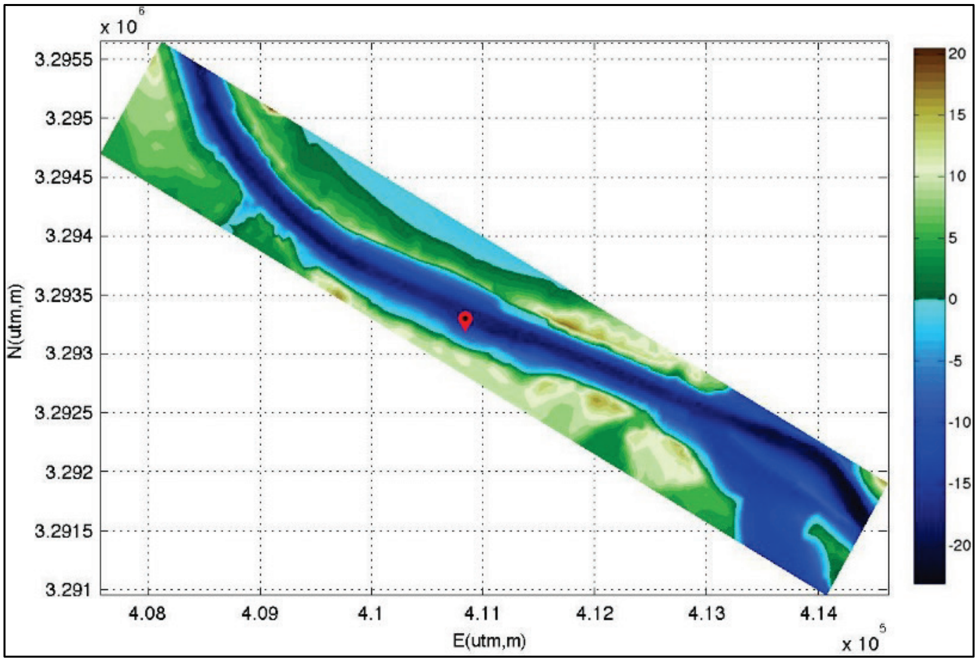

Figure 11 shows the depth change (top panel) with red for deposition and blue for erosion and sediment concentration (bottom panel). Most sediments are suspended near the shoreline, causing erosion. For additional details on the sediment transport and morphology change module in FUNWAVE-TVD, please refer to Malej et al. (2019).

2.3 Automatic Identification System (AIS) data

A goal was to validate the model against field measurements reported in Zaloom et al. (2017). In that report, data were collected using Aquadopp Profilers to monitor waves in the Port Arthur area (Gauge1; Figure 7) and the Golden Pass LNG Terminal dock (Gauge2; Figure 4), each location for two different time periods:

- Gauge1: Port Arthur area
  - 4 May 2016 14:21:01, to 11 May 2016 13:11:01 (1 week)
  - 12 May 2016 14:31:0 to 26 May 2016 10:01:01 (2 weeks)

Figure 5. Grid: Gauge2up. The colorbar of bathymetry and topography elevation is in meters.

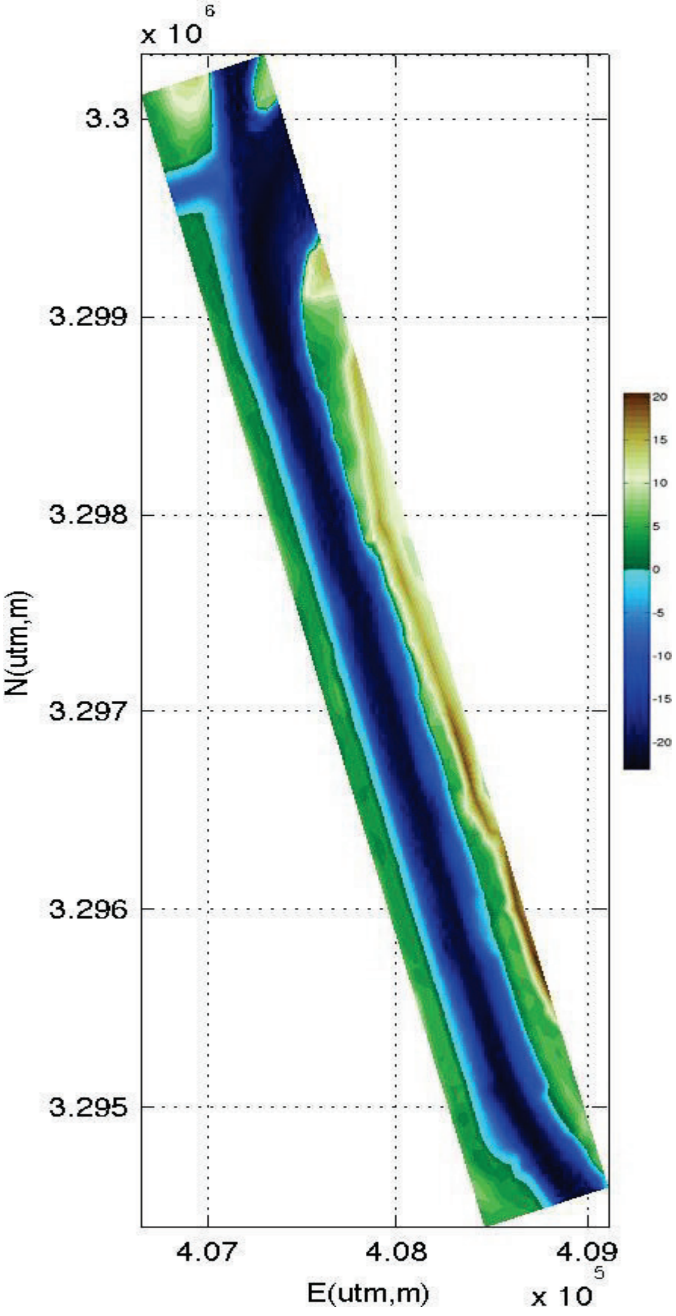

Figure 6. Grid: Turner. The colorbar of bathymetry and topography elevation is in meters.

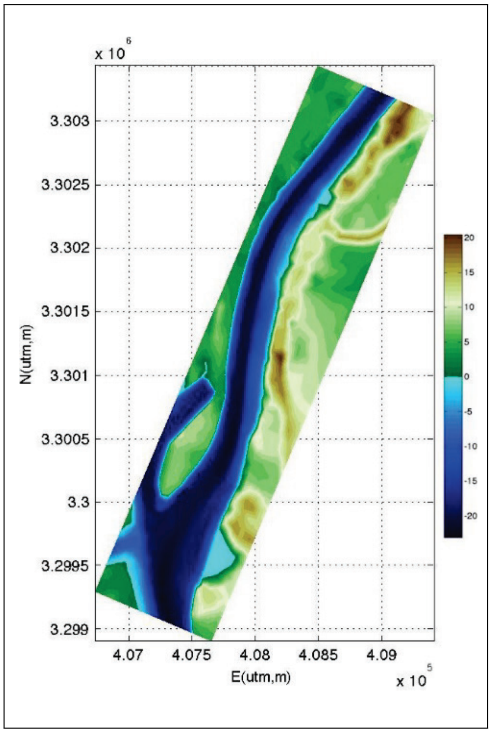

Figure 7. Grid: Gauge1. The red pin drop represents a relative location of Gauge 1 in the Port Arthur area contained in the report of Zaloom et al. (2017). The colorbar of bathymetry and topography elevation is in meters.

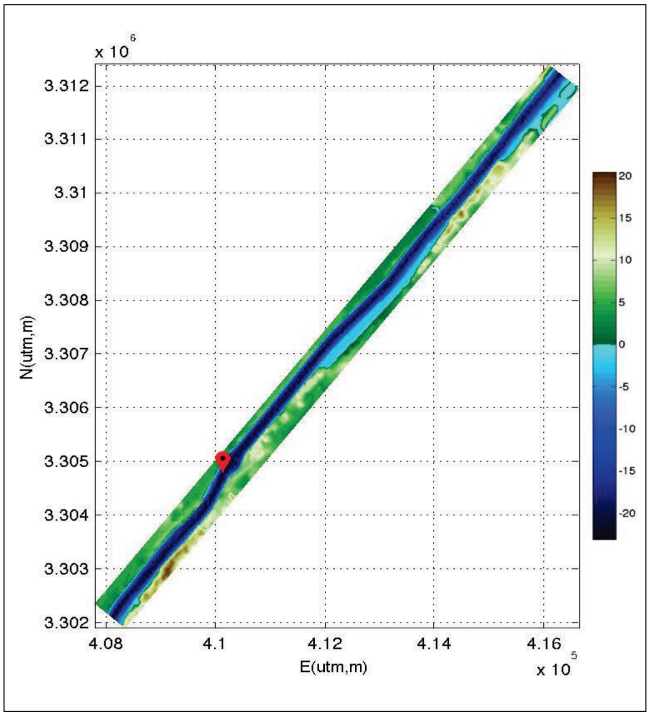

Figure 8. Test run with 5.0 m resolution.

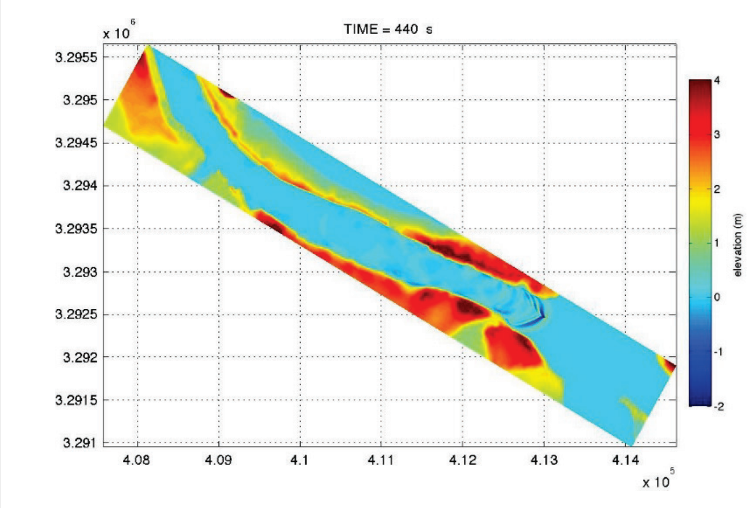

Figure 9. Test run with 1.0 m resolution.

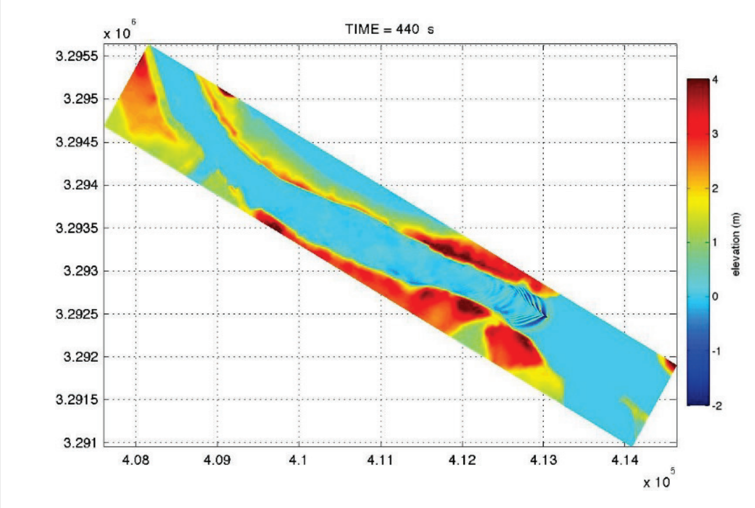

Figure 10. A close look at ship-wakes in the case of 1.0 m resolution.

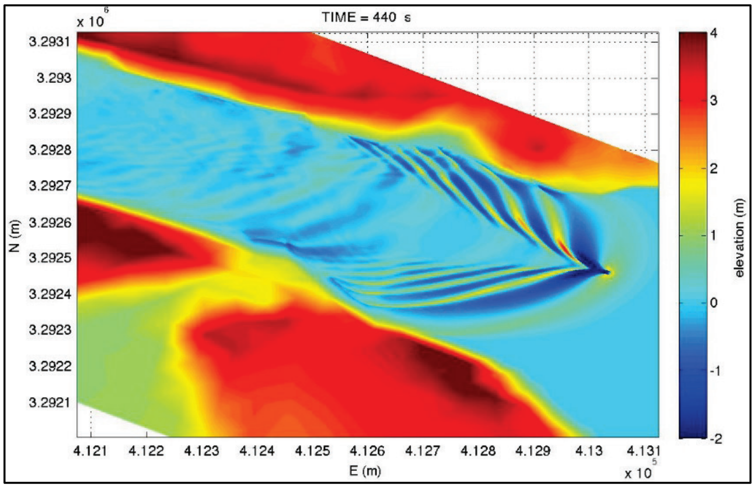

Figure 11. Results from the sediment module. The top plot represents the depth change before and after the vessel passage in meters whereas the bottom plot shows the sediment concentration in milligrams per liter in a logarithmic scale.

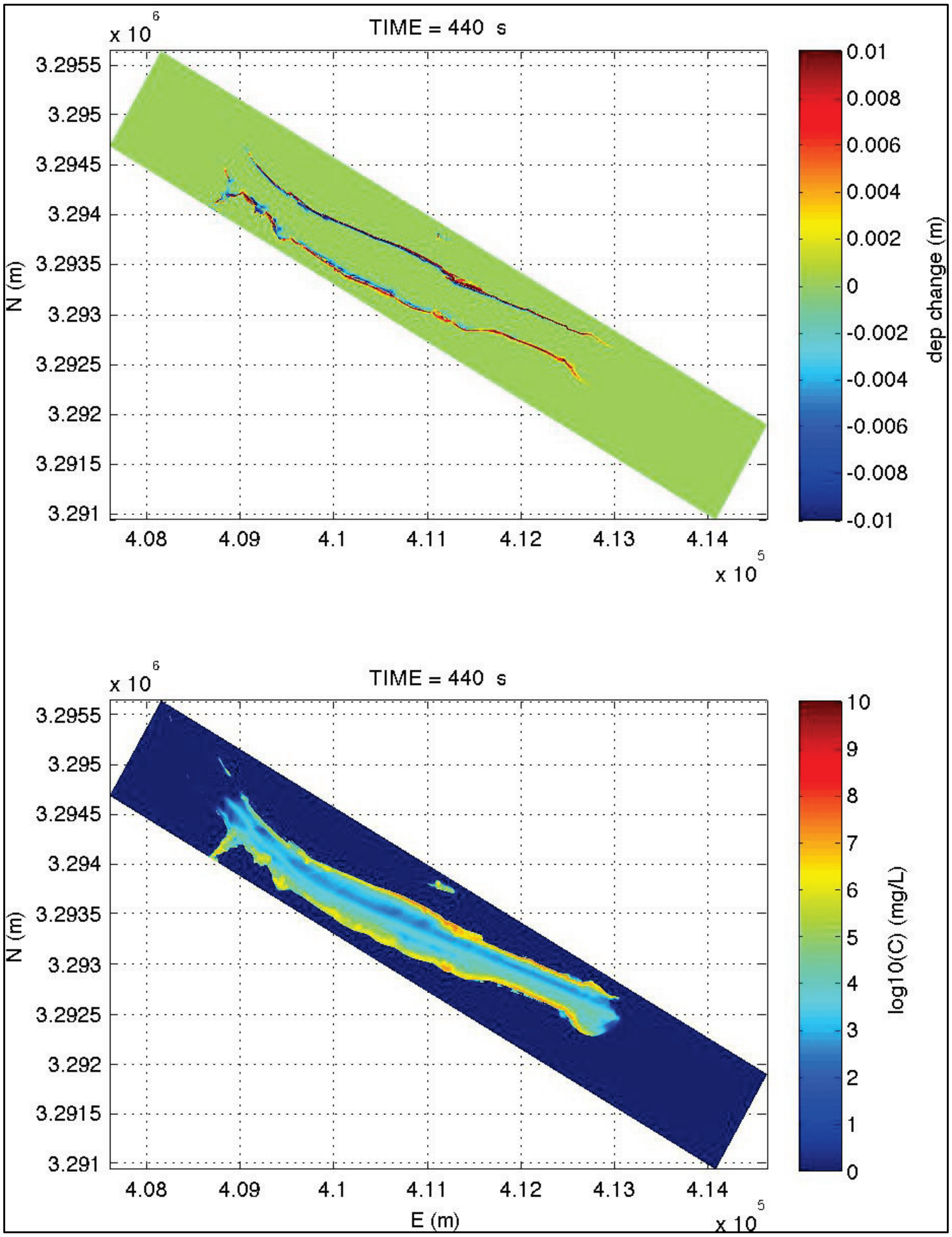

- Gauge2: Golden Pass LNG Terminal dock
    - 11 January 15: 01:01 2017 to 25 May 2017, 13:41:01 (2 weeks)
    - 30 January 13: 41:01 2017 to 15 February 2017, 10:02:01 (2 weeks)

To collect vessel traffic to be used in FUNWAVE-TVD, ERDC AIS Analysis Package (AISAP) was used (USACE 2020), a web-based interface to AIS data collected by the US Coast Guard (USCG) and USACE.

2.3.1 Data collection considerations

While AISAP is a useful tool for collecting bulk vessel traffic information, there are several limitations to the dataset that must be considered for use both inside and outside FUNWAVE.

- AIS, or the need to have a Global Positioning System (GPS) transponder on board a vessel, is only required by commercial vessels.
- AISAP does not locally store all the AIS data collected by USCG and USACE but caches any data previously requested.
- AISAP limits the amount of new data that may be requested per query for normal uses; however, email requests may be made to AISAP to automate (batch) queries.
- Not all data are always reported by AIS (e.g., ship draft).
- AIS data are not always reported at regular intervals.
- Even though the reported longitude/latitude data are within 0.0001 min of accuracy (approximately 0.2 m), the actual vessel location may be up to 10 m off, or even 50 m if certain equipment is not present. Furthermore, the GPS position may not accurately represent the center of the vessel, especially for large vessels with lengths over 100 m. For the FUNWAVE ship-wake generation mechanism, however, it is assumed that the location of the vessel is its exact center point.

2.3.2 Data collection procedure

In general, there are recommended steps for requesting traffic data from AISAP:

- Convert the UTM coordinates of the subdomains’ corners back into longitude/latitude.
- Import the longitude/latitude positions of each subdomain’s corners into AISAP to set up Area of Interest (AOI) for AISAP to perform analysis on (Figure 12).
- Check if any previously cached data exist that lie within AOIs – none found for the time intervals in the report of Zaloom et al. (2017).

- If previously cached data do not exist, select the region of interest (Figure 13) and set the time interval to be queried.

Figure 12. AOIs created in AISAP, correlated with Figure 2.

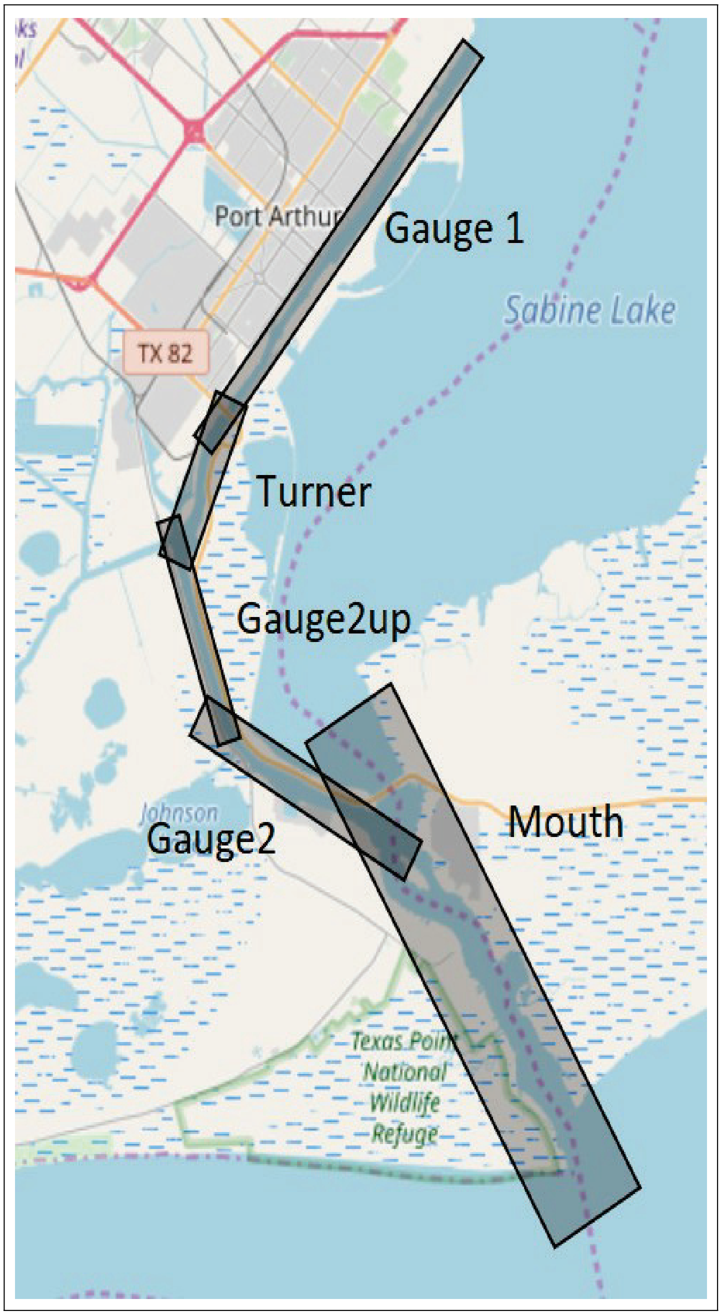

Figure 13. Data collection region used in AISAP.

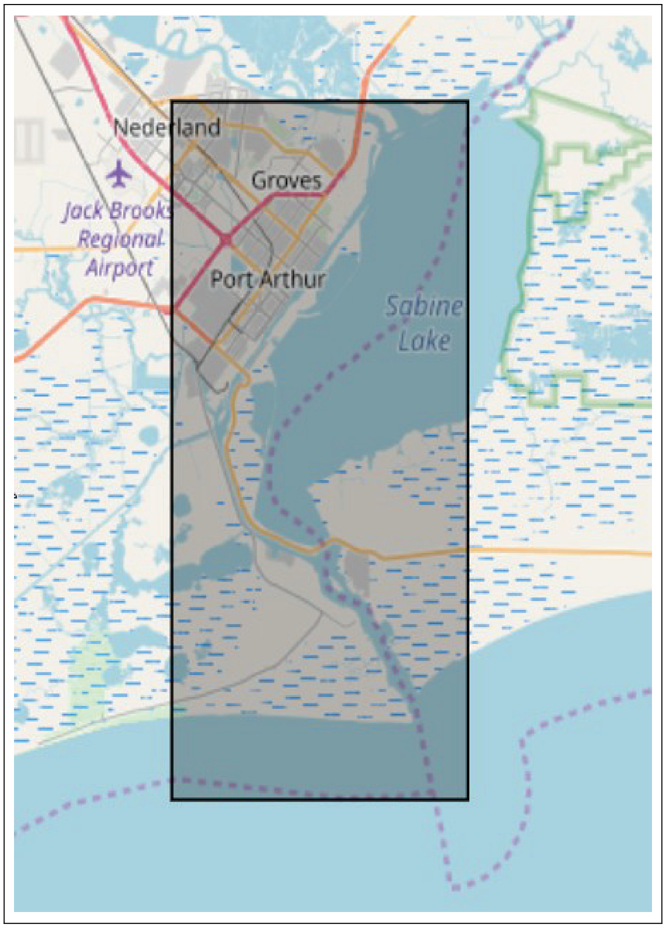

For accurate FUNWAVE simulations, high temporal resolution of the vessel position is required. Such data are not typical of the average AISAP user as high temporal resolution data are generally not required for their purposes.

Therefore, a special request is made to AISAP for these data. Typically, once the request is entered into the ASIAP system, there is an average wait time of a day or two to get through the queue and another day or two for the request to be processed and the data to be made available. These times, however, depend on the current load on the system and the amount of traffic in the AOI.

2.3.3 Vessel path corrections

As mentioned before, while the longitude/latitude AIS data are reported within 0.0001 min of precision, the actual error in the ship location may be higher. This can be seen in the AIS data in several ways:

- Between time stamps the longitude/latitude position does not change even though the vessel speed indicates that the position should have changed.
- Computing the speed numerically (using the ratio of the distance between two consecutive vessel coordinates in AIS time series and the time-step between them) results in rapid variations in the speed that do not match AIS speed data even when considering the accuracy in the reported speed.
- Removing data points where the vessel's location does not change does not sufficiently correct these rapid variations.

To correct this issue, a combination of cubic spline interpolation and a linear least squares fit method was implemented. The basic corrective steps are as follows:

- Using a clamped cubic splines method (Bartels et al. 1993), the coefficients of the cubic splines are expressed in terms of some arbitrary grid point values, typically using an equispaced grid with approximately a tenth of the number points in raw data performs best.
- Using a linear least square method, the coefficients (expressed in terms of the arbitrary grid point values) are fitted to the raw function's values (position) and its derivative values (velocity).
- The AOIs are rotated to rectangular regions (for FUNWAVE) and the origin is shifted to (0,0) (improves accuracy of fitting scheme).
- The AIS data is mapped to the transformed AOI regions.
- Using the AIS data for the vessels speed over ground and course over ground, the x and y components of the velocity are extracted.
- The cubic splines are fitted to the vessel's position and its velocity in each direction, separately, see Figures 14 and 15.
- For some vessel paths, see Figure 16, this method significantly reduces the jaggedness of a vessel's path (top), producing a more realistic path(bottom).

The last point (jaggedness of the vessel path) is subtle, but rather important. If the vessel path is not smooth enough, particularly during turning, the sudden jump in the position of the vessel body (pressure or flux cavity from submerged vessel body) causes spurious transverse waves, with the vessel acting like a paddle-type wavemaker.

There are several possible improvements to this procedure.

- The fitting scheme uses a clamped cubic spline method which assumes the acceleration is zero at the boundaries, which may be causing the increased error at the boundaries. Switching to a natural cubic spline method may correct this.
- There are oscillations in the fitted speed that appear to correlate with the discontinuities in the AIS speed data. A smoothing procedure may be used to give a good approximation to a continuous speed track within the AIS error ranges, thus smoothing out the spurious path oscillations.

Figure 14. Top: Distance between the fitting procedure results and AIS data (blue dots) and the estimated error range reported for all AIS data due to instrumentation (black dashed horizontal line), showing splines do not exceed it. Bottom: Comparison between the reported AIS path (thick red curve) and the path produced by the cubic splines linear least-square procedure (black curve).

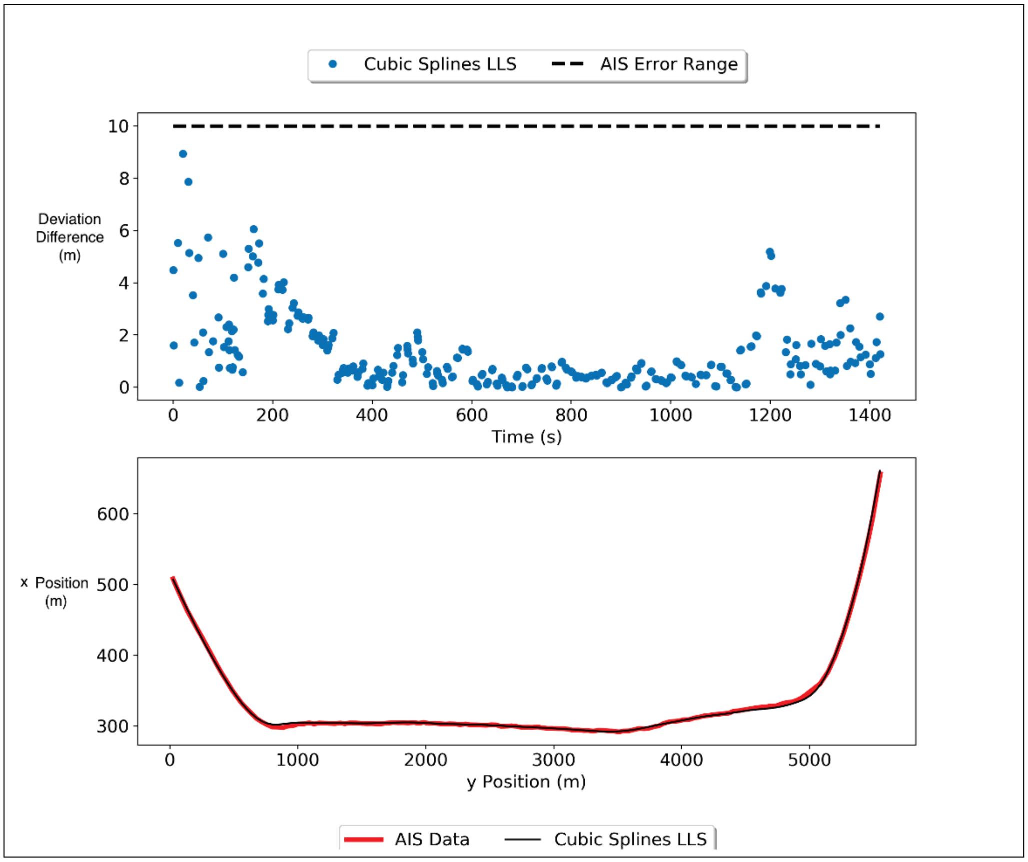

Figure 15. Top three: Comparison between velocity/speed computed numerically from AIS position data via central time difference between two adjacent vessel location points (blue dots) and the instantaneous speed reported by AIS data (red line), ignoring points where to position does not change; and the velocity/speed computed using the fitting procedure (black line). Bottom: Difference between the speed computed from AIS position data and AIS speed data (orange diamonds), and the difference between speed produced by the fitting procedure and AIS speed data (blue dots), and the accuracy range in the report AIS speed (dashed black horizontal line).

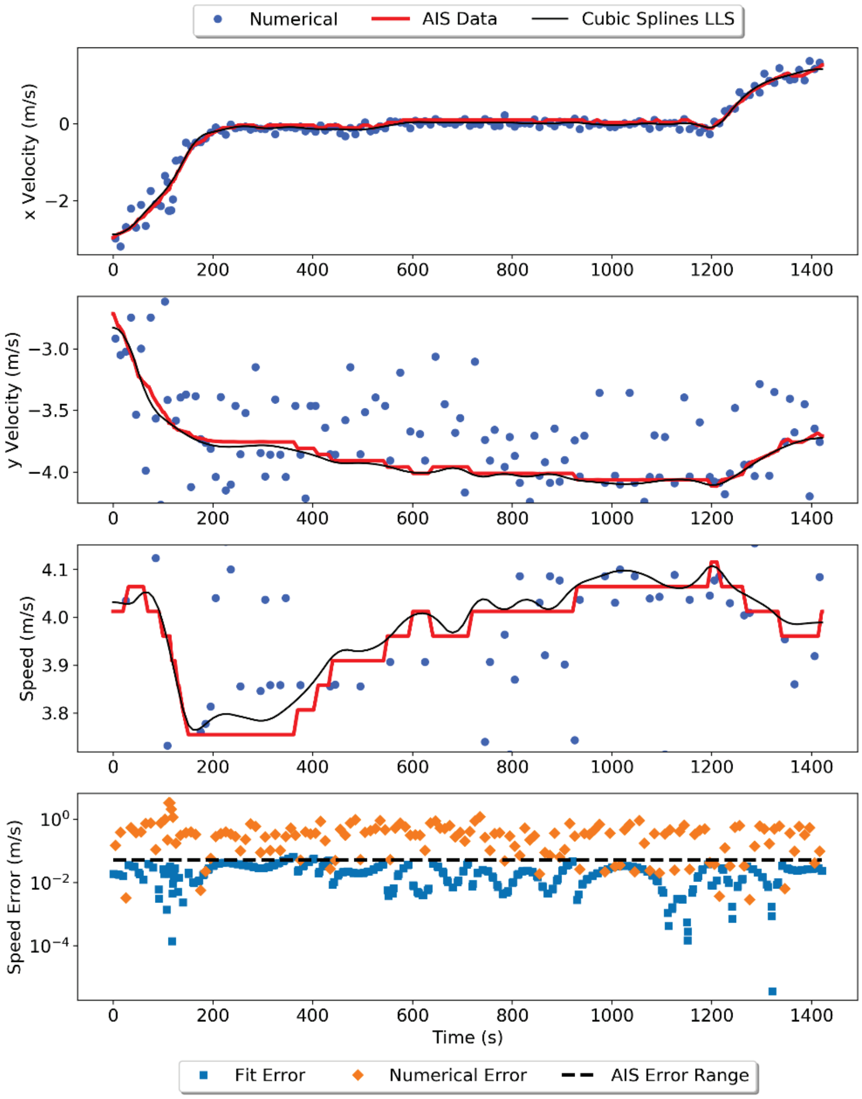

Figure 16. Comparison between the vessel path using the raw AIS data (top) and the smoothed vessel path using the cubic splines least linear squares method (bottom).

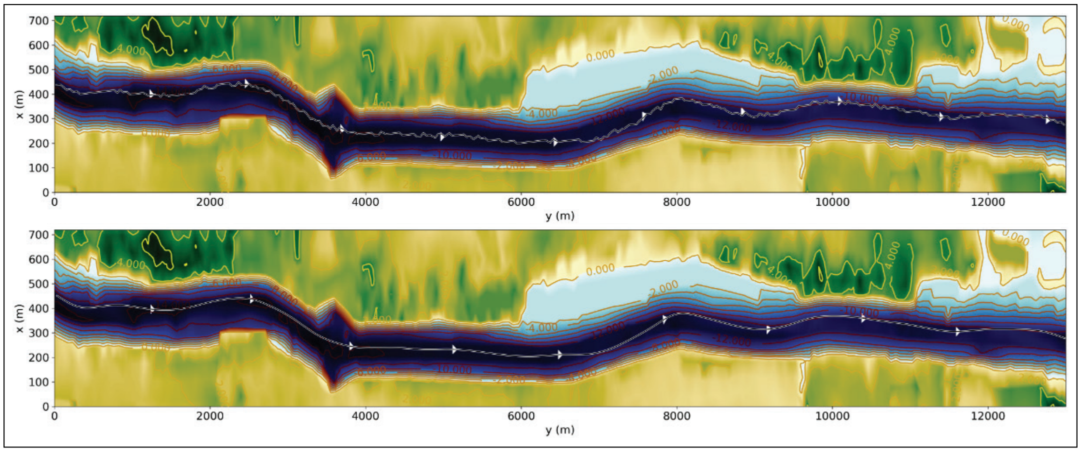

2.4 Vessel types

Various types of source functions for ship-wave generation have been implemented. The current ship-wave module in FUNWAVE offers four different generation mechanisms, two based on the pressure-type source and two based on the flux-type source, which is limited to the slender-body theory. The general equations are presented below, along with references to additional details in published literature.

2.4.1 Pressure source TYPE I

Following Ertekin et al. (1986), Wu (1987), and Torsvik et al. (2009), the pressure disturbance with a center point at (x^*, y^*) is given by

$$p_a(\tilde{x}, \tilde{y}, t) = P f(\tilde{x}, t) q(\tilde{y}, t) \tag{1}$$

where

$$f(\tilde{x}, t) = \begin{cases} \cos^2\left[\frac{\pi(\tilde{x} - x^*(t) - \frac{1}{2}\alpha_1 L)}{(1-\alpha_1)L}\right], & \frac{1}{2}\alpha_1 L < \tilde{x} - x^*(t) \le \frac{1}{2}L \\ \cos^2\left[\frac{\pi(x^*(t) - \tilde{x} - \frac{1}{2}\alpha_2 L)}{(1-\alpha_2)L}\right], & -\frac{1}{2}L \le \tilde{x} - x^*(t) < -\frac{1}{2}\alpha_2 L \\ 1, & -\frac{1}{2}\alpha_2 L \le \tilde{x} - x^*(t) \le \frac{1}{2}\alpha_1 L \end{cases} \tag{2}$$

$$q(\tilde{y},t) = \begin{cases} \cos^2\left[\frac{\pi(|\tilde{y}-y^*(t)|-\frac{1}{2}\beta W)}{(1-\beta)W}\right], & \frac{1}{2}\beta W < |\tilde{y}-y^*(t)| \leq \frac{1}{2}W \\ 1, & |\tilde{y}-y^*(t)| \leq \frac{1}{2}\beta W \end{cases} \tag{3}$$

In the rectangle $-L/2 \leq \tilde{x} - x^*(t) \leq L/2$ and $-W/2 \leq \tilde{y} - y^*(t) \leq W/2$, and zero outside this region, L and W represent the length and width (vessel beam) of the pressure source, respectively. α_1, α_2, and β are parameters representing the shape of the draft region and $0 \leq (\alpha_1, \alpha_2, \beta) < 1$. They can be evaluated using the block coefficient of a watercraft as described below. $(\tilde{x}, \tilde{y})$ is the coordinate system for the pressure disturbance, which may be rotated by an angle relative to the Boussinesq coordinate system (x, y). P is a parameter controlling the surface displacement, or draft of the vessel. In fact, p_a is the static depression around the vessel. In contrast to the formulation of the pressure distribution in the previous studies, such as Torsvik et al. (2009), P has a unit of meters and can be interpreted as the inverse barometer effect corresponding to the static surface depression for a stationary vessel.

The values of α_1, α_2, and β are hull shape/curvature parameters and can be obtained by adjusting α_1, α_2 and β to get the displaced volume (static submerged volume of the vessel)

$$V_{\text{sub}} = \iint p_a \, d\tilde{x} \, d\tilde{y} \tag{4}$$

which should match a given block coefficient C_B defined by

$$C_B = \frac{V_{\text{sub}}}{L \cdot W \cdot D} \tag{5}$$

in which D represents draft of a vessel. Examples of the pressure and vessel shape for different values of α_1, α_2, and β are shown in Figure 17 through Figure 19.

Note that because of the pressure source TYPE I formulation, the canonical equations can be scaled to arrive at an elegant analytical formulae for both the block ratio coefficient C_B and the midship section area coefficient C_M. Specifically, if you let

$$\begin{aligned} \hat{x}(t) &= \frac{[\tilde{x} - x^*(t)]\cos\theta(t) + [\tilde{y} - y^*(t)]\sin\theta(t)}{L} \\ \hat{y}(t) &= \frac{-[\tilde{x} - x^*(t)]\sin\theta(t) + [\tilde{y} - y^*(t)]\cos\theta(t)}{W} \end{aligned} \tag{6}$$

with $\theta(t)$ defined as the heading computed from the vessel's next position, i.e.,

$$\theta(t) = \mathrm{arctan2}(y^*(t + \Delta t_{\mathrm{ves}}) - y^*(t),\ x^*(t + \Delta t_{\mathrm{ves}}) - x^*(t)) \tag{7}$$

where Δt_{ves} is the time-step to the next position of the vessel. Note that the ship-wake generation function is now defined in a unit area box, $-1/2 < \hat{x}(t) < 1/2$ and $-1/2 < \hat{y}(t) < 1/2$. The pressure source TYPE I equations defined in (1) can now be rewritten in terms of $\hat{x}$ and $\hat{y}$ yielding

$$p_a(\hat{x}, \hat{y}, t) = \begin{cases} P f(\hat{x}, t) q(\hat{y}, t), & |\hat{x}| \le \frac{1}{2} \text{ and } |\hat{y}| \le \frac{1}{2} \\ 0, & \text{otherwise} \end{cases} \tag{8}$$

where

$$f(\hat{x},t)=\begin{cases}\cos^2\left(\frac{\pi(\hat{x}(t)-\frac{1}{2}\alpha_1)}{(1-\alpha_1)}\right), & \frac{1}{2}\alpha_1<\hat{x}(t)\le\frac{1}{2}\\ \cos^2\left(\frac{\pi(\hat{x}(t)+\frac{1}{2}\alpha_2)}{(1-\alpha_2)}\right), & -\frac{1}{2}\le\hat{x}(t)<-\frac{1}{2}\alpha_2\\ 1, & -\frac{1}{2}\alpha_2\le\hat{x}(t)\le\frac{1}{2}\alpha_1\end{cases} \tag{9}$$

$$q(\hat{y},t)=\begin{cases}\cos^2\left(\frac{\pi(|\hat{y}(t)|-\frac{1}{2}\beta)}{(1-\beta)}\right), & \frac{1}{2}\beta<|\hat{y}(t)|\le\frac{1}{2}\\ 1, & |\hat{y}(t)|\le\frac{1}{2}\beta\end{cases}$$

Under this scaling, the coefficients become

$$C_B=\frac{V_{\text{sub}}}{L\cdot W\cdot D}=C_M\int_{-1/2}^{1/2}f(\hat{x},t)\,d\hat{x} \tag{10}$$

and

$$C_M=\int_{-1/2}^{1/2}q(\hat{y},t)\,d\hat{y} \tag{11}$$

Finally, the midship section area coefficient (C_M) and the block coefficient (C_B) can be integrated exactly in closed form yielding

$$C_M=\frac{1+\beta}{2}\quad\text{and}\quad C_B=\frac{(2+\alpha_1+\alpha_2)C_M}{4}=\frac{(2+\alpha_1+\alpha_2)(1+\beta)}{8} \tag{12}$$

Note that if you are given the midship section area coefficient C_M, you can easily obtain β. However, when presented with the block coefficient C_B, you can only come up with a functional expression for α_1 in terms of α_2, or vice versa. Another third equation/relationship is needed to get closure. In practice, one can elect to have α_1 simply be a factor of α_2, or a special case of the bow and stern be numerically symmetric, thus equating α_1 with α_2.

2.4.2 Pressure source TYPE II

TYPE II of the pressure-type source has a slender body shape and is formulated following Bayrakter and Beji (2013). David et al. (2017) used this formulation in their tests. The pressure source can be written as

$$p_a(\tilde{x},\tilde{y},t) = P\left[1 - a(\tilde{x}/L)^4\right]\left[1 - b(\tilde{y}/W)^2\right]e^{-c(\tilde{y}/W)^2} \tag{13}$$

where a, b, and c are form parameters. For a slender body, $a = 16.0$, $b = 2.0$ and $c = 16.0$. Here, $0 < a \le 16$ controls the shape of the vessel in the lengthwise direction, and $0 < b \le 4$ and $c > 0$ control the shape of the vessel shape in the width direction, with c being the parameter primarily forming the slender body shape. Setting $b < 4$ or $a < 16$ gives the vessel sharp edges on their respective sides. Examples of the pressure and vessel shape for different values of a, b, and c are shown in Figures 20 through 23. As in section 2.4.1 above, one can obtain a closed-form solution for the block and mid-ship area coefficients under the same scaling. However, the final expression is a bit more complicated as it contains an erf(z) error function. The erf(z) function is well tabulated in engineering manuals, or it can also be approximated through a power series expansion, especially for small quantities.

Hence, under the same scaling as in Equation (6), the pressure source is defined as

$$\begin{aligned} f(\hat{x},t) &= \left(1 - a\left[\hat{x}(t)\right]^4\right) \\ q(\hat{y},t) &= \left(1 - b\left[\hat{y}(t)\right]^2\right)\mathrm{e}^{-c[\hat{y}(t)]^2} \end{aligned} \tag{14}$$

where $0 \le a \le 16$, $0 \le b \le 4$ and $c > 0$. The midship section area coefficient (C_M) and the block coefficient (C_B) can be integrated exactly, yielding

$$C_M = \frac{b\,\mathrm{e}^{-c/4}}{2c} - \frac{\sqrt{\pi}(b-2c)\,\mathrm{erf}\left(\frac{\sqrt{c}}{2}\right)}{2c^{3/2}} \quad \text{and} \quad C_B = \left(1-\frac{a}{80}\right)C_M \tag{15}$$

where the error function (erf) is defined by

$$\mathrm{erf}(z) = \frac{2}{\sqrt{\pi}}\int_0^z \mathrm{e}^{-t^2}\,dt \tag{16}$$

and can be approximated to a desired degree of accuracy. For instance, for a degree of accuracy to be on the order of 10^{-4}, one can replace Equation (16) with

$$\mathrm{erf}(z) \approx 1 - \frac{1}{(1+a_1 z + a_2 z^2 + a_3 z^3 + a_4 z^4)^4} \tag{17}$$

where $a_1 = 0.278393$, $a_2 = 0.230389$, $a_3 = 0.000972$, and $a_4 = 0.078108$.

2.4.3 Slender body TYPE I

The flux-type sources are based on the slender body theory. Here, these kinds of sources are referred to as “Slender Body TYPE.” For the flux-type source, the additional volume flux induced by ship motion is applied in the mass conservation equation.

$$dQ = F * \sin(2\pi(\tilde{x} - x^*(t)/L) * \cos(2\pi(\tilde{y} - y^*(t))/W) \tag{18}$$

where dQ represents the flux gradient. F is a parameter, which can be determined by the block ratio. The formula is calculated in a rectangle $-L/2 \le \tilde{x} - x^*(t) \le L/2$ and $-W/2 \le \tilde{y} - y^*(t) \le W/2$ and is zero outside of this region.

2.4.4 Slender body TYPE II

The TYPE II of the slender source is similar to the TYPE I but with two additional parameters representing sizes of the bow and stern.

$$dQ = \begin{cases} F * \sin(2\pi(\tilde{x} - x^*(t) - \frac{1}{2}\alpha_1 L)/(1-\alpha_1))L) * \cos(\pi\tilde{y}/W), \\ \qquad\qquad\qquad\qquad \frac{1}{2}\alpha_1 L < \tilde{x} - x^*(t) \le \frac{1}{2}L \\ F * \sin(2\pi(\tilde{x} - x^*(t) + \frac{1}{2}\alpha_2 L)/(1-\alpha_2)L) * \cos(\pi\tilde{y}/W), \\ \qquad\qquad\qquad\qquad -\frac{1}{2}L \le \tilde{x} - x^*(t) < -\frac{1}{2}\alpha_2 L \\ 0, \qquad\qquad\qquad\qquad -\frac{1}{2}\alpha_2 L \le \tilde{x} - x^*(t) \le \frac{1}{2}\alpha_1 L \end{cases} \tag{19}$$

The formula is calculated in the rectangle $-L/2 \le \tilde{x} - x^*(t) \le L/2$ and $-W/2 \le \tilde{y} - y^*(t) \le W/2$ and is also zero outside of this region.

Figure 17. Example of the vessel pressure and shape with default parameters of $\alpha 1 = 0.5$, $\alpha 2 = 0.5$, and $\beta = 0.5$ for pressure source 1 given by (1).

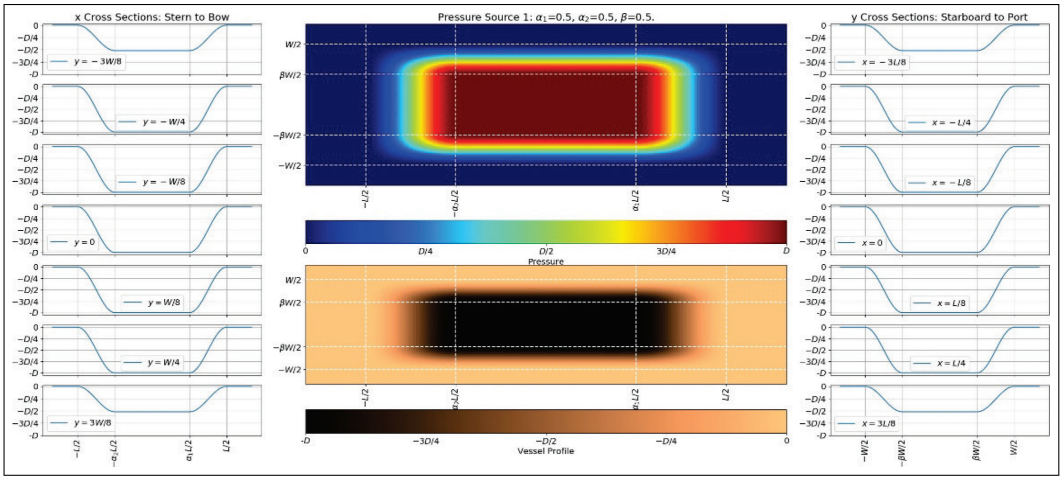

Note that to the best of the authors' knowledge, the slender body type sources, including Pressure Source TYPE II, Slender Body TYPE I and II, have not been validated using large-size vessels such as tankers and container ships.

Figure 18. Example of modifying the shape of the bow (α1) and stern (α2) of the vessel with $\alpha1 = 0.25$, $\alpha2 = 0.75$, and $\beta = 0.5$ for pressure source 1 given by Equation (1).

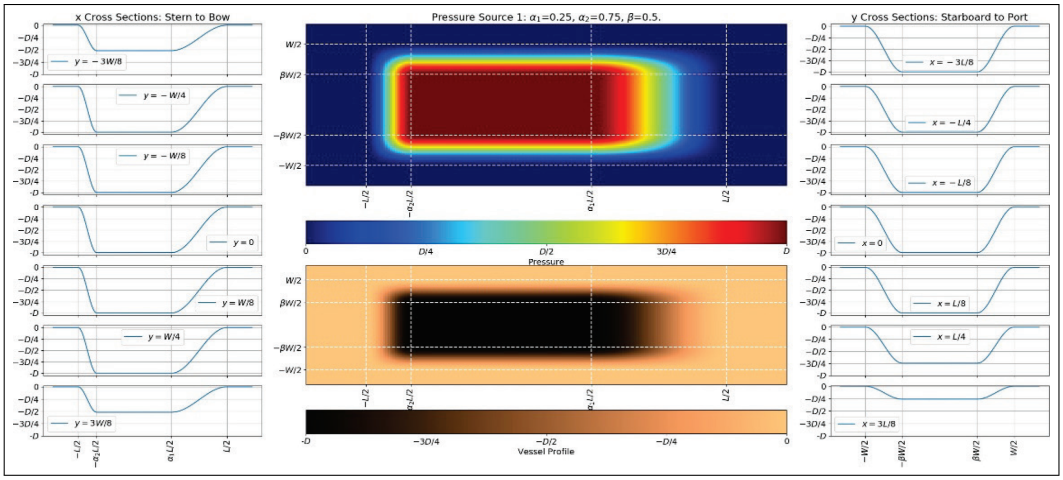

Figure 19. Example of modifying the shape of the starboard to port cross section (β) of the vessel with $\alpha1 = 0.5$, $\alpha2 = 0.5$, and $\beta = 0.3$ for pressure source 1 given by Equation (1).

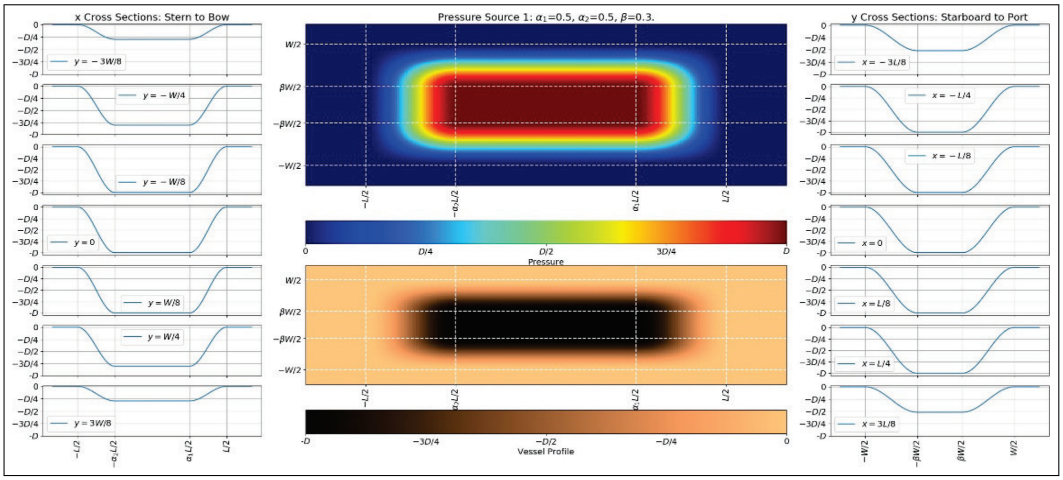

Figure 20. Example of the vessel pressure and shape with default parameters of a=16, b=2, and c=16 for pressure source 2 given by Equation (13).

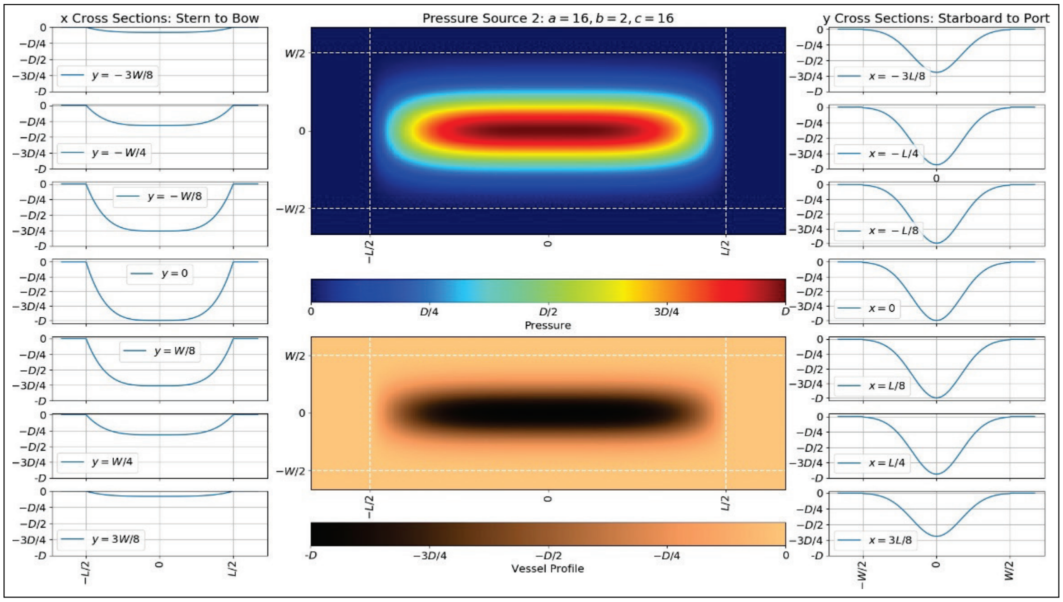

Figure 21. Example of modifying the shape of the stern to bow cross section of the vessel with a=8, b=2, and c=16 for pressure source 2 given by Equation (13). Note the vertical jumps at the bow and stern ends.

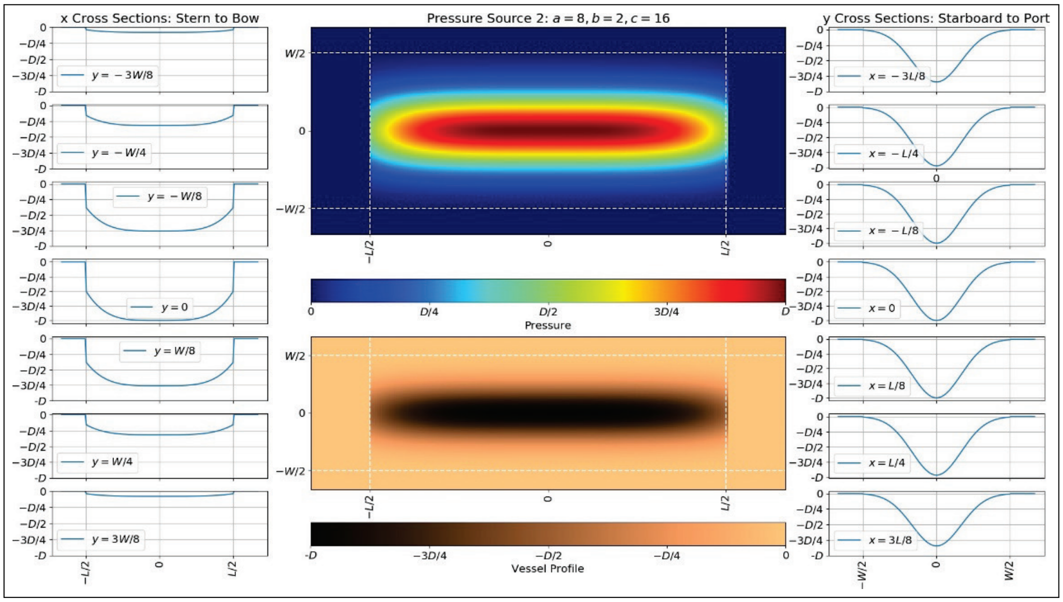

Figure 22. Example of modifying the shape of the starboard to port cross section of the vessel with a=16, b=1, and c=16 for pressure source 2 given by Equation (13).

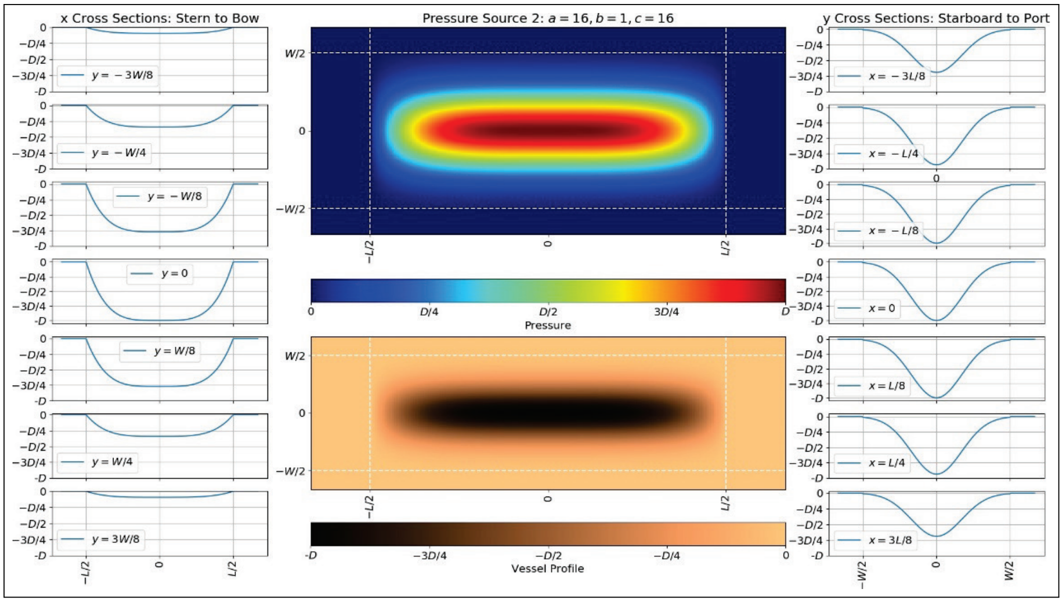

Figure 23. Example of modifying the shape of the starboard to port cross section of the vessel a=16, b=2, and c=4 for pressure source 2 given by Equation (13). Note the vertical jump at the starboard and port ends which are smoothed out in Figure 20.

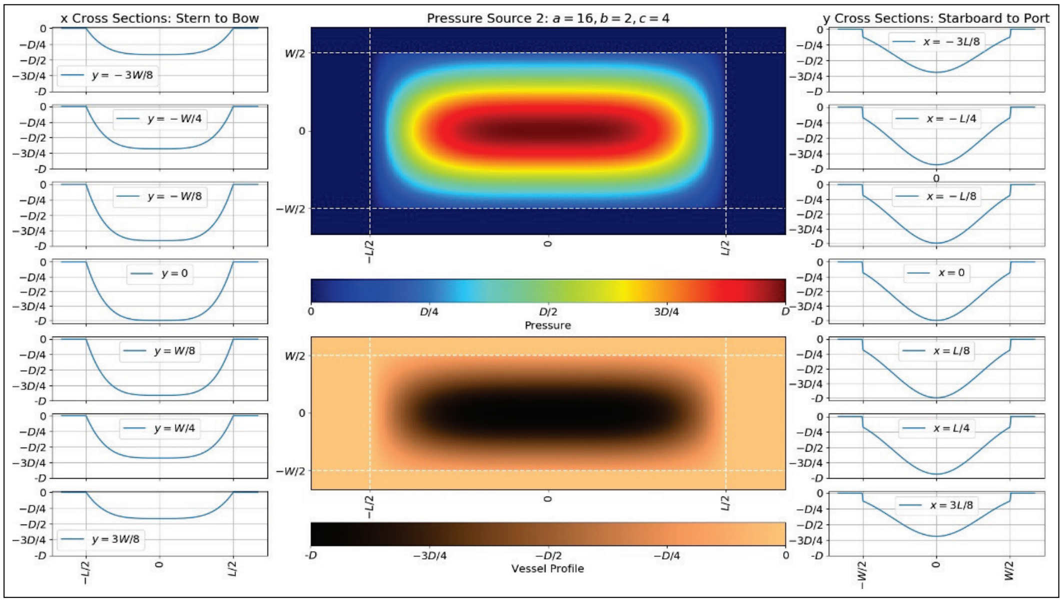

2.5 Sediment transport and morphological evolution

The (non-cohesive) sediment transport module is based on the depth-averaged sediment concentration equation

$$(\bar{c}H)_t + \nabla_h \cdot (\bar{c}\mathbf{M}) = \nabla_h \cdot (kH(\nabla_h \bar{c})) + P - D \tag{20}$$

where $\nabla_h = (\partial/\partial x, \partial/\partial y)$ is the horizontal two-dimensional (2D) gradient, $\bar{c}$ is the non-dimensional depth-average sediment concentration normalized by the sediment density, $\mathbf{M}$ is the flow rate per unit width, k is the horizontal sediment diffusion coefficient, $H = h + \eta$ is the total water depth with h being the undisturbed water depth and η being the free-surface elevation, P is the pickup of new sediment from the floor bed, and D is the deposition of sediment. The sediment diffusion coefficient computed using Elder (1959)

$$k = 5.93 u_{*c} H \tag{21}$$

with the shear velocity calculated by van Rijn (1984)

$$u_{*c} = \frac{\kappa}{-1 + \log(30H/k_s)} U_c \tag{22}$$

where U_c is the depth-average total velocity, κ is the von Karman constant equal to 0.41, $k_s = 2.5 d_{50}$ is the Nikuradse roughness coefficient, and d_{50} is the median grain diameter.

The pickup function is computed using van Rijn (1984)

$$P = 0.015 \frac{d_{50}}{a} \left(\frac{|\tau_b| - \tau_{cr}}{\tau_{cr}} \right) \tag{23}$$

where $a = 0.01H$ is a reference elevation, τ_b is the bed shear stress, τ_{cr} is a critical shear stress for erosion to occur, and d_* is a dimensionless grain size.

The dimensionless grain size is defined as

$$d_* = d_{50}\left(\frac{(s-1)\,g}{\nu^2}\right)^{1/3} \tag{24}$$

where g is gravity, ν is the kinematic viscosity coefficient, and s is the specified gravity of the sediment. The bed shear stress is as follows

$$\tau_b = \rho_w\left(\frac{0.5}{1+\ln(k_s/30h)}\right)^2 U_c^2 \tag{25}$$

where h is the undisturbed water depth, and ρ_w is the water density (default: 1027 kg/m3). The critical shear stress, above which erosion occurs, is expressed as

$$\tau_{cr} = \rho_w(s-1)gd_{50}\theta_{cr} \tag{26}$$

where θ_{cr} is the critical Shields parameter.

The deposition rate is computed using Cao (1999)

$$D = \gamma\bar{c}w_f(1-\gamma\bar{c})^2 \tag{27}$$

where $\gamma = \min[2, 1 - n/\bar{c}]$, n is the sediment porosity, $\bar{c}$ is again the non-dimensional depth-average sediment concentration normalized by the sediment density, and w_f is the settling velocity (default: 125 m/s).

The evolution of the seabed is due to sediment transport and is governed by the following depth (Z_b) change equation

$$\frac{d\bar{Z}_b}{dt} = \frac{1}{1-n}\left(\bar{D} - \bar{P} - \nabla \cdot \bar{\mathbf{q}}_b\right) \tag{28}$$

$\bar{Z}_b$ is the time-averaged depth change with positive values for erosion and negative values for deposition. $\bar{P}$ and $\bar{D}$ are the time-averaged pickup and deposition rates, respectively, averaged over the morphological time-step (dt_{morph}) in the suspended load model. The $\bar{\mathbf{q}}_b$ represents the bedload flux vector averaged over the same time interval, and its scalar bedload transport formula follows Meyer-Peter and Müller (1948):

$$\bar{q}_b = \frac{8\left[\left(\tau_b - \tau_{cr}\right)/\rho_w\right]}{g(s-1)} \tag{29}$$

Note that seabed changes occur at a relatively slower time scale compared to the general wave dynamics in FUNWAVE; therefore, to speed up the computation times, Equation (20) is time averaged and solved over a multiple of the normal FUNWAVE time-step (dt) – typically a multiple between 5 and 20 produces an optimal balance between speed and accuracy. For additional details on the sediment transport and morphology change modules in FUNWAVE, see Malej et al. (2019).

3 FUNWAVE – Field Validations

This section shows two validation experiments against field data. The first one comes from the Lamar University and University of Houston report (Zaloom et al. 2017), and the second one is from ERDC/CHL TR-03-15 (Maynord 2003). Both data sets have their intrinsic limitations, and in both situations, there is only the comparison of numerical results against digitized image plots. In Appendix A, a sample FUNWAVE input file with a list of common input parameters is presented.

3.1 Validation against two vessels from the Lamar University and University of Houston report

In this sub-section, FUNWAVE simulation results are compared with a small field data set (mainly two vessels from a digitized image) in the Lamar University and University of Houston report (Zaloom et al. 2017). Note that there is no complete certainty on the exact locations of the wave gauges that were reported; thus, approximate locations were used in the simulations. These are in close proximity of what is believed to be the gauge locations. For the wave gauge at the Golden Pass area, note that the bathymetry data are missing the Golden Pass terminal (south area of map in Figure 25), and placing the gauge in 298 m from the water center line as reported in Zaloom et al. (2017) results in the gauge being above ground. Therefore, a station location was chosen such that it is sufficiently deep (8.5 m vs. 15 m in the report) to reduce the effects of short waves and to be sufficiently far away from the water center line (180 m). The location of the numerical wave gauge in the Port Arthur area is shown in Figure 26.

For the initial set of simulations, $\alpha_1 = \alpha_2 = \beta = 0.5$ for pressure source TYPE I in Equation (1) was chosen, which resulted in midship section area coefficient $C_M = 0.75$ and the block coefficient $C_B = 0.5625$. These values are reasonable, albeit slightly smaller than common coefficient values for deep-draft vessels like oil tankers, etc. In Figure 24, example block coefficient (C_B) values for some deep-draft tankers and container-type vessels are shown.

Subsequently, for the pressure source TYPE II, the authors started with $a = c = 16$ and $b = 2$ in Equation (13); this yielded a midship section area coefficient $C_M = 0.414$ and block coefficient $C_B = 0.331$. For the slender source TYPE I, $F = 1$ in Equation (18) was initially chosen; followed by F

= 1 and $\alpha_1 = \alpha_2 = 0.8$ for slender source TYPE II in Equation (19). All the simulations were performed in ERDC DoD Supercomputing Resource Center (DSRC), utilizing high performance computing (HPC) clusters, including Onyx and Topaz. The details of the model setup (ship waves and corresponding sediment/morphology change) and input/driver files were somewhat complex and different from each other but can be furnished to the sponsor upon request.

Figure 24. Sample deep-draft vessel block coefficients (CB) from Barrass (2004).

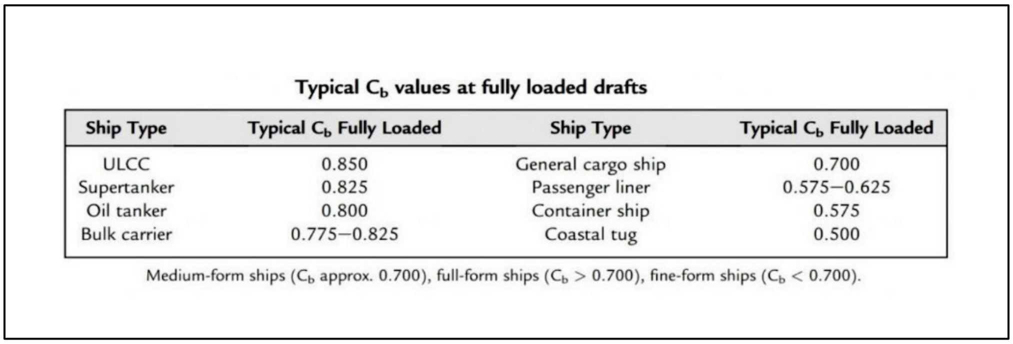

Typical C_b values at fully loaded drafts

Ship Type	Typical C_b Fully Loaded	Ship Type	Typical C_b Fully Loaded
ULCC	0.850	General cargo ship	0.700
Supertanker	0.825	Passenger liner	0.575–0.625
Oil tanker	0.800	Container ship	0.575
Bulk carrier	0.775–0.825	Coastal tug	0.500

Medium-form ships (C_b approx. 0.700), full-form ships ($C_b > 0.700$), fine-form ships ($C_b < 0.700$).

Figure 25. Station location in FUNWAVE simulations in Golden Pass area. Note that the bathymetry data are missing the Golden Pass terminal (South area of map in Figure 28) and placing the gauge 298 m from the water center line as reported in Zaloom et al. (2017), results in the gauge being above ground. Therefore, a station location was chosen such that it is sufficiently deep (8.5 m vs. 15 m in the report) to reduce the effects of short waves and to be sufficiently far away from the water center line (180 m).

The authors first discuss results for a Liquefied Petroleum Gas (LPG) tanker called *BW Leo* (whose dimensions were length = 225 m, beam/width = 36 m, and the maximum draft = 12 m) in the Golden Pass channel for pressure source TYPE I, TYPE II, and slender source TYPE I and II (Figure 27). It may be seen that pressure source TYPE I captures the approximate period (200 sec) and magnitude (0.2 m) of the drawdown wave; however, the wave peak right after the major depression, often referred to as the surge part of the TSW, is not accurately captured. It seems that the model is breaking those surge waves with high-enough wave surface slope and distributing/dissipating that energy. Hence, the visible difference between the model and field data.

Figure 26. Station location in FUNWAVE simulations in the Port Arthur area.

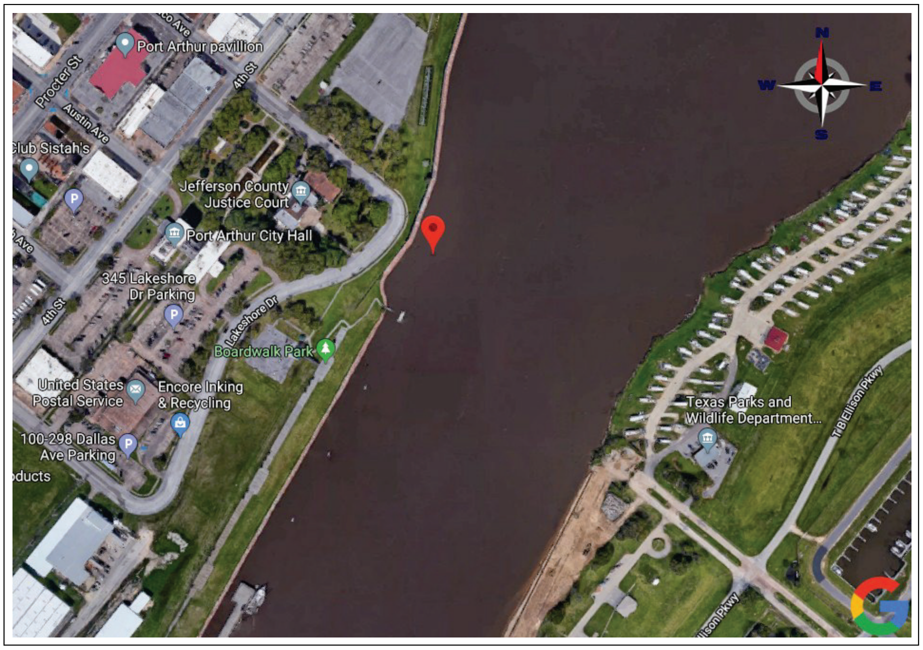

Pressure source TYPE II and slender source TYPE I and II have similar signals as pressure source TYPE I. However, the wave heights are smaller, particularly for the slender TYPE II. Note that the differences between field data and simulation data may be due to the simulation bathymetry data missing the Golden Pass Terminal, resulting in the wave gauge location being a compromise between the gauge location and depth reported in Zaloom et al. (2017). Despite that, the model with the pressure source TYPE I captured the drawdown part of the TSW wave with a correct wave magnitude. In contrast, the remaining pressure and flux source types predicted a smaller trough of the drawdown wave.

For illustration purposes, in Figure 28 the resulting vessel-generated wave system is shown in the vicinity of the Golden Pass. The wave field was generated by the *BW Leo* with the above-mentioned initial parameters using the pressure source TYPE I methodology. The red pin represents the location of the wave gauge and the orange polygon shows the area that was not considered wet (under water) during our simulation. Meaning, the satellite map image is the most current one whereas the bathymetry/topography maps had that area designated as a dry spot (above water). Thus, it is likely that this area was modified and/or dredged from the time the bathy/topo surveys were taken. Also, the pointy bow is only drawn to show the vessel path direction and is not a true representation of the designed/utilized bow shape. Finally, note that in Figure 28, there is a visible difference in tide levels, as well. As mentioned before, the satellite image is from the most current setting whereas simulations were done with correct water level corresponding to the reported time of the data collection. The tidal range for the area is approximately 0.45 m, and the tidal current is not significant (Maynord 2003). Because of that and the fact that the vessel speeds were calculated over ground from the AIS system, thus being in the correct reference frame, there was no vessel-speed adjustment made numerically to account for the tidal current. For large tidal currents (~ 2 m/sec), it is not a matter of just including tidal currents but modeling the tide and tidal currents in the entire channel. This is achievable in FUNWAVE, but it requires one-way boundary coupling to a forcing grid, which would impose desired free-surface fluctuations and currents (flow velocities) at the channel boundary/entrance.

Figure 27. Comparison between FUNWAVE simulation results for different vessel types with default shape parameters and field data for the *BW Leo* in the Golden Pass channel. The length, width, and applied draft of the vessel were equal to 225 m, 36 m, and 8.1 m, respectively.

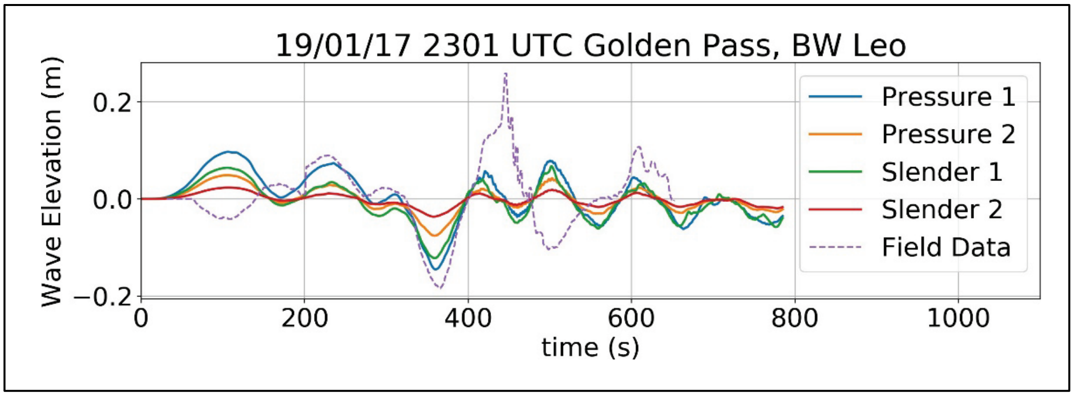

The second vessel considered was a crude oil tanker called *NS Champion* (whose dimensions were length = 244 m, beam/width = 42 m, and the maximum draft = 15.38 m) in the Port Arthur channel, shown in Figure 29. Similar to the simulation for the *BW Leo*, for pressure source TYPE I, the drawdown wave is captured but with a different period (135 s vs. 110 s) and slightly different magnitude (0.33 m vs. 0.28 m). In contrast to the *BW Leo* simulations, the pressure source TYPE II and slender source TYPE I and II have similar signals as pressure source TYPE I. However, their respective wave height of the drawdown wave is much smaller. In contrast to *BW Leo*, the steepness of the surge wave following the drawdown for *NS Champion* is not as high. As such, the model appears to resolve the surge wave better in this case without breaking those waves prematurely. This may also be related to the fact that in this location the *NS Champion* is much closer to the channel banks than *BW Leo*, not allowing the nonlinearity to shoal the surge wave as much.

Figure 28. Simulated wave field showing the traditional drawdown primary wave with satellite overlay from FUNWAVE for the *BW Leo* in the Golden Pass channel area, with default shape/size parameters for pressure source TYPE I. The red pin represents the location of the wave gauge, and the orange polygon shows the area that was not considered wet (under water) during the simulation. The pointy bow is drawn only for illustration purposes to show the vessel direction and is not a true representation of the designed bow shape. Additional minor visual discrepancy is from numerical simulations using correct water levels whereas the satellite image shows a snapshot at a low tide.

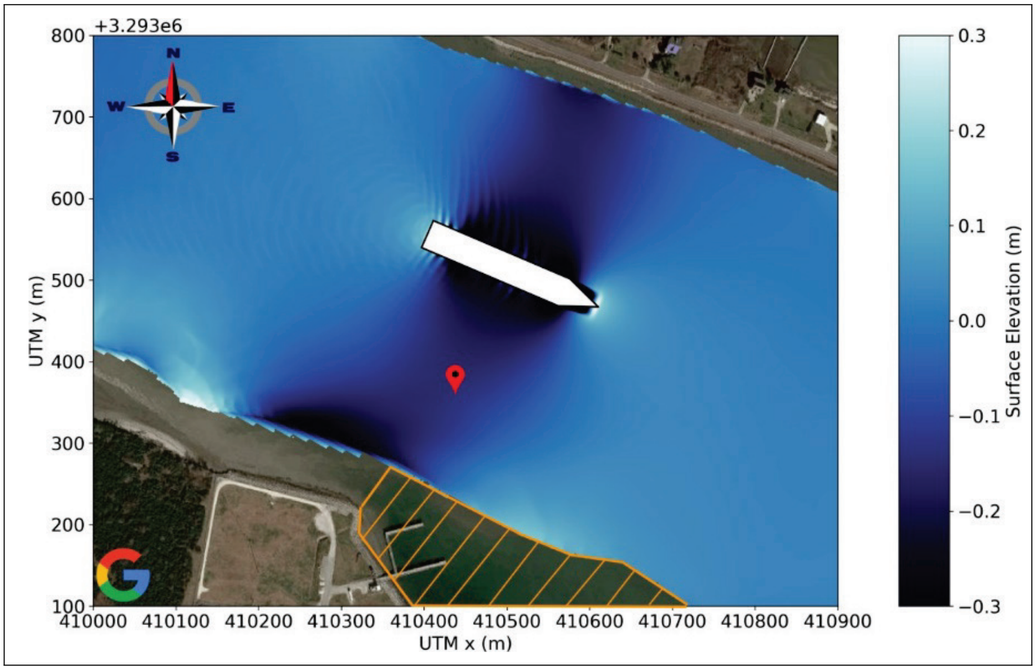

Also, similar to *BW Leo* validation, the resulting vessel-generated wave system around Port Arthur from *NS Champion* with the above-mentioned initial parameters for pressure source TYPE I is shown for illustration purposes in Figure 30. The red pin represents the location of the wave gauge, and the orange polygon shows the area that was not considered wet (under water) during the simulation. This means that the satellite map image is the most current one whereas the bathymetry/topography maps corrected with the appropriate water level had that area designated as a dry spot (above water). It is also likely that this area was modified and/or dredged from the time the bathy/topo surveys were taken. Note that the pointy bow is only drawn to show the vessel path direction and is not a true representation of the designed/utilized bow shape.

In Figure 31, the results for the effects of varying one of the vessel parameters for pressure source TYPE I, Equation (1) are plotted while keeping all the other parameters fixed at their default values given earlier. In the left column, the wave height (blue) and period (orange) of the primary drawdown wave computed from simulations are plotted, with the corresponding values from the field data denoted with the horizontal dashed line. In the right column, the L_2 error between simulation results and field data over only the time period of the drawdown wave of the field data (red) and relative percentage difference between the maximum drawdown extent (deepest trough) between field and simulation (red) are plotted. The vertical dashed black line corresponds to the value of the original parameter used in Figure 27. The L_2 error is defined as

$$L_2[\eta_{\mathrm{Sim}}(t), \eta_{\mathrm{Fld}}(t)] = \frac{\sqrt{\int_a^b \left[\eta_{\mathrm{Sim}}(t) - \eta_{\mathrm{Fld}}(t)\right]^2\ dt}}{\sqrt{\int_a^b \left[\eta_{\mathrm{Fld}}(t)\right]^2\ dt}} \tag{30}$$

where η_{Sim}(t) is the free-surface elevation at the gauge from simulations, $\eta_{\mathrm{Fld}}(t)$ is the free-surface elevation from field data, and a and b are the bounds of the time interval of interest. Note that the dependence of the wave height and period on parameters are mostly in phase. Looking at the L2 measure of the drawdown wave itself, it may be seen that the overall error is relatively large, indicating that the signal does not match field data well. However, using this type of metric will be sensitive to phase-shifts (Figure 27).

Figure 29. Comparison between FUNWAVE simulation results for different vessel types with default shape parameters and field data for the *NS Champion* in the Port Arthur channel. The length, width, and draft of the vessel are equal to 234 m, 42 m, and 8 m, respectively.

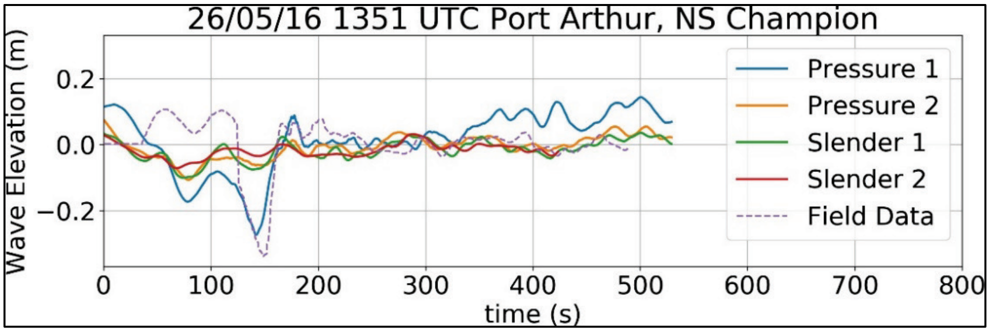

Figure 30. Simulated wave field showing the traditional drawdown primary wave with satellite overlay from FUNWAVE for the *NS Champion* in the Port Arthur channel area, with default shape/size parameters for pressure source TYPE I. The red pin represents the location of the wave gauge, and the orange polygon shows the area that was not considered wet (under water) during the simulation. The pointy bow is drawn only for illustration purposes to show the vessel direction and is not a true representation of the designed bow shape.

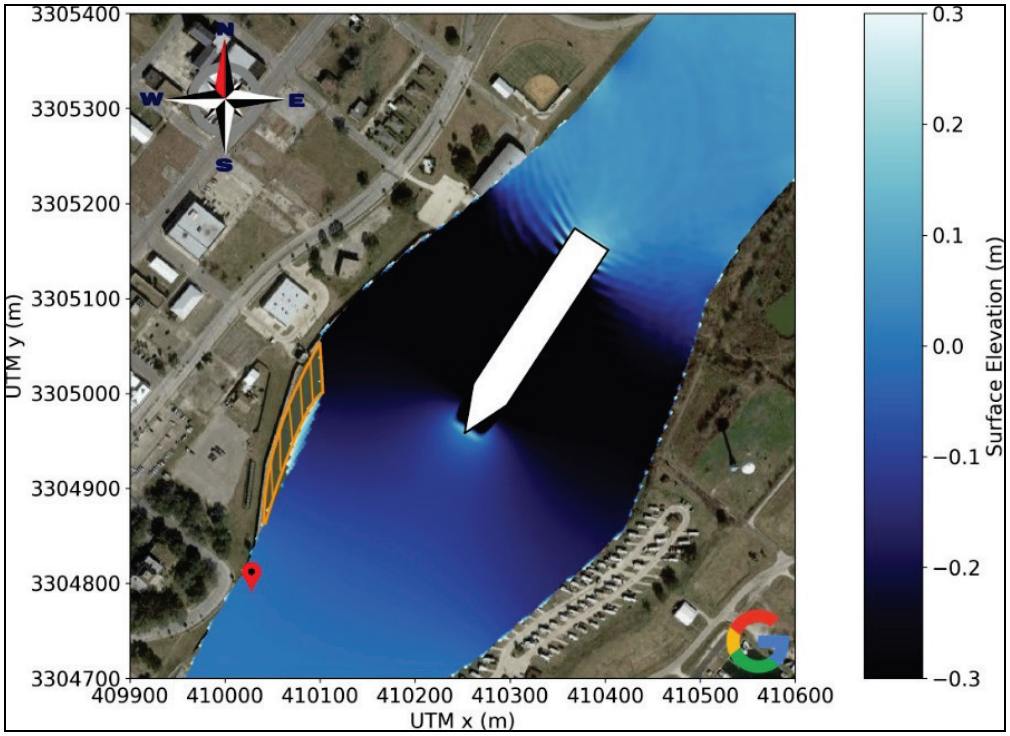

The L_2 error in the drawdown wave is below 0.5 for most simulations and may be as low as 0.05, where the latter indicates a relatively good match with the data. Focusing on which parameters to change, it appears that increasing the draft to approximately 9.0 m would minimize the L_2 errors for the drawdown wave and closely match the wave height and period of the drawdown wave, as well. This change would be considered reasonable as the AIS data reported a draft of 8.1 m while Zaloom et al. (2017) reported a draft of 11.7 m. Furthermore, slightly increasing the vessel's length to approximately 250 m would provide a good match to field data while the reported vessel width (beam) gives a decent compromise between matching the wave height and period. However, while it is reasonable to assume that the vessel draft may change in time and is not always reported accurately by vessel's AIS systems, the width and length should be fixed and accurate. It is therefore more reasonable to alter the vessel's shape parameters (α_1, α_2, and β) to better match field data. Analyzing the results for the shape parameters, it appears that $\alpha_1 = 0.625$, $\alpha_2 = 0.5$, and $\beta = 0.75$ give the best match to field data. These parameters yield the midship section area coefficient $C_M = 0.875$ and the block coefficient $C_B = 0.684$, which slightly underestimates the typical block coefficients for large cargo ships and oil tankers (Figure 24).

In Figure 32, a similar parameter study as in Figure 31 for pressure source TYPE II, contained in Equation (13) is presented. Note that a parameter study was not performed for parameter a due to instability issues, which appear to be due to a sharp vessel bow with $a < 16$ (Figure 21).

This claim is equally supported by instabilities occurring also for pressure source TYPE I with large α_1 (i.e., sharpening of the bow), hence the lack of data points in Figure 31 for $\alpha_1 > 0.625$.

Analyzing the results in Figure 32, note that with the exception of parameter c, the vessel parameters have little effect on the wave height of the drawdown wave, and only the vessel length and width significantly affect the period of the drawdown wave. Results show that only the parameter c has significant effect on the period and wave height of the drawdown wave. Albeit, with all the considered parameter permutations (in the current set of simulations), it was not possible to completely match the wave height of the drawdown wave in the field data. Results for the L_2 norms show that the error in the drawdown wave height is between 0.4 and 0.7 and is likely due to pressure source 2 not generating a sufficiently large drawdown wave compared to the field data.

In Figure 33, a parameter study for the *NS Champion* in the Port Arthur area with pressure source TYPE I is presented. Similar to the *BW Leo*, the dependence of the wave height and period on vessel parameters is mostly in phase. However, unlike the results for the *BW Leo*, the signal from simulation results contains more noise, resulting in extracted quantities having more dependence on vessel parameters. Results indicate that the shape parameters $\alpha_1 = 0.275$, $\alpha_2 = 0.275$, or $\beta = 0.375$ would provide the best compromise to match the wave height and wave period. These parameters would equate to the midship section area coefficient $C_M = 0.6875$ and the block coefficient $C_B = 0.4383$, an underestimation of block coefficients typical of oil tankers (Figure 24). Moreover, slightly decreasing the vessel length to 230 m, the vessel width to 40 m, or the draft to 7.6 m, would better match the field data. Note that the draft for the *NS Champion* reported in Zaloom et al. (2017) is 10.2 m. Results for the maximum wave height and the L_2 error norm show that error is mostly due to simulation data settling to a different height than the field data for $t > 300$ in Figure 29. The L_2 error over the drawdown wave is approximately 0.5 for all simulations and is most likely due to the small dip within the main drawdown wave observed in simulations at $t = 75$ in Figure 29.

Figure 31. Effects of vessel parameters for *BW Leo* using pressure source TYPE I, Equation (1), on wave height (left column, blue curve) and period (left column, orange curve) and L2 norm of the drawdown wave, computed with Equation (30), on the subdomain of the field data (right column, red curve) and drawdown maximum extent in surface elevation only (right column, green curve). Note that negative values indicate an underestimation while positive values (in percentages) indicated overestimation. Period and wave height of the drawdown wave computed from field data are given by the horizontal dashed lines, and the default vessel parameters are denoted by the vertical dashed black lines.

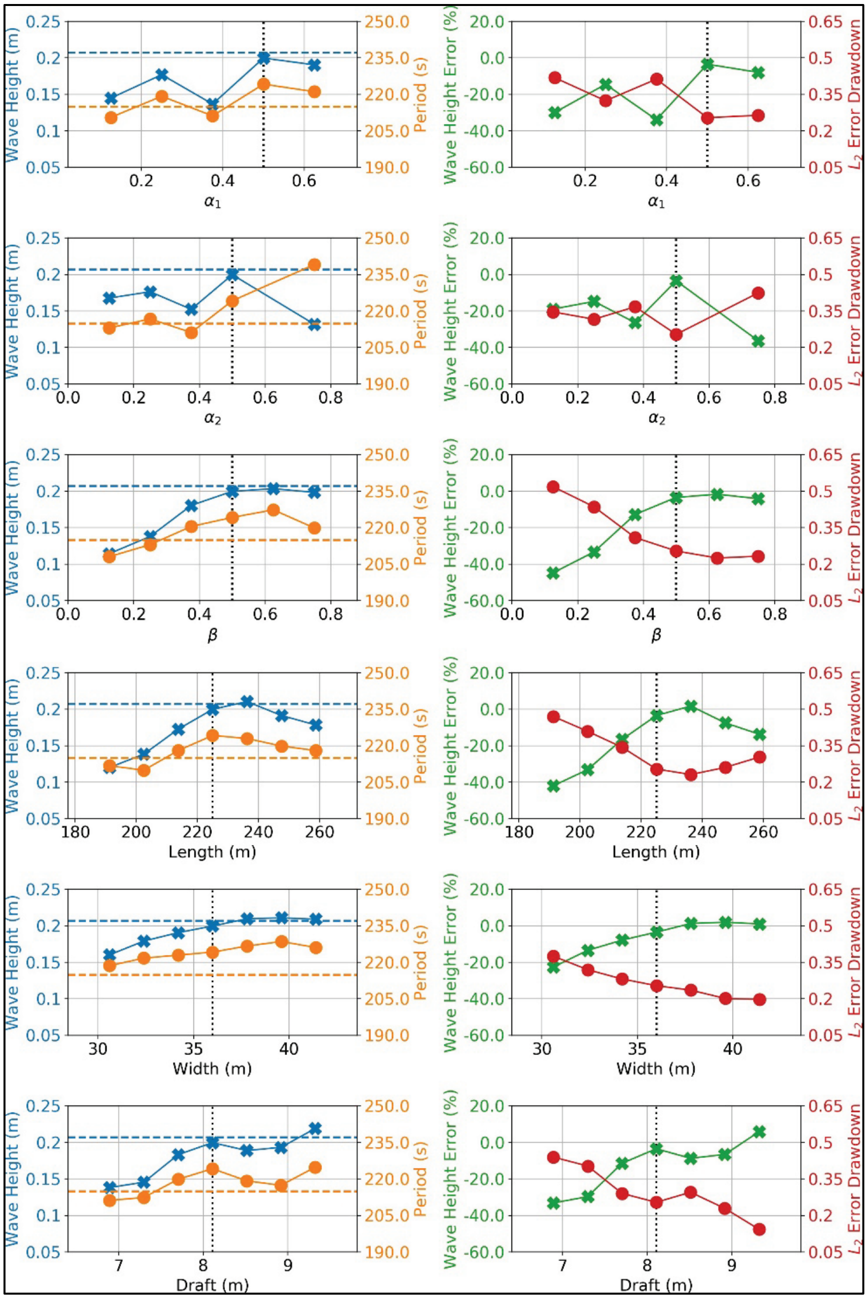

Figure 32. Effects of vessel parameters for *BW Leo* using pressure source TYPE II, Equation (13), on wave height (left column, blue curve) and period (left column, orange curve) of the drawdown wave, and L_2 norm, computed with (30), on the drawdown wave time subdomain of the field data (right column, red curve) and drawdown wave height relative percentage difference (right column, green curve). Period and wave height of the drawn down wave extracted from field data are given by the horizontal dashed lines (left column), and the default vessel parameters are denoted by the vertical dashed black lines.

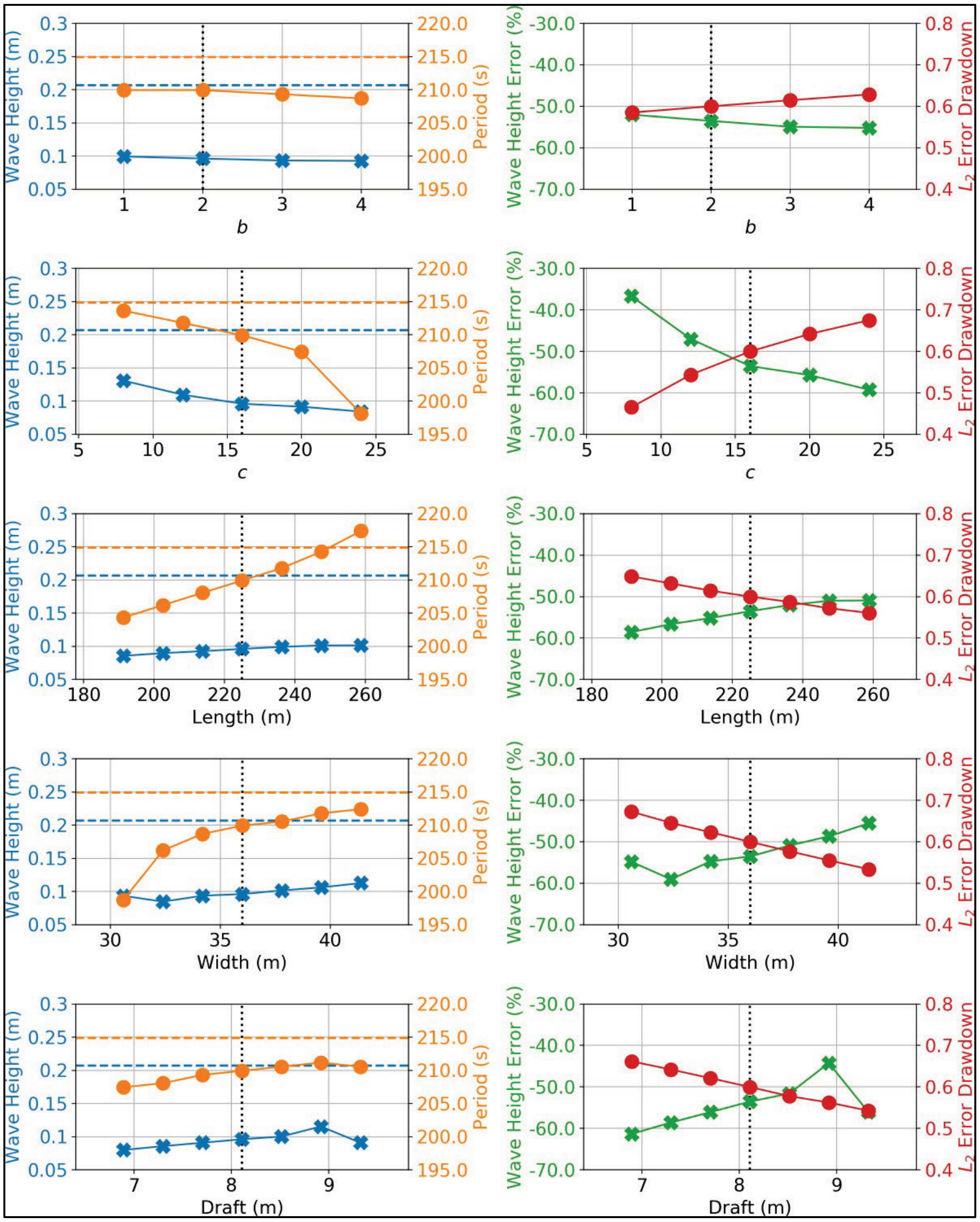

A parameter study for pressure source TYPE II is not presented because of the method not being able to accurately depict the drawdown wave in the original design. However, note that similar to the *BW Leo* (Figure 32), vessel parameters have little influence on the wave height of the drawdown wave.

Ultimately, the pressure source TYPE I methodology yields best overall results qualitatively, and its parameter space (generally +/- 50%) yields most robust quantitative results, as well. It is acknowledged that more quantitative studies, aside from the two studied vessels, are desirable. In addition, there is still some unresolved uncertainly as to the exact location of the wave gauges and validity of the field data from the report of Zaloom et al. (2017). The scarcity of vessel tracks and unresolved questions about the methods of analysis of the remaining data in that report (e.g., calculating significant wave height (H_{sig}) of such episodic events like ship wakes) does not provide an ad equate framework for comparing numerics against field data in a true/fair environment. As it stands, however, the authors are advocating that pressure source TYPE I will be the methodology utilized for scour/erosion hot spots determination in the subsequent section.

3.2 Validation against one vessel (*Pacific Sapphire*) from ERDC/CHL TR-03-15 (Maynord 2003)

In this subsection is a discussion of the numerical simulation results against inbound and outbound vessel paths of the tanker *Pacific Sapphire* of the Maynord (2003) report. Maynord's study was conducted to analyze before and after deepening ship-wave effects on two locations (termed south and north sites) in the SNWW, Port Arthur, TX. The work of Maynord (2003) was conducted for USACE SWG. The field work was carried out during April–May 2002 by ERDC personnel. The field data collection was supplemented by numerical modeling of ship-wave effect using HIVEL2D (Stockstill and Berger 1994).

Since both the actual bathymetry/topography terrain data and true vessel path (AIS does not go so far in time) were not available, it was necessary to resort to a sample path of a closest-type vessel in dimensions and velocity from the previous section (AIS paths corresponding to vessels from the time frame of Zaloom et al. (2017) work) as well as bathymetry/topography maps from that time frame. Figure 34 presents the two sites, henceforth referred to as South Site and North Site, where different instruments like the pressure and capacitance gauges were deployed. For additional details on gauge parameters and recorded vessel traffic, see Maynord (2003).

Figure 33. Effects of vessel parameters for NS *Champion* using pressure source TYPE I, Equation (1), on wave height (left column, blue curve) and period (left column, orange curve) of the drawdown wave, and L_2 norm, computed with Equation (30), on the main drawdown wave subdomain of the field data (right column, red curve) and the relative percentage difference of the drawdown wave only (right column, green curve). Period and wave height of the drawn down wave computed from field data are given by the horizontal dashed lines (left column), and the default vessel parameters are denoted by the vertical dashed black lines.

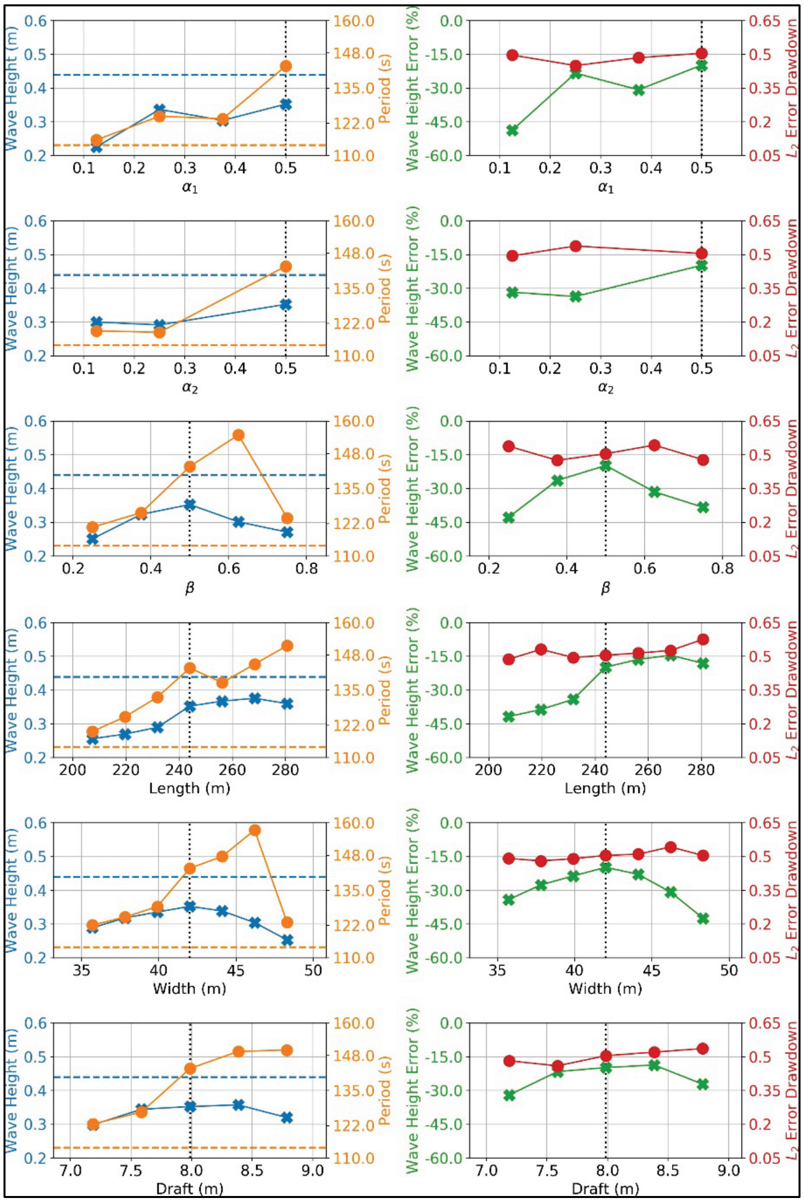

Figure 34. Schematic of the SNWW channel outlining two data collection sites (south and north) in Maynord (2003).

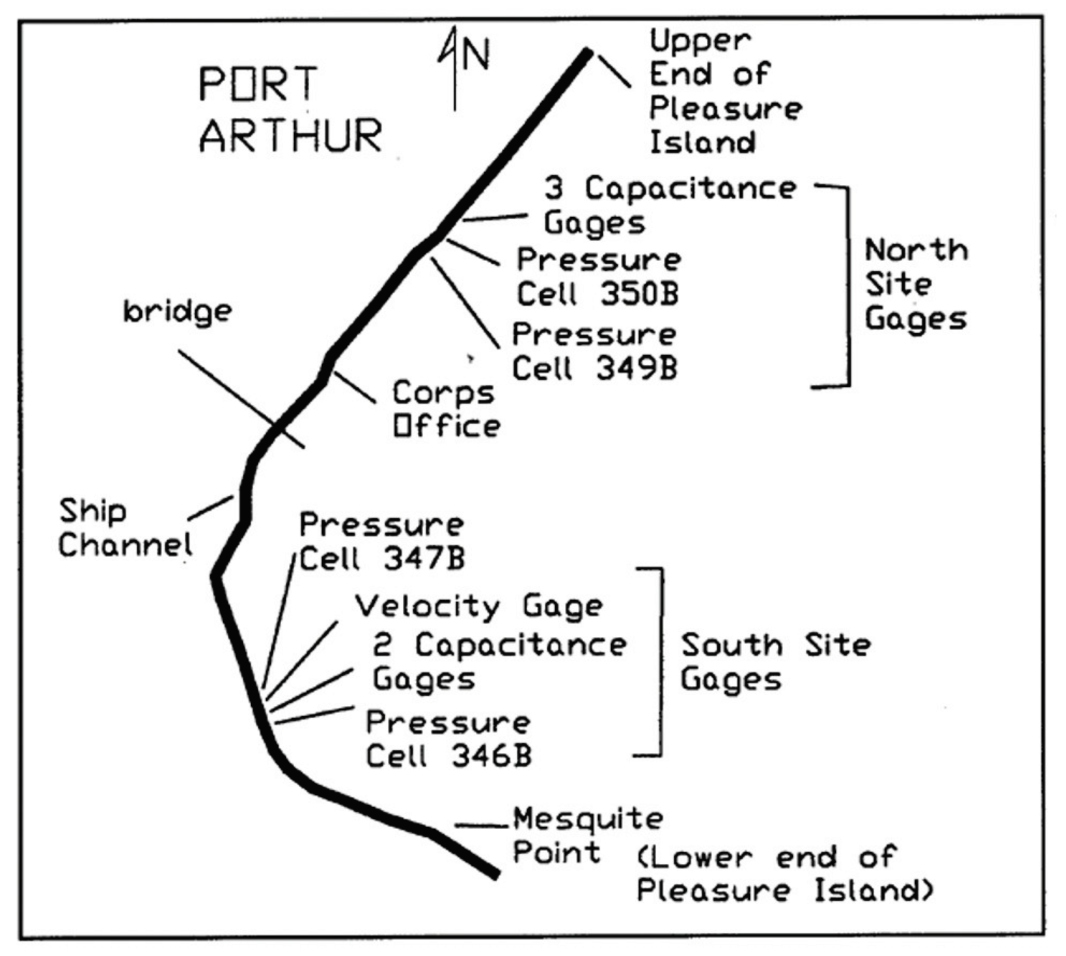

The vessel used for the numerical comparisons was the *Pacific Sapphire* (tanker) during the 1 May 2002 (inbound) and 4 May 2002 (outbound) passages. During the inbound 1 May passage, the *Pacific Sapphire* reported having the length of 247 m, width (beam) of 41.7 m, and the loaded draft of 12.2 m. The inbound passage occurred during the tidal slack (zero tidal current) with water level of 0.96 m (Mean Low Tide [MLT]). All simulations were performed using the NAVD88 datum; hence, conversions of elevation and water levels were needed (MLT [meters] = NAVD88 [meters]+ 0.268 m). For the outbound passage on 4 May, the unloaded vessel reported a draft of 8.5 m, also during tidal slack with water level of 0.58 m.

Figure 35 shows an elevation map for the North Site from the Maynord (2003) report (left) and the FUNWAVE grid that was used (right). The purple dots on the right image represent location of numerical (FUNWAVE) stations. For illustration purposes, the FUNWAVE image (right) was converted to the MLT datum and shown in feet to better compare to the image from Maynord (2003) plot (left). It was only possible to obtain and confirm an approximate field gauge location, and as such, had to resort to putting down a line of computational gauges from the middle of the channel towards the river bank (every 20 m) to find the closest match. Moreover, the footprint of the channel has changed some, and it was desired to compare the results at least from a gauge that matched the reported depth from Maynord (2003). This would also allow an analysis of the nonlinear effects of shoaling and wave breaking with distance to the riverbank. It is expected that FUNWAVE resolves the deformation of the free-surface during nearshore shoaling and wave breaking well, which is the most important process in wave-sediment interaction.

Figure 35. Bathymetry contours at the North Site from the Maynord (2003) report (left) and the actual bathymetry/topography profile used in FUNWAVE simulations (right). For illustration purposes, the FUNWAVE image (right) was converted to the MLT datum and shown in feet to better compare to the image from Maynord (2003) plot (left).

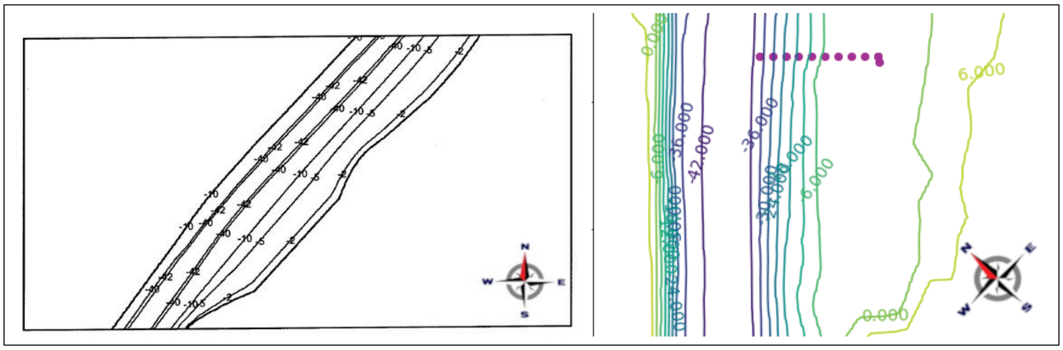

In Figure 36, a comparison between digitized image of the TSW height in feet of the outbound passage of the *Pacific Sapphire* on 4 May at the North Site. As can be seen, the drawdown part of the TSW is very well resolved with FUNWAVE Pressure Source TYPE I mechanism, even for varying hull curvature parameters (α_1, α_2, β), where the base case represents all those parameters equal to 0.5. When analyzing the surge part of the TSW, it is easily seen that FUNWAVE tends to break and dissipate wave energy of the steep surge wave here, thus showing different overall vertical extent of the TSW. Note that all of the numerical and physical grid parameters utilized in validation contained in the previous section (Zaloom et al. 2017) were copied over to this validation. See Appendix A for a full list of common parameters.

In contrast, Figure 37 shows the loaded inbound Pacific Sapphire vessel passage, but at the South Site location. Here, the vertical axis representing the free-surface elevation is shown in feet, and the horizontal axis is time in seconds. Since this field data image (Maynord blue curve) was also digitized from their report, the plot was offset to match their mean water level (0.96 m). Contrary to the Figure 36, the surge part of the TSW is much better resolved due to less wave breaking caused by a milder slope in the wave. Note also that for larger values of α1 and β, resulting in a block coefficient $C_B = 0.76$, the vertical extent of the overall TSW has a better match to the field data and is also representative of larger vessels (Figure 24).

Figure 36. North Site outbound passage comparison of the time series for the *Pacific Sapphire* tanker collected field data from Maynord (2003) (blue) versus FUNWAVE simulations (orange, green, red). The base case represents all of hull curvature parameters (*α*1, *α*2, *β*) equal to 0.5. The horizontal axis is in seconds (time), and the vertical axis is in feet (free-surface elevation).

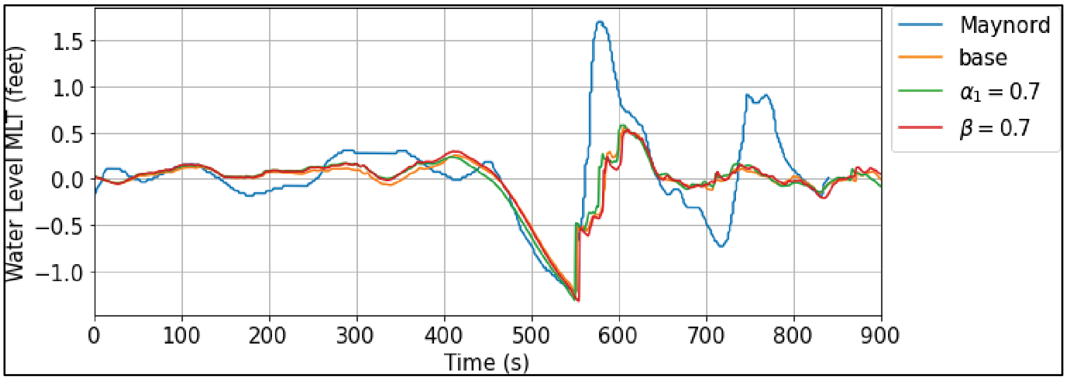

Figure 37. South Site inbound passage comparison of the time series for the *Pacific Sapphire* tanker collected field data from Maynord (2003) (blue) versus FUNWAVE simulations (orange, green). The base case represents all of hull curvature parameters (*α*1, *α*2, *β*) equal to 0.5. The horizontal axis is in seconds (time), and the vertical axis is in feet (free-surface elevation).

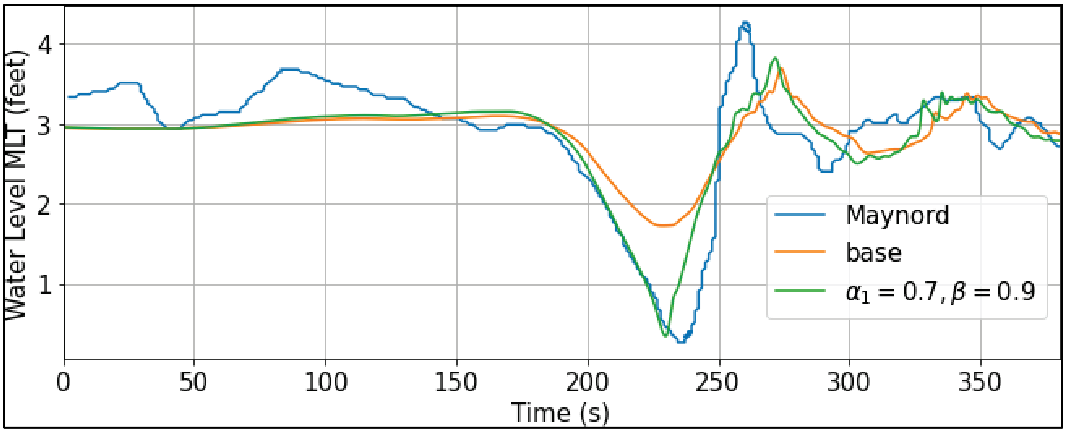

To summarize, the authors carried out validation work against a limited data, or rather a tabulated values of bulk parameters and digitized images of the recorded output. In both comparisons, Zaloom et al. (2017) and Maynord (2003), the FUNWAVE model behaved favorably, especially for the drawdown part of the ship-wave system. Based on the Bernoulli equation, the drawdown should be dependent on the blocking ratio/coefficient (C_B and C_M). Since the surge part of the TSW is often in a shape of a turbulent bore with a spilling breaker, the model tended to break and dissipate that energy quickly, hence, leading to underestimation of the surge wave part of the TSW.

Going forward, however, there is operational confidence in FUNWAVE’s ability to model large container-type vessels in complex 2D navigational channels of sufficient widths. The Pressure Source TYPE I and II mechanisms are believed to be robust in the far-field distance from the vessel (distance greater than a length of the vessel), as the individual features of the vessel hull do not play a crucial role in the far field. To model properly the near-field effects, one may need to resort to a higher-fidelity model, like a full computational fluid dynamics (CFD) simulation that allows for multi-value solutions and can model plunging and spilling breakers using first principles. Unfortunately, the full CFD simulations require inordinate amount of time and computational resources to deliver results on larger grids. Thus, FUNWAVE is still an outstanding candidate for quantification of ship-wave effects on complex 2D adjacent shorelines in an operationally quick setting.

4 Erosion Hot Spot Analysis in SNWW

To perform an analysis of hot spots with a reasonable number of computations in SNWW simulations, the number of vessels obtained through AISAP were filtered down. This was done in part due to a large computational burden (several hundred thousand computational HPC hours were utilized across the entire study on DoD HPC systems) as well as to pick out vessels and vessel paths with most certainty and correlation with the true sample. This would help in extrapolating to a larger (true) sample size of vessel traffic in SNWW. Hence, one would be able to better quantify the cumulative effects of the vessel-generated waves and their erosion/scour effects.

4.1 Filtering AISAP data

In the 7 weeks of data collected from AISAP, 3 weeks in May 2016 and 4 weeks in January–February 2017, over 2,300 vessels were found to be in at least one of the AOIs shown in Figure 12. This 7-week sample size is statistically significant when compared to the true annual vessel traffic (not shown here). However, not all the vessels reported all of their dimensions (length, width, and draft); hence, vessels that do not report all their dimensions were filtered out. This reduced the total number of vessels to 1766 (approximately a quarter of vessels did not fully report their dimensions). To further reduce that number of vessels, it was required that there are at least 400 data points in a single AOI ensuring that there is sufficient data to interpolate a smooth and accurate vessel path for simulations. From the 1,766 vessels, 1,723 vessels had sufficient data points indicating vessel AIS frequently updates their positions, which is expected given that this is required in high traffic area such as SNWW. Last, to further reduce the number of vessels, simulations to vessels that travel all AOIs in a single transit were restricted, reducing the amount of vessels to 48. See Table 1 for details of the filtering stages for each time interval.

Figure 38 presents a histogram of vessel dimensions after the first two filter steps. The statistical data indicate that approximately 60% of vessels are small vessels with lengths less than 30 m, beam/width of less than 20 m and draft approximately 2.5 m. The remaining vessels are large vessels with lengths over 100 m, with average widths of 35 m and average drafts of 9 m. Figure 39 shows the average speed of transits in each AOI. Note that vessels may have more than one transit. Statistical data also indicate that there is a range of vessel speeds in different AOIs, with the majority of vessels traveling under 10 kn. As one can see though, there are vessels present in the sample size that do travel at 20 and even 30 kn, albeit only few of them. In that figure, a logarithmic scale was utilized to show in greater detail the vessels in high-velocity sample AOIs. Furthermore, there is a dense amount of traffic in the Gauge 1 AOI, which is expected due to the main Port Arthur dock being in the region.

Table 1. Number of vessels initially collected from AISAP and after each filtering step for each time interval: (1) 4 April 2016 to 11 April 2016; (2) 12 April 2016 to 26 April 2016; (3) 11 January 2017 to 25 January 2017; (4) 30 January 2017 to 15 February 2017, and the total over all the time intervals.

818353	Time Interval				
Number of vessels	(1)	(2)	(3)	(4)	Total
Initial AISAP data	417	659	595	668	2339
With parameters	311	469	471	515	1766
With minimum data points	297	459	464	503	1723
In all five AOIs	10	6	12	20	48

Figure 38. Distribution of vessel dimensions collected from AISAP after filtering vessels with reported length, width, and draft, and filtering vessels with minimum amount of data points. Vertical dashed red line indicates the mean value.

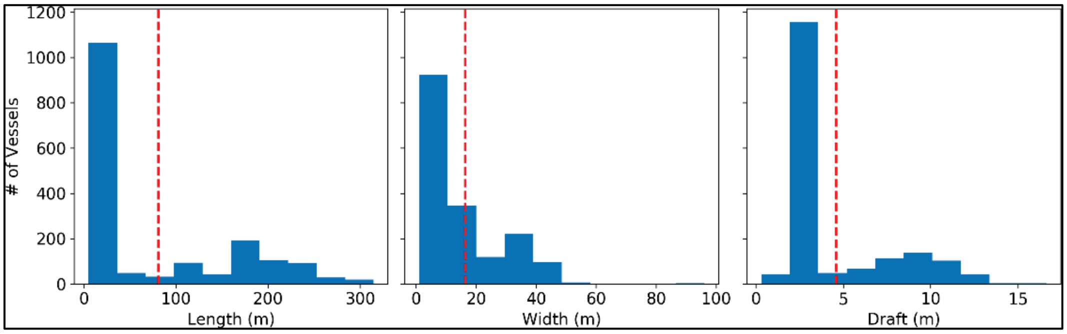

In Figures 40 and 41, the same statistical data are shown as Figures 38 and 39 for the actual simulations that were performed. These plots show that final filtering step led to simulations that covered an appropriate range of vessel shapes and speeds but focused on larger vessels. Note that the filtering steps indicated that larger vessels are more likely to travel between all AOIs than the smaller ones in a single transit. However, note that vessel transit is generally driven by load/discharge ports and the route between the two. Thus, relative care should be taken when assigning a statistical meaning to this observation.

Figure 39. Distribution of vessel speeds in each AOI collected from AISAP after filtering vessels with reported length, width, and draft, and filtering vessels with minimum amount of data points. Vertical dashed red line indicates the mean value. Note that a logarithmic scale was used to show the details for the few outliers traveling above 10 kn.

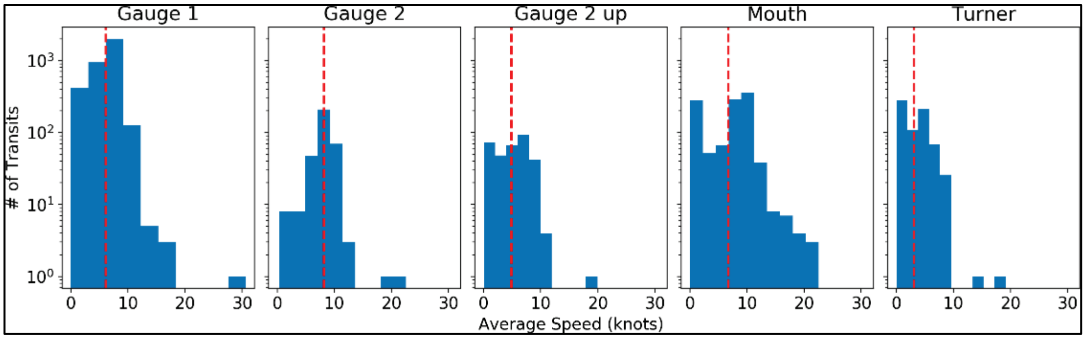

Figure 40. Distribution of vessel dimensions used for simulations. Vertical dashed red line indicates the mean value.

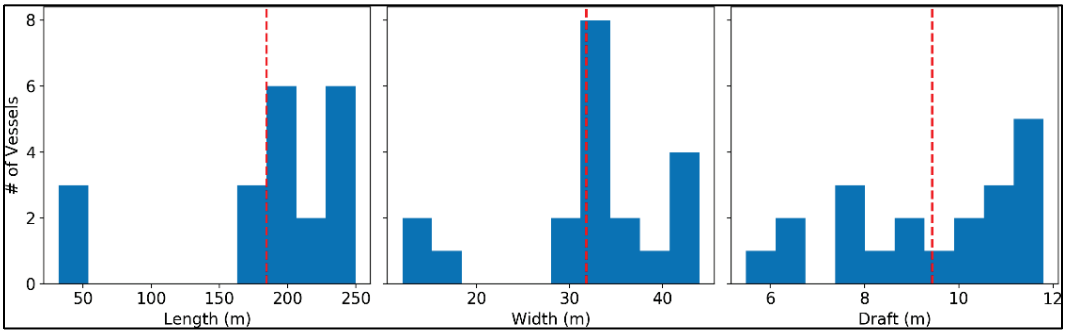

Figure 41. Distribution of vessel speeds in each AOI used for simulations. Vertical dashed red line indicates the mean value.

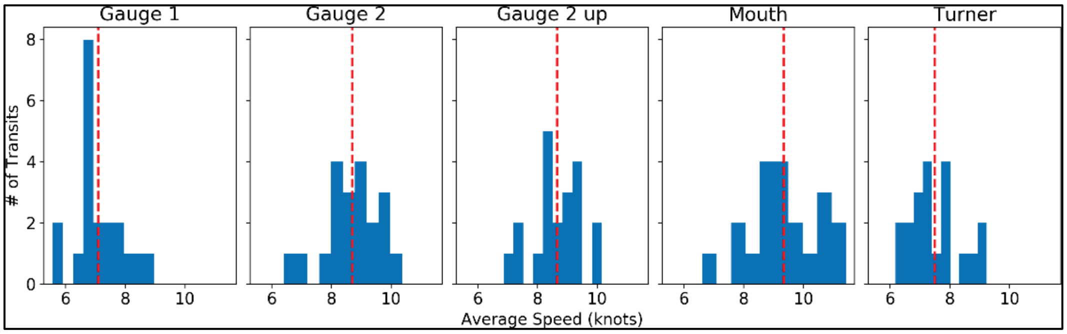

4.2 Simulation stability

Before discussing ship-wake induced erosion results from FUNWAVE-TVD simulations, note that there were difficulties in stabilizing simulations. Out of the 49 vessels for five different locations resulting in a total of 245 simulations attempted, 123 were fully successful. In addition, few simulations led to erosion outliers, with greater than 10 cm of depth change and therefore were ignored for this analysis, resulting in 115 simulations (see Table 2 for more details). Figures 42 and 43 present a histogram of vessels' dimensions and average speed in each AOI, respectively. Note that successful simulation results still cover a wide range of vessel sizes and speeds.

Table 2. Number of vessels in each AOI with successful simulations before and after the erosion-outliers (more than 10 cm) filtering process.

AOI	Successful	Filtered
Gauge 1	24	22
Gauge 2	24	24
Gauge 2 up	25	23
Mouth	25	22
Turner	25	24
Total	123	115

Figure 42. Distribution of vessel parameters for successful simulations. Vertical dashed red line indicates the mean value.

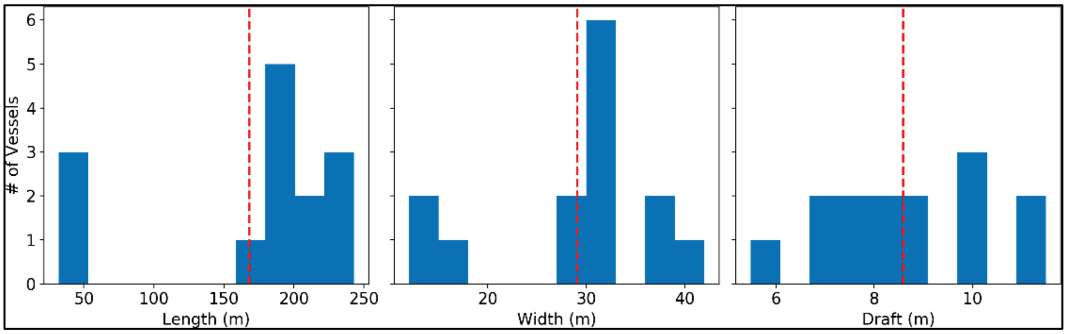

Note that instability issues in simulations are primarily because of the low under-keel clearance (UKC), hence the decrease in the value of the mean draft and the subsequently fewer vessels with drafts greater than 10 m for successful simulations in Figures 40 and 42. The pressure source mechanism has been widely used for ship wake generation in Boussinesq-type wave models (e.g., Nwogu [2001], David et al. [2017], Shi et al. [2018] and Shallow Water Equation-based models, e.g., Stockstill and Berger [1999]).

Figure 43. Distribution of vessel speeds in each AOI for successful simulations. Vertical dashed red line indicates the mean value.

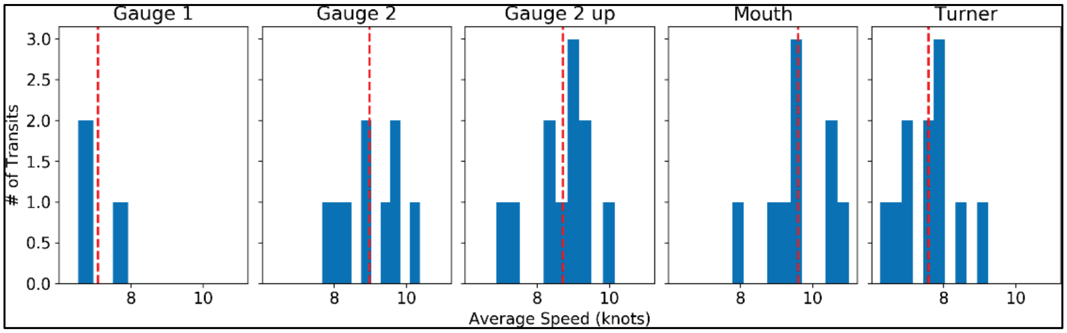

To alleviate this pressure-source issue, several studies (e.g.,Maynord [2003] or Stockstill and Berger [1994]) have purposely reduced the draft and correspondingly increased the beam (width) of the vessel such that the mid- ship cross-sectional area coefficient (C_M) of the vessel remained constant (i.e., after simplification in C_M) yielding

$$W_{\text{original}} D_{\text{original}} = W_{\text{new}} D_{\text{new}} \tag{31}$$

where *W* and *D* are the beam and draft of the vessel, respectively. However, it is believed that rigorous analysis of this approach has not been performed.

Figure 44 plots the ship wake signal for the *Pacific Sapphire* tanker with various adjustments to vessel's beam with corresponding modification to the draft such that the C_M remains the same. The results show that the ship-wake signals are nearly identical across the various beams and drafts considered, even in the most extreme case where the width is slightly more than doubled and the draft halved. Note that increasing the draft (by decreasing the beam) causes the depth of the draw-down wake to decrease. It is unclear if this observation is a consequence of the instability from the low UKC or a result of some other numerical artifact.

Nonetheless, further investigation is needed into this approach, as well as potential changes to the observed erosion patterns. However, such a research effort is not currently within the scope of this report. For all of the simulations, the prescribed width and draft of a vessel have not been altered; thus, only those simulations that remained stable throughout the entire simulation were analyzed.

4.3 Erosion analysis

To analyze the erosion in each AOI, two quantities were computed. Mainly, the average and maximum erosion were compared, defined as the vertical bed (depth) change at each grid point; specifically, the mean and maximum were computed as follows:

$$\bar{d}_{(i,j)} = \frac{\sum_{p=1}^{P} d_{(i,j),p}}{P} \tag{32}$$

and

$$\hat{d}_{(i,j)} = \max_{1 \le p \le P} d_{(i,j),p} \tag{33}$$

respectively, where the (i, j) subscripts denote the grid point and the p subscript enumerates the P number of total simulations under consideration. In addition to the combined directional traffic, erosion effects of inbound and outbound traffic were considered separately, as well.

Figure 44. FUNWAVE simulation ship wake results of Pacific Sapphire tanker with various adjustments to vessel's beam with corresponding modification to the draft such that the cross-sectional area remains the same, see Equation (31).

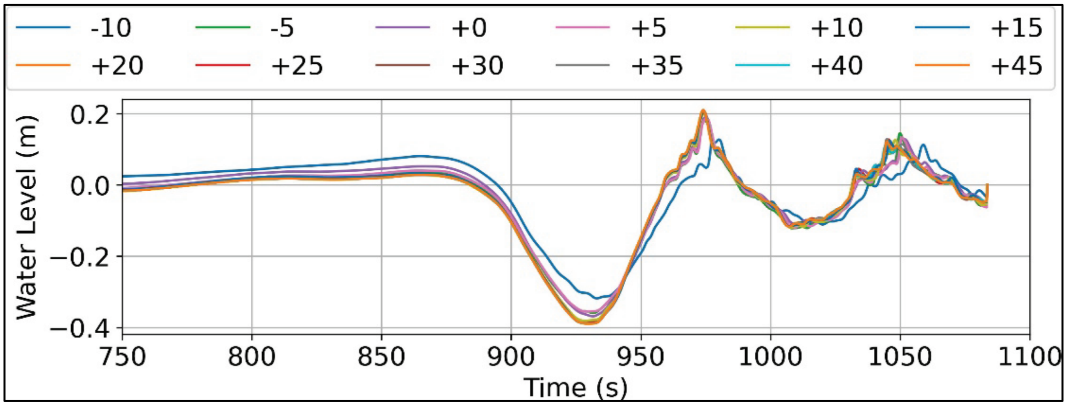

4.3.1 Updating the bathymetry after each vessel vs. using same initial bathymetry

Before investigating erosion and scour effects in the SNWW, the methodology of using the same initial bathymetry across all simulations was justified, instead of updating the bathymetry after each vessel passage. In Figure 45, the total cumulative erosion is plotted for nine vessel passages in the Gauge 2 location for (a) the same initial bathymetry for each vessel and (b) updating the bathymetry after each vessel passage. Simulation results demonstrate that there is little difference between the two cases. Note that in the case of updating the bathymetry, there is a negligible amount of mass loss due to suspended sediment in the water column that has not had the time to resettle, in particular at the end of the vessel path.

Safty and Marsooli (2020) performed similar vessel-wake simulations with FUNWAVE in the Jamaica Bay, New York, and reported that out of 10 repeated passages of a large vessel, the total cumulative erosion for the last 5 passages was 2–3 times greater than the first 5 passages. This will, of course, depend on the time interval between each vessel passage and the generated flow conditions, as sediment transport is intimately related to it. In this study, there was not an observation of increased amounts of erosion from the first five runs versus the second five vessel passages—they were comparable. This result does not necessarily contradict the authors’ result, as in that work the erosion was measured using a change in depth at a specific grid point, whereas the authors’ result computes the total erosion over the entire domain.

Results in the subsequent subsections also suggest that large erosion events are more likely due to the specific dimensions of a vessel and its path, rather than a cumulative effect of multiple vessel passages.

Figure 45. Comparison between total accumulated erosion over the entire Gauge 2 location (left) and average accumulated erosion over the entire Gauge 2 erosion per vessel (right) when using the same initial bathymetry for each vessel (dashed blue curve) and updating the bathymetry after each vessel run (solid red curve).

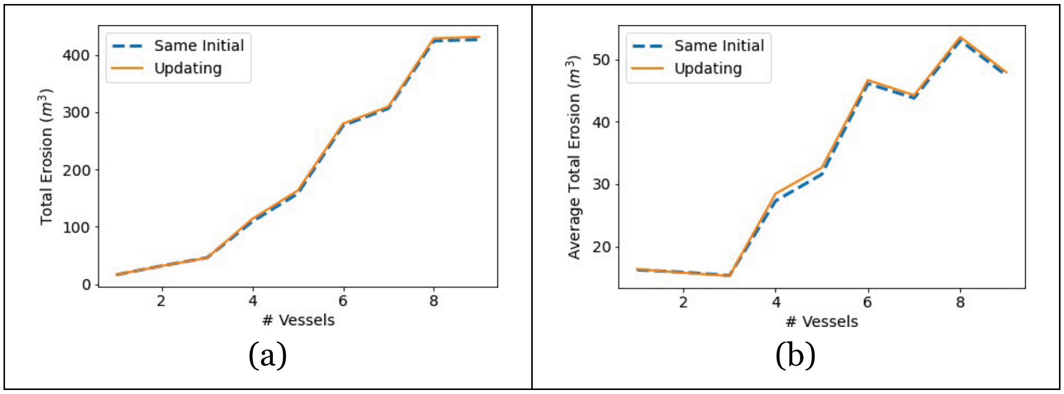

(a) (b)

4.3.2 Individual grid – the Mouth

Having justified the approach of not updating the bathymetry after each vessel passage, the analysis with traffic entering the SNWW from the Mouth AOI and moving to locations more inland was begun. In Figure 46, the erosion in the Mouth AOI is shown. Note that comparing the erosion patterns for mean values and the maximum values, there is little difference between the locations where erosion occurs; however, the maximum values are larger. This indicates that while ship-wake induced erosion patterns are qualitatively the same for different vessels, the degree of erosion within this pattern varies between each vessel. Also note that there is substantial erosion along the water center line of the channel, which coincides with the path of the vessels. The extent of the inner-channel erosion caused by the vessel passage needs further investigation as some of these appears to be due to low UKC between the bottom of the vessel and the channel floor, resulting in pressure fluctuations below the vessel. Also note that each run was a separate event and there was no sediment resuspension happening prior to vessel passage.

In terms of erosion hot spots within this sub region, there appears to be one, marked with a blue pin in the final image (c) showing maximum erosion. Note that the plots in (c) have a split color bar, where yellow indicated a threshold for erosion areas. For the mean erosion plot in (c), the threshold is 0.05 cm whereas for the maximum erosion, the threshold is an order of magnitude higher and equal to 0.5 cm. The same threshold will be applied to all subsequent subgrids. As far as the authors are concerned, they have never seen any classification of vessel-induced erosion from numerical simulations in literature. The results only provide erosion patterns. One could use a morphological factor to get a quantity. However, an erosion spot would eventually get to an equilibrium. For Figure 46, the single hot spot coincides with a cove centered at approximately $y = 2500$, $x = 2400$, as seen in more detail on satellite images in Figure 47, where the hot spot longitude and latitude coordinate is given by (29.767475, -93.883590).

Satellite images with outlined hot spots (blue pin) are shown in Figure 47, along with the corresponding latitude and longitude coordinates. Comparing the difference of erosion induced by inbound and outbound traffic, it appears that inbound traffic, subpanel (a), induces less erosion. also note that outbound traffic, subpanel (b), induces more erosion at the tips of the jetties of the channel entrance at $y = 14000$. These effects are likely attributed to the orientation of the vessel-generated divergent waves, as well as typical shoreline geometry (angle of trapping regions), with increased vortical eddies created around the inlets/jetties in that case. In general, the corresponding inbound and outbound traffic differentiates between loaded and unloaded vessel draft (e.g., ballast draft) and that would ultimately induce different vessel wave heights. However, it was noticed that vessel drafts reported in AIS often remained unchanged between their respective inbound and outbound tracks. It is unclear if this is due to incorrect information being reported to AIS, or if the vessel is being unloaded and then reloaded before returning on the outbound traffic. More detailed and reliable investigation of load/draft conditions would be recommended. Without such verified information, it would be difficult to provide additional draft (vessel load) conclusions with enough certainty.

Also note that the simulations were done without ambient forcing (wind generated waves or tidal currents), and the water surface was modulated exclusively by vessel-generated waves. Both these effects can be added into the model; however, the latter (tidal currents) would require one-way manual grid coupling at a boundary to impose time-dependent currents. For the SNWW, the tidal range is approximately 0.45 m, and the tidal current is not significant (Maynord 2003). In general, tidal currents may be significant and be on the order of 2 m/sec, especially near inlets, thus contributing to wave-generated erosional effects through basic wave transformation and wave-current interaction.

4.3.3 Individual grid – Gauge 2

Switching focus to Gauge 2, where the Golden Pass in located, Figure 48 shows similar erosion along the vessel path, as in the previous sub- section (Mouth). However, the magnitude of the erosion is larger and may be a result of the shallower channel depth. Depths here range from 12 to 13 m versus 16 to 17 m in the Mouth, resulting in higher pressures below the vessel. This further supports the claim that the erosion in the main channel is due to low clearance between the bottom of the vessel and the channel flow (UKC). While the erosion/deposition effects in the main part of the channel are not the focus of this work/report, note that sudden or appreciable vessel velocity changes may also contribute to main channel erosion/deposition effect and should be further investigated.

In addition, there appears to be more erosion along the banks when compared to the Mouth location, the mean erosion where the channel width decreases, $5000 < y < 6000$, for inbound traffic (moving from right to left) in top of sub-panel (a). Given that the same degree of erosion is not observed for outbound traffic in the top of sub-panel (b), it suggests that the increased erosion may be due to waves being funneled from the larger body of water into the channel. Following the turn between $y = 500$ and $y = 2000$, there appears to be more erosion along the bank on the outside of the turn in contrast to the inside of the turn, indicating that the path of the vessel (turning) may be increasing the energy of the ship-wakes, thus enhancing erosion.

Finally, there appear to be three erosion hot spots in this region. One approximately centered around $y = 1200$, $x = 125$ with longitude/latitude coordinate of (29.774171, -93.943214); a second one centered around $y = 4200$, $x = 600$ with its longitude/latitude coordinate of (29.764485, -93.909154); and the third around $y = 5500$, $x = 700$ with longitude/latitude coordinate of (29.760297, -93.902455). A satellite image of those three hot spots is shown in Figure 49, along with their respective longitude and latitude coordinate. The left-most hot spot corresponds to a channel connecting to the Keith Lake, which may trap waves and cause prolonged reflection/ringing. For the middle hot spot, the erosion is stronger for outbound traffic (moving from left to right) in sub-panel (b) than for inbound traffic, sub-panel (a), indicating ship-wakes traveling into the outcrop perpendicular to the vessel path are reflected and are causing increased erosion. For the right-most hot spot, significant erosion occurs on the bank, which may be the result of the funneling of vessel-generated waves into a thinner channel and may likely need to be investigated further. Nonetheless, intricate channel and adjacent bank geometry, which is unique and specific to every area, is one of the main contributing factors to increased erosion, and it further justifies the point about the need for 2D (not one-dimensional cross-sectional) vessel-wave numerical modeling.

Figure 46. Mean and maximum erosion in the Mouth subgrid location for (a) inbound traffic (moving here from right to left), (b) outbound traffic (moving here from right to left), and (c) overall traffic. The erosion hot spots are marked with a blue pin in the final bottom image in (c) for maximum erosion. Plots in (c) have a split color bar, where yellow indicated a threshold for erosion areas. For the mean plot in (c), the threshold is 0.05 cm whereas for the maximum plot the threshold is 0.5 cm.

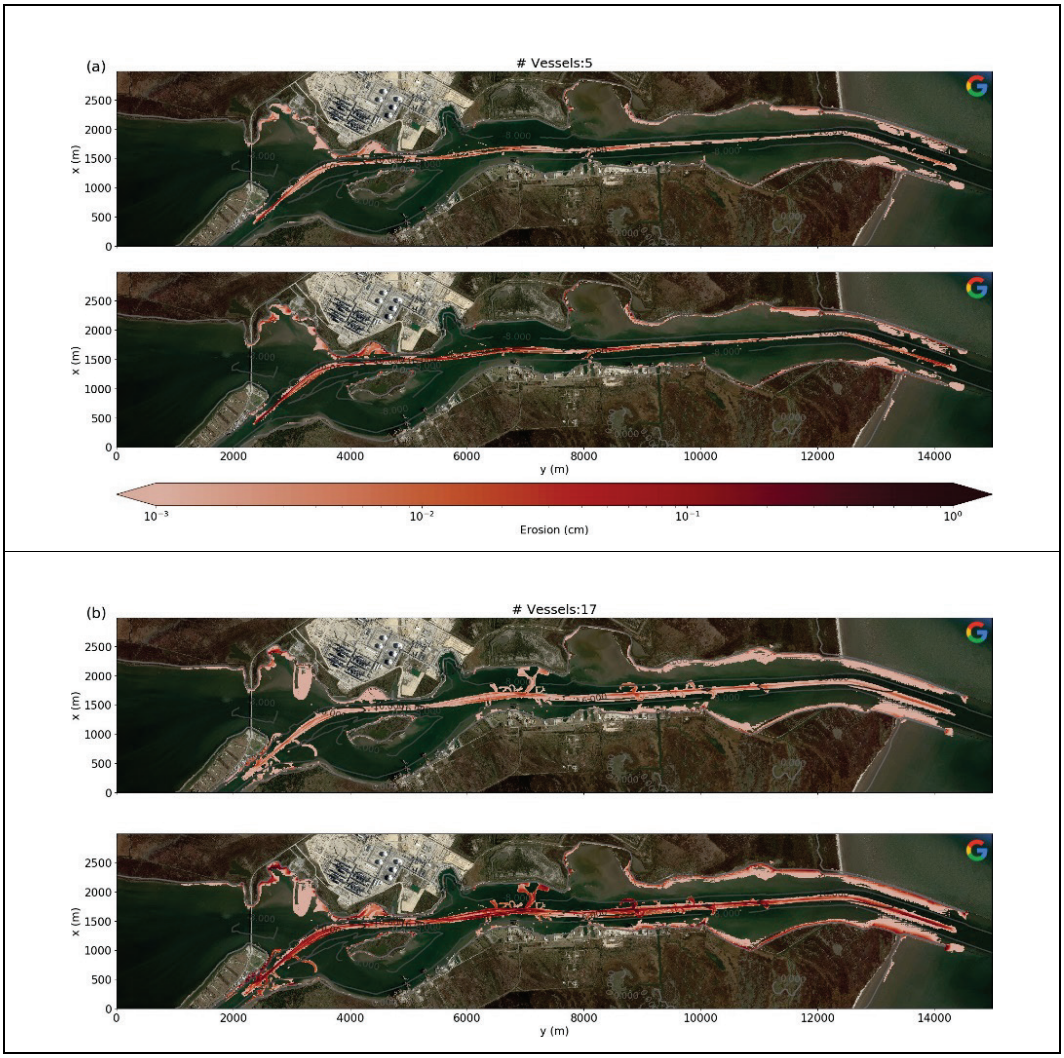

Figure 46. (cont.)

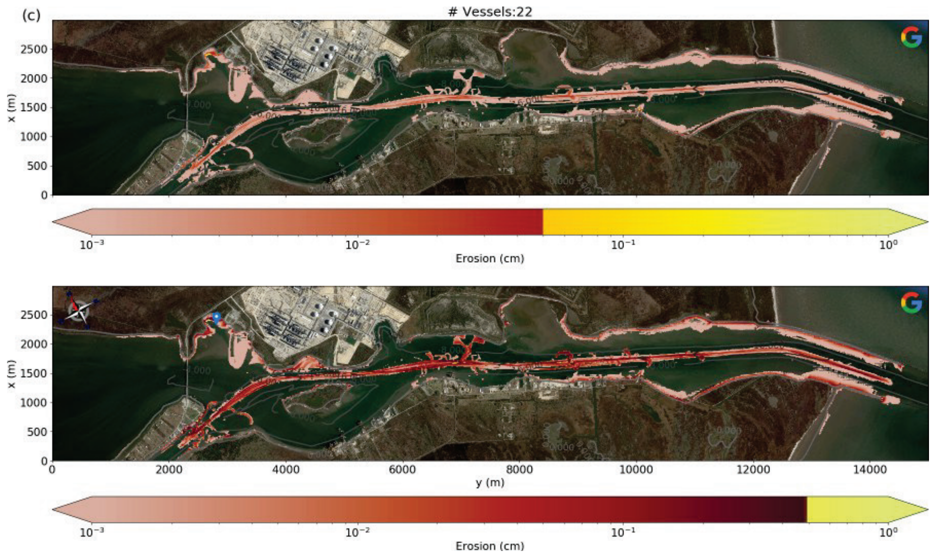

Figure 47. Satellite images of hot spot region in Figure 46 where the pin corresponds to longitude and latitude coordinates (29.767475, -93.883590).

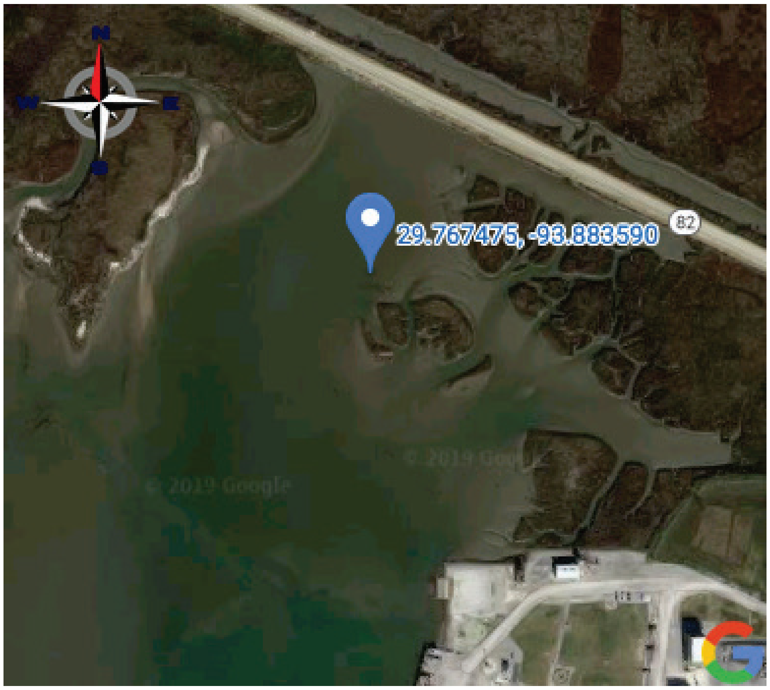

4.3.4 Individual grid – Gauge 2 up

In Figure 50, erosion results are shown for the Gauge 2 Up location. Note that due to the large aspect ratio of the domain, the *y*-axis of the plot is stretched. For the inbound traffic (moving from left to right) in sub-panel (a), features that are similar to other locations are observed. However, for the outbound traffic, sub-panel (b), there is significantly more erosion. It is unclear what leads to the increased erosion. It may be due to a funneling effect similar to Gauge 2 or some sheltering, or the turning of the vessel that may be increasing the energy of the shipwake (note the increased erosion on the bank on the outside of the turn between y = 4750 and y = 5500, between longitude/latitude coordinates (29.817688, -93.960459) and (29.822276, -93.962517)). These waves may, in turn, be reflected farther down the channel or a combination of the two. Heavy erosion in this area was also mentioned in Zaloom et al. (2017). Therefore, the numerical results are reasonable and in agreement with the findings of Zaloom et al. (2017). In Figure 51, a hot spot region where significant erosion occurs on the bank is shown, along with its corresponding longitude and latitude coordinate of (29.801437, -93.954770).

Figure 48. Mean and maximum erosion in Gauge 2 location for (a) inbound traffic (right to left), (b) outbound traffic (right to left), and (c) overall traffic.

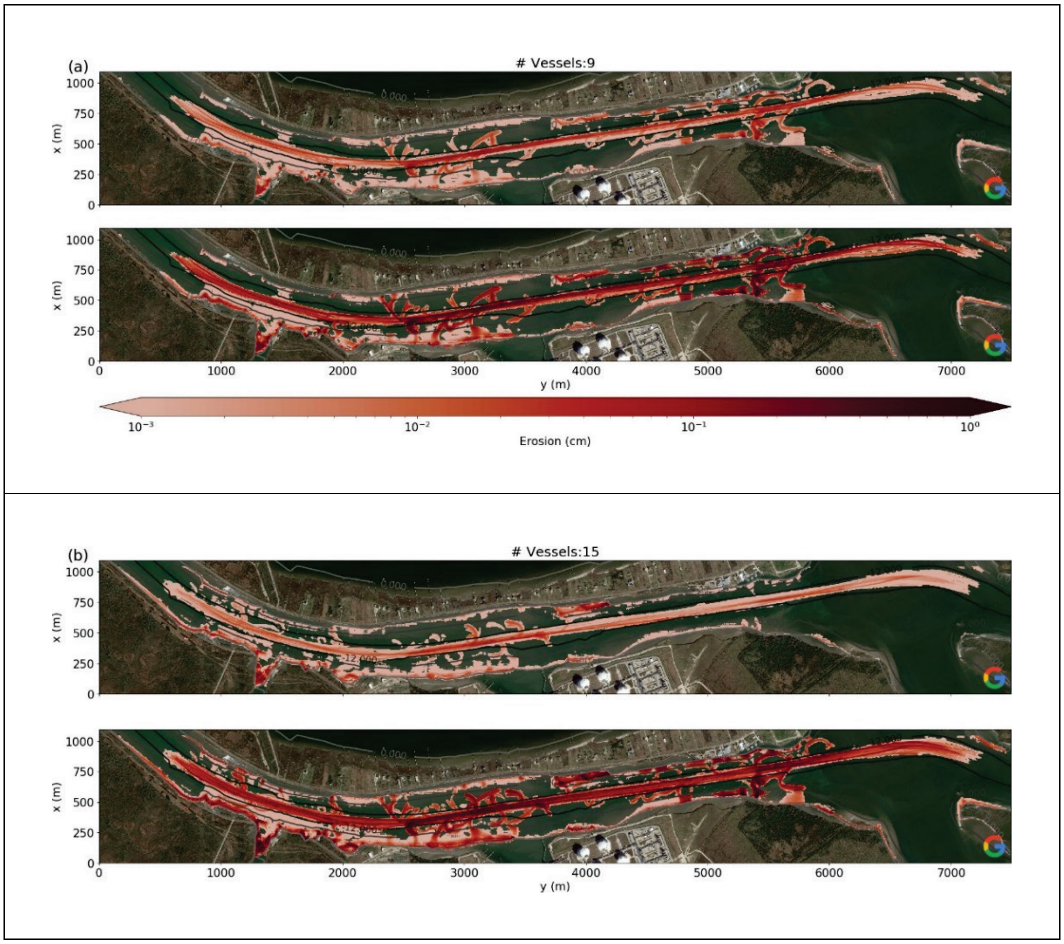

Figure 48. (cont.)

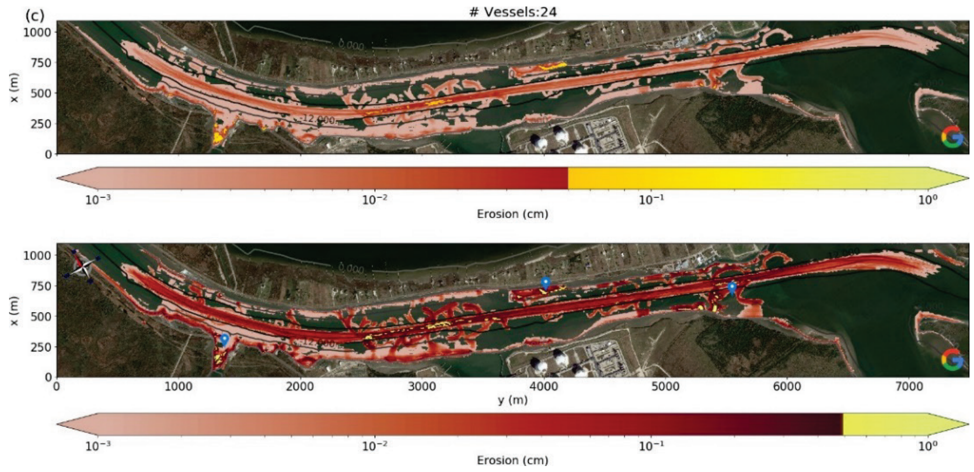

Figure 49. Satellite image of the hot spot regions in Figure 48 where the pins correspond to longitude and latitude coordinates (29.774171, -93.943214), (29.764485, -93.909154), and (29.760297, -93.902455), respectively.

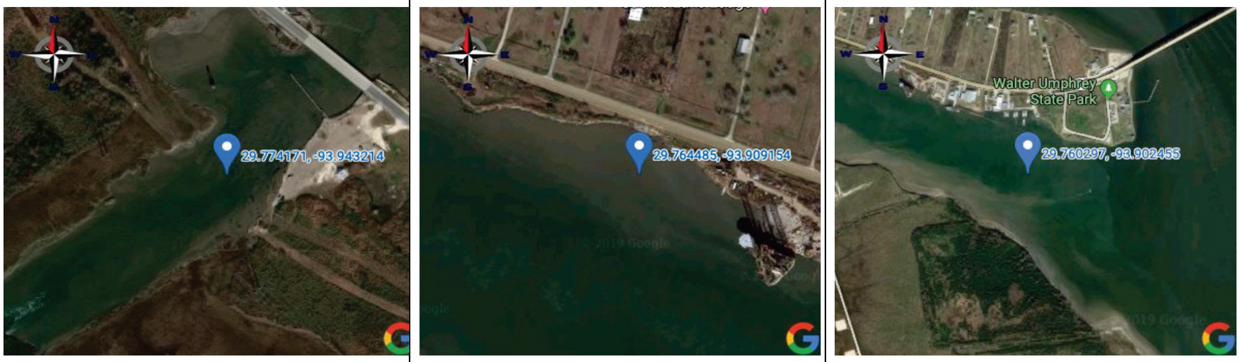

(a) (b) (c)

4.3.5 Individual grid – Turner

Moving farther inland to the Turner location in Figure 52, similar features as in previous grid analysis are identified. However, unlike previous results, there does not appear to be a significant difference between the erosion on the outside and inside banks of the turn between y = 2500 and y = 3600, where in the previous grids the outside of the turn bank had substantially more erosion, as opposed to the inside of the channel. This difference is likely due to a smaller curvature of the turn and the slower vessel speeds in the location, 7.5 kn here in Turner vs. 9 kn in Gauge 2 and

Gauge 2 Up (Figure 43). Two erosion hot spots were identified. These are centered at $y = 600$, $x = 200$ and $y = 3600$, $x = 500$, with longitude and latitude coordinates of (29.823112, -93.954583) and (29.852255, -93.943162), respectively. The satellite images and coordinates are shown in Figure 53.

Similar to previous results, these hot spots occur in small coves where waves are generally trapped and can reflect (ring) multiple times.

4.3.6 Individual grid – Gauge 1

The last region to discuss is Gauge 1, where Port Arthur is located. The erosion result plots are shown in Figure 54. Note that due to the large aspect ratio of the domain, the horizontal y-axis of the plots is stretched. There are three hot spots identified here centered at $y = 6250$, $x = 300$; $y = 8250$, $x = 175$; and $y = 11750$, $x = 250$; with longitude and latitude coordinate of (29.888246, -93.910852), (29.902370, -93.895891), and (29.928291, -93.873383), respectively. Those coordinates are also shown on satellite images in Figure 55. Similar to previous results, the left-most hot spot is a cove-like area, and the right-most hot spot corresponds to channels between two barrier islands. This was also another hot spot region identified in the report of Zaloom et al. (2017). Note, however, that the bathymetry data are older than the satellite image as there are two barrier islands in the data as opposed to one in the satellite image. The middle hot spot is similar to the left-most hot spot discussed in Gauge 2 (Figure 48), with higher erosion identified for outbound traffic, sub-panel (b), where vessels are heading towards the outcrop region.

Figure 50. Mean and maximum erosion in Gauge 2 Up location for (a) inbound traffic (left to right), (b) outbound traffic (right to left), and (c) overall traffic. Note that due to the large aspect ratio of the domain, the y-axis of the plots is stretched.

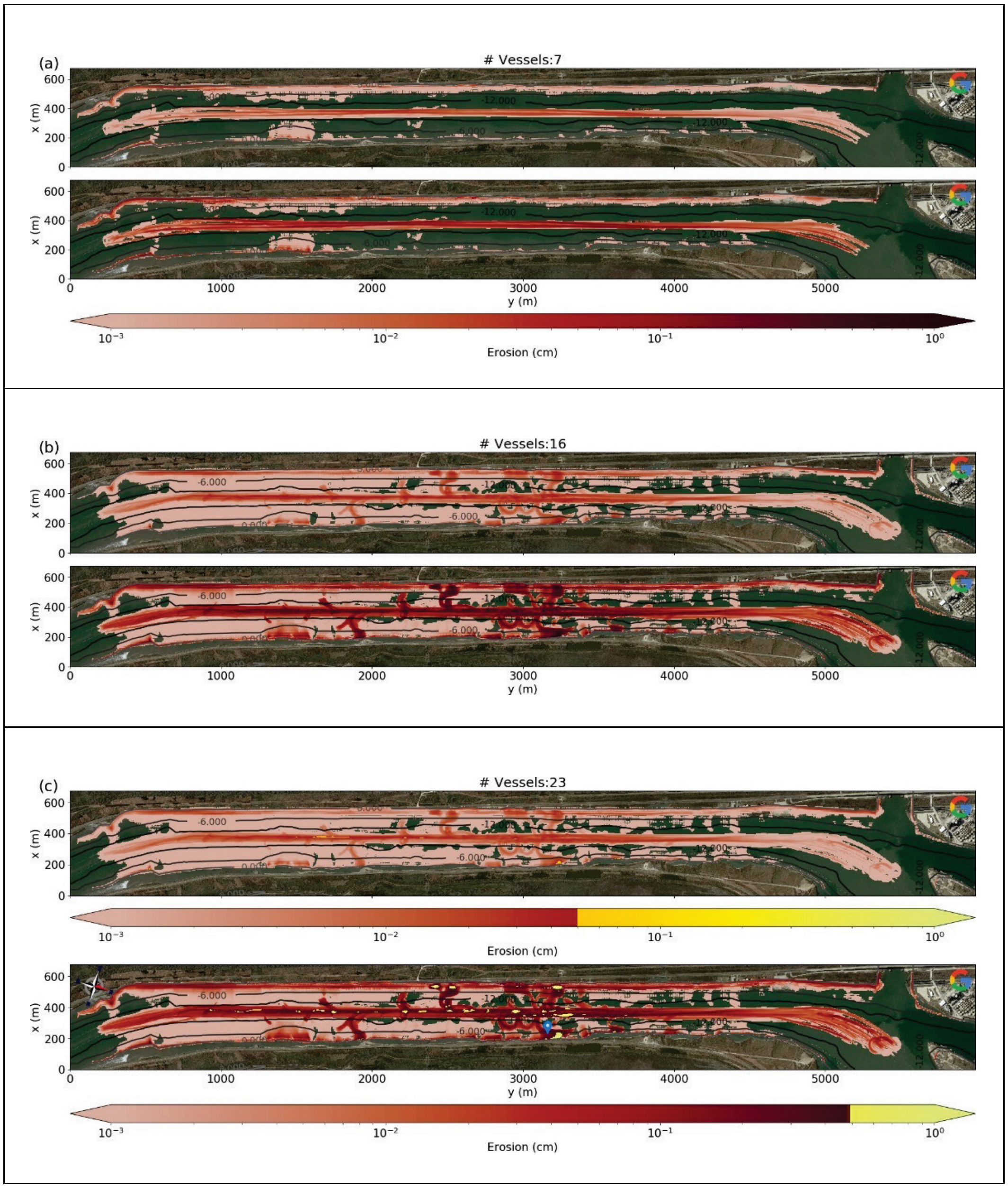

Figure 51. Satellite image of hot spot region from Gauge 2 Up grid in Figure 50, where the pin corresponds to longitude and latitude coordinates of (29.801437, -93.954770).

Figure 52. Mean and maximum erosion in Turner location for (a) inbound traffic (left to right), (b) outbound traffic (right to left), and (c) overall traffic.

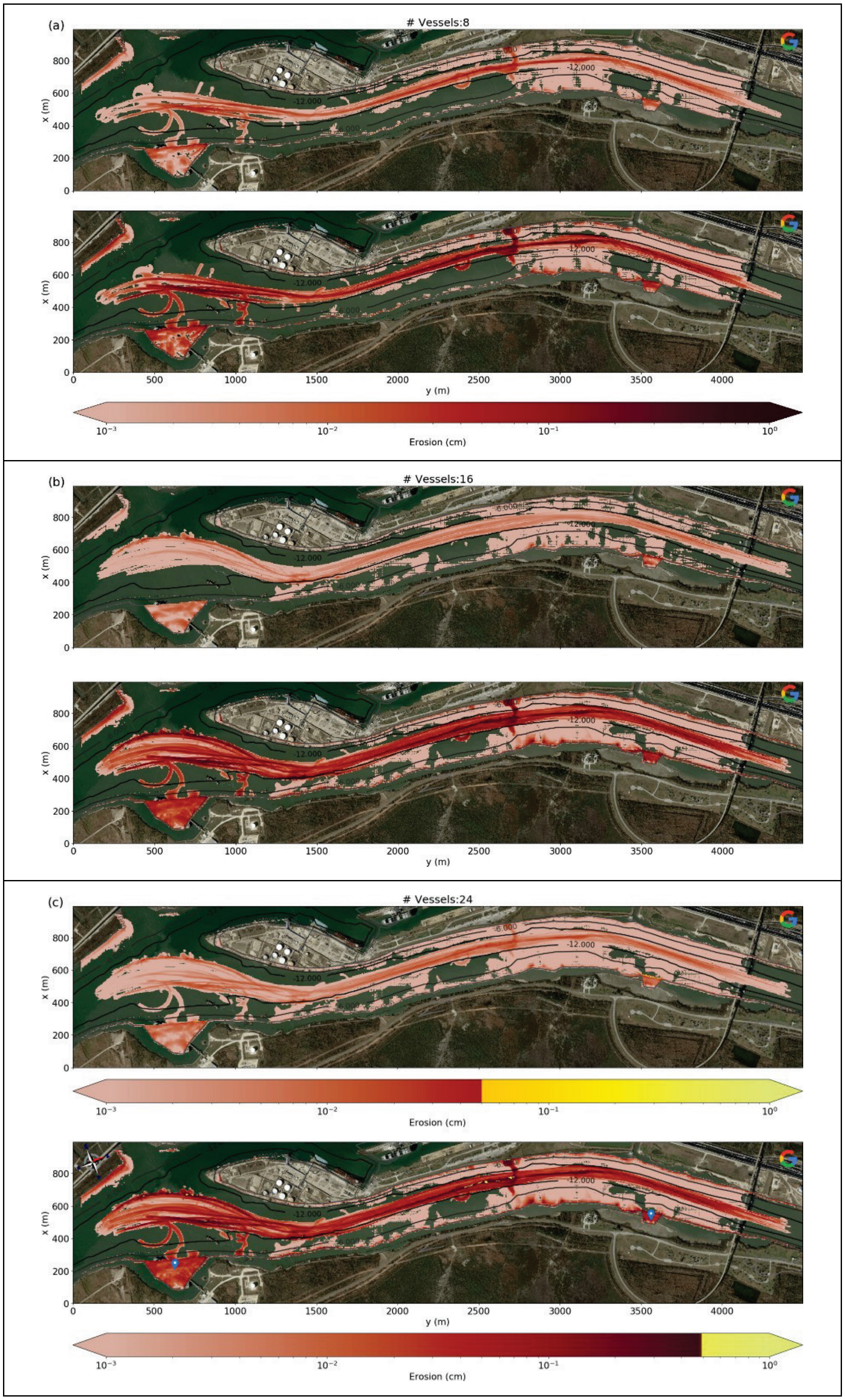

Figure 53. Satellite images of hot spot regions in Figure 52 from left to right, where the pins correspond to longitude and latitude coordinates of (29.823112, -93.954583) and (29.852255, -93.943162), respectively.

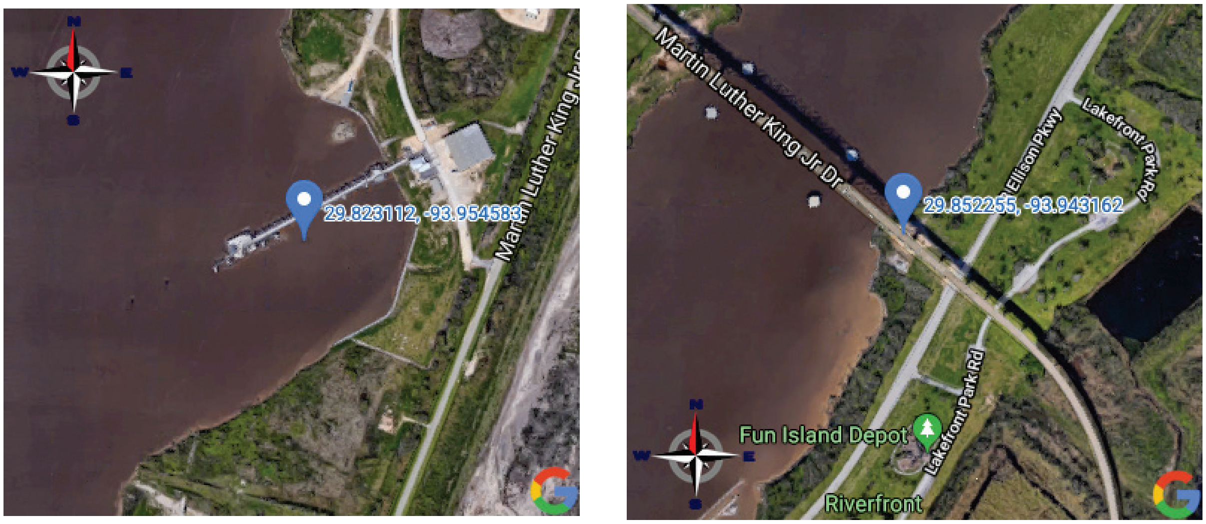

(a) (b)

Figure 54. Mean and maximum erosion in Gauge 1 location for (a) inbound traffic (left to right), (b) outbound traffic (right to left), and (c) overall traffic. Note that due to the large aspect ratio of the domain, the *y*-axis of the plots is stretched.

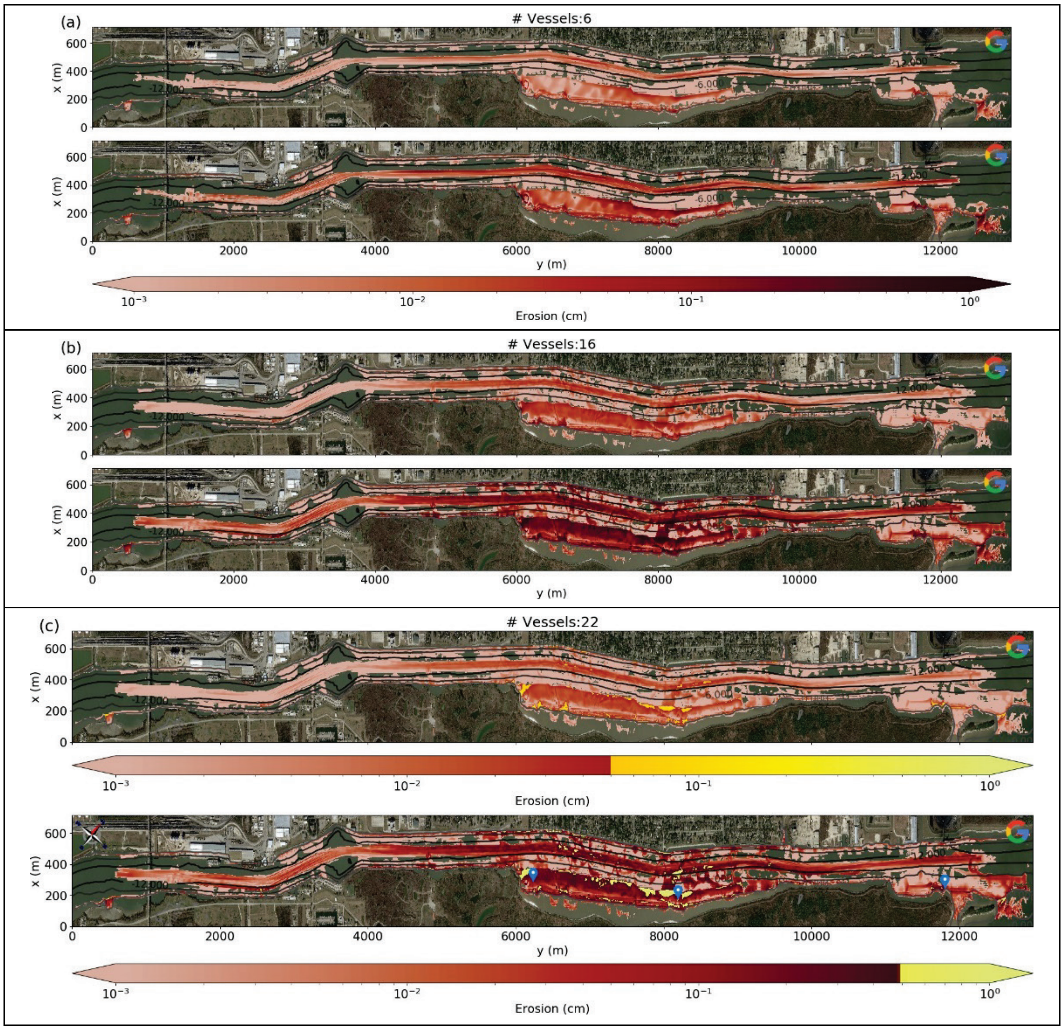

Figure 55. Satellite images of hot spot regions in Figure 54 from left to right where the pins correspond to longitude and latitude coordinates (29.888246, -93.910852), (29.902370, -93.895891), and (29.928291, -93.873383), respectively.

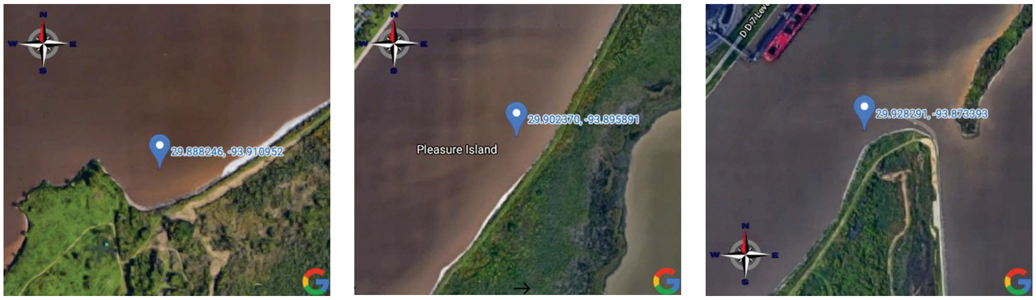

(a) (b) (c)

5 Discussion and Concluding Remarks

In summary, the results identified a variety of erosion hot spots in the SNWW region, which included the two heavy erosion regions mentioned in report of Zaloom et al. (2017). Furthermore, the additional erosion hot spots not contained in the above-mentioned report, but identified in the simulation results, appear to be inherently a result of 2D bathymetry features and 2D variable vessel paths, suggesting that higher-fidelity phase-resolving Boussinesq-type 2D numerical modeling is a key to correctly simulating the vessel wave-induced sediment transport and morphology change. These findings, however, would benefit from additional investigation so that the community can establish whether this is due just to variable tracks, or speed, or changing draft, especially when inbound and outbound tracks produce different results.

FUNWAVE-TVD has been shown to simulate vessel-generated waves that match the observed heights and periods of the drawdown wave within 20% with appropriately tuned shape parameters. In some cases, the model matches data within a few percent and captures the TSW very well. Furthermore, the corresponding ship-wake induced sediment transport with morphology change show reasonable agreement with field data. However, there were some stability issues and fluctuations of pressures below vessels that had a low UKC, thereby potentially leading to enhanced erosion below the vessel. The authors acknowledge that this requires further investigation. In addition, the following points are re-emphasized.

1. Cubic-spline interpolation was important for smoothing out vessel paths and for obtaining high-enough frequency path data for the simulations. This step removes spurious waves that raw AIS data may introduce into the simulations (e.g., sudden accelerations/deceleration resulting from erroneous numerical speeds calculated from raw data). In addition, providing more detailed location data during turns (interpolated onto finer time steps) for smoother vessel paths, removes the raw, jagged AIS path that gave rise to the paddle-type wavemaker effect.
2. Several vessel source functions were implemented in the model. Pressure Source TYPE I provided the best agreement with the field data in the model validation. The slender sources, based on either the pressure function or flux function, failed to predict correct drawdown wave heights from large-size vessels. Consequently, the pressure source TYPE I was

used in the study of vessel-generated wave erosion from large-size vessels traveling in the SNWW.

3. Within the framework of analyzing these vessel-generated episodic wave events, model sensitivity to the vessel parameters in Pressure Source TYPE I show that vessel dimensions affect wave heights and periods in a mostly linear fashion and in somewhat predictable way (e.g., increasing draft would increase the wave height). Furthermore, the model allows for small variations in vessel dimensions without drastically altering the results. Hence, this illustrates the robustness of the ship-wake model. Sensitivity to vessel-shape (curvature of the hull) parameters are slightly more complex and may require further investigation, especially when initializing the model in an operational setting with specific and firm vessel parameters from given block coefficient (C_B), or midship section area co-efficient (C_M).
4. There are numerical stability issues unresolved in the study, especially for deep-draft vessels. When a pressure source is moving, the pressure field representing a vessel shape deviates from the initial distribution and causes fluctuations. For a deep-draft vessel, the moving pressure source with fluctuations can touch the channel bed, resulting in numerical instabilities. Note that this will likely be a common problem for models that implement vessel-generated waves with a pressure-source methodology (e.g., HIVEL2D, AdH), as also experienced and discussed in Maynord (2003). In Maynord (2003), the problem was remedied by decreasing the vessel draft and enlarging the width (beam), thereby keeping the mid-ship cross-sectional area of the vessel the same. This stabilized the simulations, but it is unclear what operational effect it had on the vessel-generated wave field. In this current examination, as discussed in subsection 4.2, a similar trend was observed, albeit for only one type of a vessel. The approach shows promise, but the problem needs to be further investigated[1].
5. The model can predict the erosion hot spots caused by large-size vessels. The results showed that erosion occurs along the SNWW banks as expected. However, simulation results also suggest that some erosion hot spots are a result of inherently 2D features, such as channel bank geometry or vessel turning, where the latter may increase wave energy on the outside of the turn. In addition, existence of what is termed as coves,

---

[1] After the production of this report, new stabilization features were added to FUNWAVE-TVD to address instability issues of deep-draft vessels with low UKC. This new stabilization mechanism has been shown to suppress high-frequency noise due to this instability and allow simulation of vessels with drafts that can touch or even extend beyond the channel depth (see Malej [2021] for further details).

or vessels traveling from a wider channel to a thinner one, is causing funneling of the waves into a smaller region. This can lead to additional erosion stemming from repeated wave reflections (ringing).

References

Barrass, C. B. 2004. *Ship Design and Performance for Masters and Mates*. Elsevier Ocean Engineering Book Series. Oxford: Elsevier Butterworth-Heinemann.

Bartels, R. H., J. C. Beatty, and B. A. Barsky. 1993. "Thermite and Cubic Spline Interpo lation." In M. Kaufmann (Ed.), *An Introduction to Splines for Use in Computer Graphics and Geometric Modelling*. San Francisco, CA: Morgan Kaufmann.

Bayrakter, D. and S. Beji. 2013. "Numerical Simulation of Waves Generated by a Moving Pressure Field. *Ocean Engineering* 59(2013): 231–239. doi:10.1016/j.oceaneng.2012.12.025.

Cao, Z. 1999. "Equilibrium Near-Bed Concentration of Suspended Sediment." *J. of Hydraulic Eng*. 125(12): 1270–1278.

Chen, Q. 2006. "Fully Nonlinear Boussinesq-Type Equations for Waves and Currents over Porous Beds." *J. of Engineering Mech.* 132(2): 220–230.

Chen, Q., J. T. Kirby, R. A. Dalrymple, A. B. Kennedy, and A. Chawla. 2000. "Boussinesq Modeling of Wave Transformation, Breaking, and Runup." *J. of Waterway, Port, Coastal, and Ocean Eng*. 126(1): 48–56. doi:10.1061/(ASCE)0733-950X(2000)126:1(48).

David, C. G., V. Roeber, N. Goseberg, and T. Schlurmann. 2017. "Generation and Propagation of Ship-Borne Waves - Solutions from a Boussinesq-type Model." *Coastal Engineering* 127(2017): 170–187.

Elder, J. 1959. "The Dispersion of Marked Fluid in Turbulent Shear Flow." *J. of Fluid Mech.* 5(4): 544–560. doi:10.1017/S0022112059000374.

Erduran, K. S., S. Ilic, and V. Kutija. 2005. "Hybrid Finite-Volume Finite-Difference Scheme for the Solution of Boussinesq Equations." *International Journal for Numerical Methods in Fluids* 49(11): 1213–1232.

Ertekin, R. C., W. C. Webster, and J. V. Wehausen. 1986. "Waves Caused by a Moving Disturbance in a Shallow Channel of Finite Width." *Journal of Fluid Mechanics* 169(1986): 275–292.

Gottlieb, S., C.-W. Shu, and E. Tadmor. 2001. "Strong Stability-Preserving High-Order Time Discretization Methods." *SIAM Review* 43(1): 89–112.

Kennedy, A. B., Q. Chen, J. T. Kirby, and R. A. Dalrymple. 2000. "Boussinesq Modeling of Wave Transformation, Breaking, and Runup." *J. of Waterway, Port, Coastal, and Ocean Eng*. 126(1): 39–47.

Kennedy, A. B., J. T. Kirby, Q. Chen, and R. A. Dalrymple. 2001. "Boussinesq-type Equations with Improved Nonlinear Performance." *Wave Motion* 33(3): 225–243.

Lam, M. Y., M. Malej, F. Shi, and K. Ghosh. 2018. *Profiling and Optimization of FUNWAVE-TVD on High Performance Computing (HPC) Machines*. ERDC/CHL CHETN-I-95. Vicksburg, MS: US Army Engineer Research and Development Center.

Malej, M., F. Shi, and J. M. Smith. 2019. *Modeling Ship-Wake-Induced Sediment Transport and Morphological Change — Sediment Module in FUNWAVE-TVD*. ERDC/CHL CHETN-VII-20. Vicksburg, MS: US Army Engineer Research and Development Center. doi: http://dx.doi.org/10.21079/11681/32911.

Malej, M., and F. Shi. 2021. *Suppressing the Pressure-Source Instability in Modeling Deep-Draft Vessels with Low Under-Keel Clearance in FUNWAVE-TVD*. ERDC/CHL CHETN-IX-55. Vicksburg, MS: US Army Engineer Research and Development Center. doi: http://dx.doi.org/10.21079/11681/40639.

Maynord, S. T. 2003. *Ship Effects before and after Deepening of Sabine-Neches Waterway, Port Arthur, Texas*. ERDC/CHL TR-03-15. Vicksburg, MS: US Army Engineer Research and Development Center.

Meyer-Peter, E., and R. Müller. 1948. "Formulas for Bed-Load Transport." In IAHSR 2nd Meeting, Stockholm, Appendix 2. IAHR, 1948.

Nwogu, O. 2001. *Bouss2D: A Boussinesq Wave Model for Coastal Regions and Harbors*. ERDC/CHL TR-01-25. Vicksburg, MS: US Army Engineer Research and Development Center.

Safty, H. E., and R. Marsooli. 2020. "Ship Wakes and Their Potential Impacts on Salt Marshes in Jamaica Bay, New York." *J. Mar. Sci. Eng* 8(5): 325.

Shi, F., J. T. Kirby, J. C. Harris, J. D. Geiman, and S. T. Grillis. 2012. "A High-Order Adaptive Time-Stepping TVD Solver for Boussinesq Modeling of Breaking Waves and Coastal Inundation." *Ocean Modelling* 43(2012): 36-51.

Shi, F., M. Malej, J. M. Smith, and J. T. Kirby. 2018. "Breaking of Ship Bores in a Boussinesq-type Ship-Wake Model." *Coastal Engineering* 132(2018): 1–12.

Stockstill, R. L., and R. C. Berger. 1994. *HIVEL2D: A Two-Dimensional Flow Model for High-Velocity Channels*. Technical Report REMR-HY-12. Vicksburg, MS: US Army Engineer Waterways Experiment Station.

Stockstill, R. L., and R. C. Berger. 1999. *A Two-Dimensional Flow Model for Vessel-Generated Currents*. ENV Report 10. US Army Engineer District, Rock Island; US Army Engineer District, St. Louis; US Army Engineer District, St. Paul.

Tehranirad, B., J. T. Kirby, F. Shi, and S. T. Grilli. 2016. *Does Morphological Adjustment During Tsunami Inundation Increase Levels of Hazard?* Research Report No. CACR-16-02. Center of Applied Coastal Research, Department of Civil and Environmental Engineering, University of Delaware.

Torsvik, T., G. Pederson, and K. Dysthe. 2009. “Waves Generated by a Pressure Disturbance Moving in a Channel with Variable Cross-Sectional Topography.” *J. of Waterway, Port, Coastal, and Ocean Eng*. 135(3): 120–123.. doi:10.1061/(ASCE)0733- 950X(2009)135:3(120).

USACE (US Army Corps of Engineers). 2017. *Sabine Pass to Galveston Bay, Texas Coastal Storm Risk Management and Ecosystem Restoration: Final Integrated Feasibility Report – Environmental Impact Statement*. Technical report. Galveston District – Southwestern Division, Galveston, Texas.

USACE. 2018. *Investigations - Fact Sheets*. Technical report. Galveston District – Southwestern Division, Galveston, Texas.

USACE. 2020. *AIS Analysis Package* (AISAP). Software package. https://aisap.usacegis.us/aisap portal/home.html.

van Rijn, L. 1984. “Sediment Pick-up Functions.” *J. of Hydraulic Eng*. 110(10): 1494–1502. doi:10.1061/(ASCE)0733-9429(1984)110:10(1494).

Woodruff, I., J. T. Kirby, F. Shi, and S. Grilli. 2018. “Estimating Meteo-Tsunami Occurrences for the US East Coast.” *Coastal Engineering Proceedings 36* (2018): 66–66.

Wu, T. Y. 1987. “Generation of Upstream Advancing Solitons by Moving Disturbances.” *Journal of Fluid Mechanics* 184(1987): 75–99.

Zaloom, V., Q. Qian, M. Jao, X. Wu, K.-H. Wang, S. Lin, and B. Kolkmeier. 2017. *Wake Wash in Sabine-Neches Waterway Phase I Report*. Technical report for Sabine-Neches Navigation District. Lamar University and University of Houston.

Appendix A: Sample FUNWAVE Input File

An example input file is shown in this appendix. The input file is divided into two parts: variables that vary between simulations and variables that are constant for all simulations.

A.1 Input variables that vary between different AOIs and vessel transits

```
   ! ---------------------------------------- TITLE --------------------------------------------------------------
TITLE = Sample Input File

   ! -------------------------------------- PARALLEL INFO ----------------------------------------------
PX = 6
PY = 44

   ! ---------------------------------------- DEPTH --------------------------------------------------------------
DEPTH_FILE = 01_snww_tx_gauge2up_bathy_1m_676X5996.txt
WaterLevel = 0.886

   ! ------------------------------------ DIMENSION --------------------------------------------------------
   ! global grid dimension
Mglob = 676
Nglob = 5996

   ! ---------------------------------- OUTPUT ---------------------------------------------------------------
NumberStations = 8
STATIONS_FILE = gauge2up_gauges.txt

   ! ----------------- TIME-----------------------------------
TOTAL_TIME = 921.0
```

A.2 Input variables that were constant for all simulations

```
  ! ------------------------------- DEPTH ---------------------------------------------------
DEPTH_TYPE = DATA

  ! --------------------------- GRID ---------------------------------------------------------

DX = 1.0
DY = 1.0

  ! --------------------------- TIME -------------------------------------------------------
PLOT_INTV = 20.0
PLOT_INTV_STATION = 0.1

  ! --------------------------- OUTPUT -----------------------------------------------------
FIELD_IO_TYPE=BINARY
RESULT_FOLDER = output/

  ! -------------------------- SHIP WAKES --------------------------------------------------
VESSEL_FOLDER = ./
NumVessel = 1

  ! -------------------------- SPONGE LAYER ---------------------------------------------
DIFFUSION_SPONGE = F
FRICTION_SPONGE = T
DIRECT_SPONGE = T
Csp = 0.10
CDsponge = 10.0
Sponge_west_width =  50.0
Sponge_east_width =  50.0
Sponge_south_width = 50.0
Sponge_north_width = 50.0
R_sponge = 0.85
A_sponge = 5.0
ETA_LIMITER = F
CrestLimit = 8.0
TroughLimit = -8.0


  ! ----------------PHYSICS------------------------------
DISPERSION = T
Gamma1 = 1.0
Gamma2 = 1.0
Gamma3 = 1.0
Beta_ref=-0.531
SWE_ETA_DEP = 0.7
VISCOSITY_BREAKING = T
```

```
  ! ---------------------------- NUMERICS ----------------------------------------------------------
Time_Scheme = Runge_Kutta

HIGH_ORDER = FOURTH
CONSTRUCTION = HLLC
CFL = 0.2
FroudeCap = 1.0

  ! -------------- WET-DRY-------------------------------
MinDepth=0.02
MinDepthFrc = 0.02

  ! ---------------------------- SHOW BREAKING ---------------------------------------------
SHOW_BREAKING = F
Cbrk1 = 0.70
Cbrk2 = 0.40
WAVEMAKER_VIS = F
visbrk = 0.40

  ! ---------------------------- SEDIMENT PROPERTIES ----------------------------------
ROLLER = T
ROLLER_EFFECT = F
Bed_Change = T
BedLoad = T
D50 = 0.0005
Sdensity = 2.68
n_porosity = 0.47
WS = 0.0125
Shields_cr = 0.055
Shields_cr_bedload = 0.047
Tan_phi = 0.7
Kappa1 = 0.3333
Kappa2 = 1.0
MinDepthPickup = 0.2
```

Appendix B: Enlarged Erosion Plots

This appendix shows again the maximum erosion (per one vessel passage) for both inbound and outbound paths for the five subregions, but plotted vertically to provide more details to the reader, along with blue pins signifying an erosion hotspot.

B.1 Subgrid: Grid 1 (Mouth) – maximum erosion with hotspots

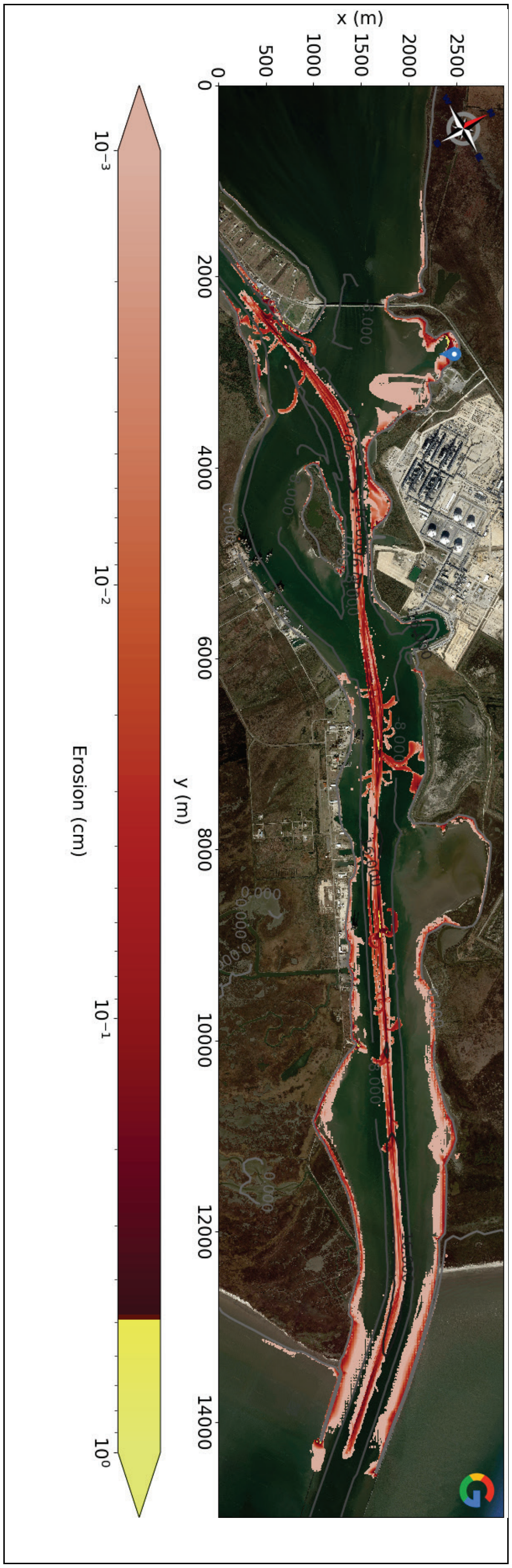

B.2 Subgrid: Gauge 2 – maximum erosion with hotspots

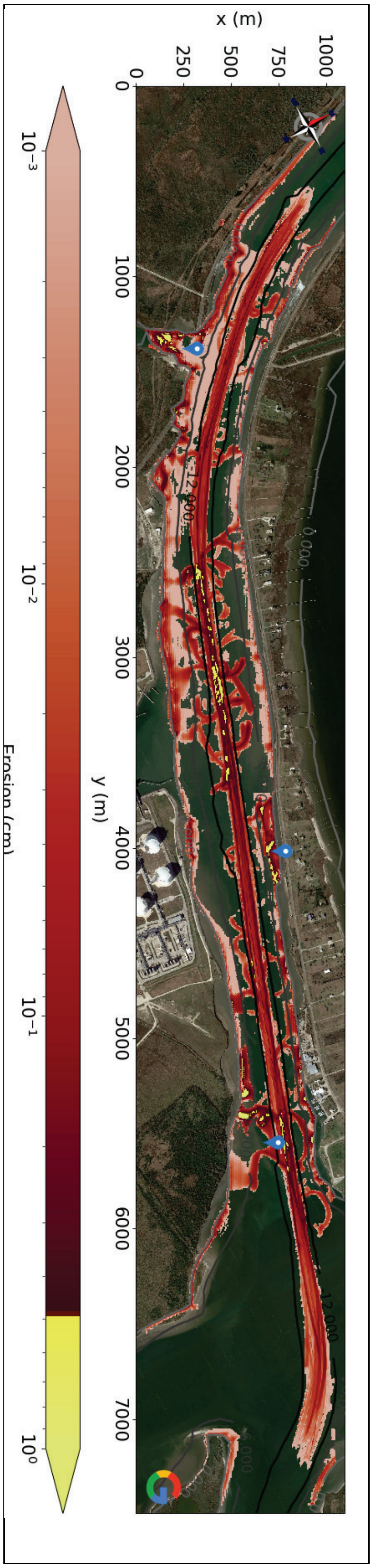

B.3 Subgrid: Gauge 2 UP – maximum erosion with hotspots

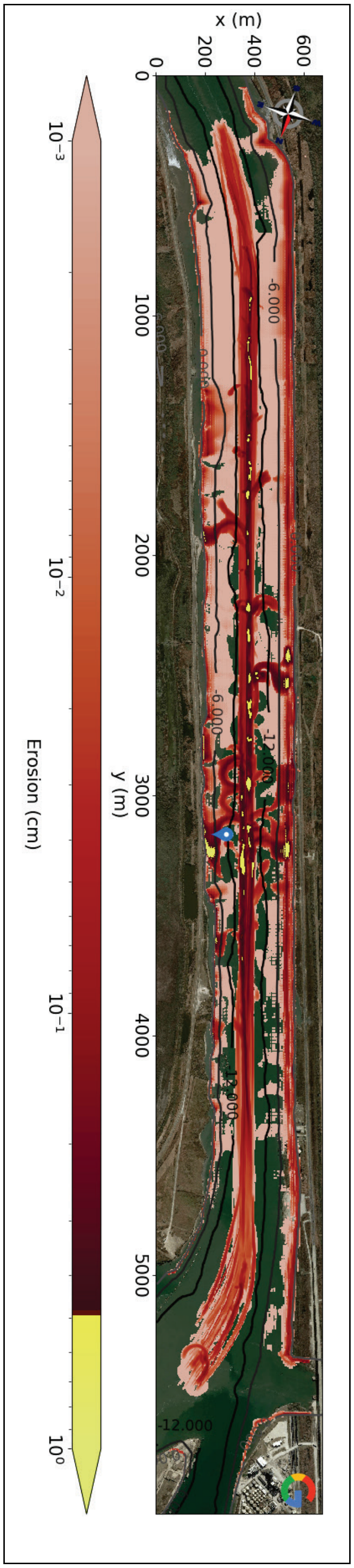

B.4 Subgrid: Turner – maximum erosion with hotspots

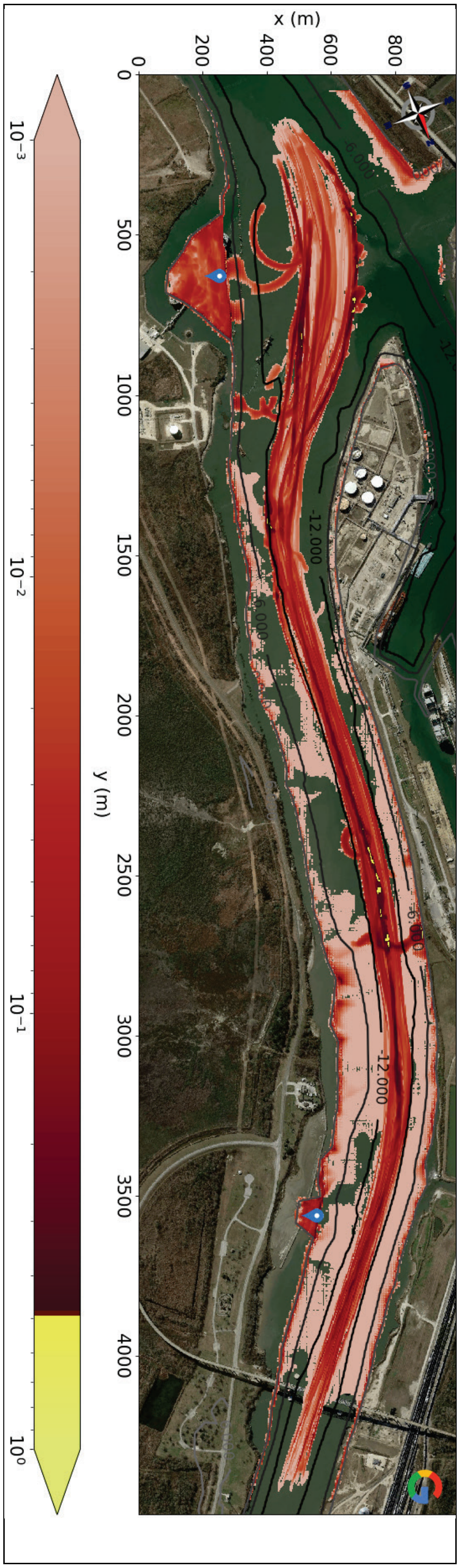

B.5 Subgrid: Gauge 1 – maximum erosion with hotspots

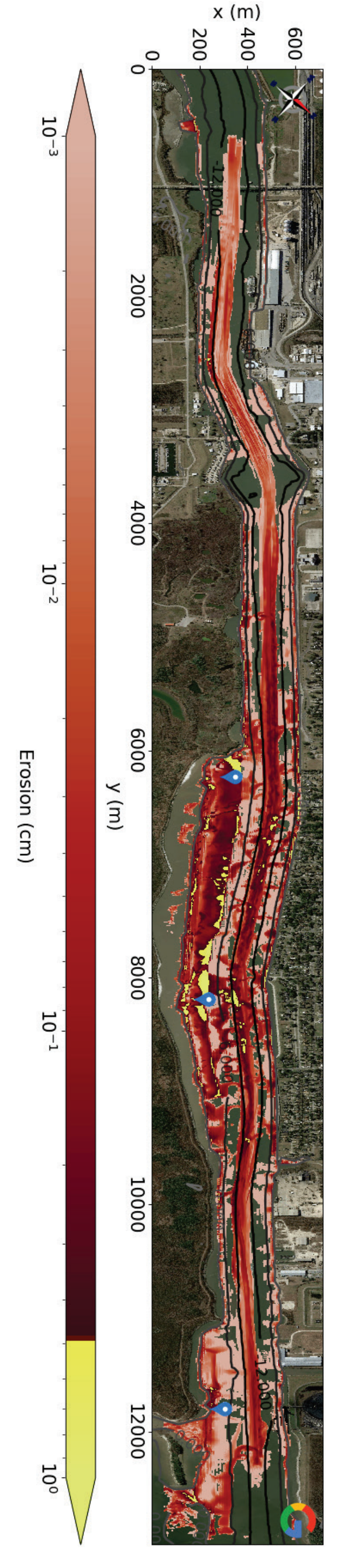

Acronyms and Abbreviations

2D	Two-dimensional
AIS	Automatic Identification System
AISP	AIS Analysis Package
AOI	Area of Interest
CFD	Computational fluid dynamics
DoD	Department of Defense
ERDC	US Army Engineer Research and Development Center
GPS	Global Positioning System
HPC	High-performance computing
MLT	Mean Low Tide
S2G	Sabine Pass to Galveston Bay
SNWW	Sabine-Neches Waterway
SWG	Galveston District
TSW	Transverse stern wave
UKC	Under-keel clearance
USACE	US Army Corps of Engineers
USCG	US Coast Guard
UTM	Universal Transverse Mercator

REPORT DOCUMENTATION PAGE

Form Approved
OMB No. 0704-0188

1. REPORT DATE September 2022	**2. REPORT TYPE** Final Report	**3. DATES COVERED** *(From - To)* FY20–FY21

4. TITLE AND SUBTITLE
Operational Modeling of Large Container-Type Vessel-Generated Waves with Related Erosion and Scour Effects

5a. CONTRACT NUMBER

5b. GRANT NUMBER

5c. PROGRAM ELEMENT NUMBER

6. AUTHOR(S)
Michael-Angelo Y.-H. Lam, Matt Malej, and Fengyan Shi

5d. PROJECT NUMBER

5e. TASK NUMBER

5f. WORK UNIT NUMBER

7. PERFORMING ORGANIZATION NAME(S) AND ADDRESS(ES)

Coastal and Hydraulics Laboratory
US Army Engineer Research and Development Center
3909 Halls Ferry Road
Vicksburg, MS 39180-6199

Center for Applied Coastal Research
University of Delaware
259 Academy Street
Newark, DE 19716

8. PERFORMING ORGANIZATION REPORT NUMBER
ERDC/CHL TR-22-20

9. SPONSORING/MONITORING AGENCY NAME(S) AND ADDRESS(ES)
Navigation Research Program
US Army Engineer Research and Development Center
3909 Halls Ferry Road
Vicksburg, MS 39180-6199

10. SPONSOR/MONITOR'S ACRONYM(S)
NAVSYS

11. SPONSOR/MONITOR'S REPORT NUMBER(S)

12. DISTRIBUTION/AVAILABILITY STATEMENT
Approved for public release; distribution is unlimited.

13. SUPPLEMENTARY NOTES
Funding Account Code U4381107; AMSCO Code 031391

14. ABSTRACT
In this report, the US Army Engineer Research and Development Center, Coastal and Hydraulics Laboratory, presents a numerical modeling study using FUNWAVE-TVD to investigate ship-induced waves of large container-type vessels with related erosion and scour effects. The new vessel wake generating models implemented in the FUNWAVE-TVD Vessel Module are presented and validated against field data in the Sabine-Neches Waterway, Texas. Utilizing the Sediment Transport and Morphology Change Modules, ship wake-induced erosion is analyzed to assess potential impacts to Sabine-to-Galveston Hurricane Flood Protection Systems.

15. SUBJECT TERMS
Container ships, Erosion, Scour (Hydraulic engineering), Sedimentation and deposition, Sediment transport, Wakes (Fluid dynamics)

16. SECURITY CLASSIFICATION OF:			**17. LIMITATION OF ABSTRACT**	**18. NUMBER OF PAGES**	**19a. NAME OF RESPONSIBLE PERSON**
a. REPORT	**b. ABSTRACT**	**c. THIS PAGE**			Matt Malej
Unclassified	Unclassified	Unclassified	SAR	96	**19b. TELEPHONE NUMBER** *(Include area code)* 603-646-4455